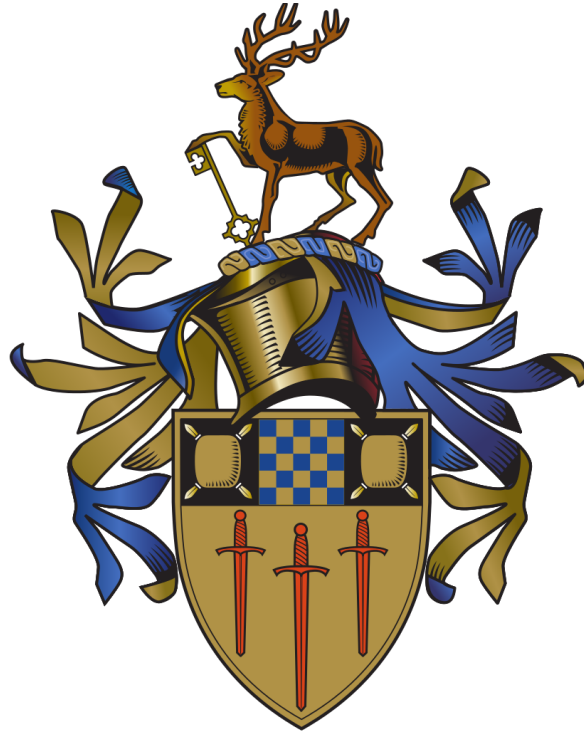


Study of the transport of water in the nanopores of C–S–H by ^1H NMR



Vadzim Yermakou

Department of Mechanical Engineering and Sciences
University of Surrey

This dissertation is submitted for the degree of
Engineering Doctorate

2017

Acknowledgements

The completion of this thesis would not be possible without help and support of several people to whom I am extremely grateful.

Firstly, I would like to express my sincere gratitude to my supervisor Professor Peter McDonald for the continuous support of my EngD study and research, for his patience, motivation and enthusiasm. His immense knowledge, his ability to test a complex hypothesis with the back of the envelope calculations, his advice whilst allowing me the room to work in my own way encouraged me to conduct research. I attribute the level of my English to his encouragement and effort to raise it above the level of native speakers.

Secondly, I'd like to thank Jeffrey Chen, Ellis Gartner and Remi Barbarulo from Lafarge-Holcim for the cement chemistry discussions and assistance with corporate affairs. Also LafargeHolcim R&D laboratories for letting me work on NMR and the technical team for taking care of NMR spectrometer.

In my daily work I have been blessed with a friendly NMR group of TRANSCEND: Arnaud, Agata and Noemy. It's a pleasure to thank them for the fruitful stimulating discussions of NMR and cement, for their support and for all the fun we have had in the last four years. It was great to see you at my defence.

Agata Gajewicz contributed to this thesis by drawing C-S-H model sketch used in Section 6, she is also responsible for the design of the figures in Chapter 6. The data discussed in Section 6.3.4 were obtained by Agata Gajewicz and Koljeet Kang at the University of Surrey. Agata also has an amazing quality of a welcoming hostess and I owe my deepest gratitude to her for the opportunity to share the flat with her family during my visits to the University of Surrey.

I am indebted to Centre for Doctoral Training and Noelle for support and invaluable help in hard situations associated with my health problems.

Finally, I thank my parents for supporting me spiritually throughout all my studies at University; they have made available their support in a number of ways. I would like to show you my gratitude for caring and believing in me.

Last, but certainly not the least, warmest thanks to my wife Yulya and son Martin for letting me work in the evenings both in the lab and at home.

I would like to acknowledge the sponsorship from European Commission for Marie-Curie Initial Training Network Transcend ‘The Understanding TRANSport for Concrete which is Eco friendly, iNnovative and Durable’ (EP7/2007-2013).

Abstract

This thesis describes a series of ^1H nuclear magnetic resonance (NMR) experiments to investigate connectivity of the the nanopores of the calcium-silicate-hydrates (C–S–H) in cement based materials. This is achieved by coupling ^1H NMR relaxometry in one and two relaxation times dimensions and ^1H NMR cryoporometry down to about -80°C . In particular the thesis contains the first use in any system of coupled two dimensional relaxometry and low temperature cryoporometry.

The cryoporometry has been validated on model porous silica glass (SiO_2) materials with known pore sizes and then applied to C_2S and C_3S , in cement chemistry notation, otherwise known as alite and belite. The ^1H NMR cryoporometry data was used to estimate the pore sizes in C_2S . It was found that the T_2 relaxation time depends on temperature in C_2S and C_3S , but not in porous glasses SiO_2 and MCM-41. There are two possible explanations. It could be due to the interaction of water with the -OH groups on the pore surface. It is known, that water, or a monolayer of water becomes physisorbed on silanol groups. Silanol groups are present both at the silica glasses surfaces as well at the cement pores surfaces. However, there are no many studies available on the interaction of water-silanol groups and temperature dependency below 0°C . The other explanation concerns hydrated calcium ions in cementitious materials not present in silica glasses. However, little is known about C–S–H surfaces.

A two dimensional ^1H NMR $T_2 - T_2$ exchange experiment was used to investigate the exchange of water between interlayer spaces, gel pores and capillary pores at temperatures of room temperature, -5°C and -30°C on cooling and again on warming in C_3S . A 3-site exchange numerical model was written to solve the associated coupled differential magnetisation exchange equations. By comparing the model output and experimental data it was shown that water exchanges between interlayer spaces and gel pores and between interlayer spaces and capillary pores. However, there is no exchange from gel pores to capillary pores.

A further set of room temperature experiments were carried out to investigate the change in the pore size distribution of C-S-H in white cement following desorption and resorption of water as a function of drying severity. Rearrangements of the nano porosity were seen

dependant on the severity of the drying. There were both reversible and irreversible changes. However, the total pore volume remained constant within measurement error. Most interestingly for more severe drying relaxation of the pore size distribution was seen for several days following resorption of water.

All the experimental work was carried out at the LafargeHolcim research laboratories in Lyon, France. The thesis also contains details of the adaptation necessary to carry out experiments described on a standard Maran Ultra 23.5 MHz NMR spectrometer.

Table of contents

1	Introduction	1
2	Theory	5
2.1	Basic principles of NMR relaxometry	5
2.1.1	Theory of NMR relaxometry	5
2.1.2	Data Analysis	16
3	Literature review	19
3.1	Introduction	19
3.2	C-S-H	19
3.2.1	What is unhydrated cement?	19
3.2.2	Cement hydration	20
3.2.3	Rate growth	21
3.2.4	Powers and Brownyard model	21
3.2.5	C-S-H models	22
3.2.6	Jennings	23
3.2.7	Cement porosity	25
3.3	Methods to measure cement porosity	25
3.3.1	MIP	25
3.3.2	BET	25
3.3.3	LTC	26
3.3.4	Disadvantages	26
3.4	Meso-structural models of cement	27
3.4.1	Structure	27
3.5	NMR	27
3.5.1	Relaxometry	27
3.5.2	T_2 - T_2 exchange experiments	30
3.5.3	NMR Cryoporometry	31

3.5.4	Combined relaxometry and cryoporometry	31
4	Technique development	33
4.1	Coil height	33
4.1.1	3 days old cement paste with water to cement ratio 0.4 with 2 thermocouples.	34
4.2	Thermal equilibrium	36
4.3	Curie's correction	36
4.4	$T_2 - T_2$ validation	37
4.5	Conclusions	40
5	Cryoporometry and relaxometry on model materials	41
5.1	Results	41
5.1.1	Materials and methods	41
5.1.2	Results: 8.7 nm porous glass	44
5.1.3	Results: 11 nm porous glass	48
5.1.4	Results: 3 nm MCM41	51
5.1.5	Discussion	56
5.2	Relaxometry-cryoporometry on the cementitious materials	59
5.2.1	Materials and methods	60
5.2.2	Results for C_2S	61
5.2.3	Results for C_3S	66
5.3	Conclusions	71
6	Study of C-S-H drying shrinkage and relaxation on rewetting.	73
6.1	Background	73
6.2	Methods and materials	73
6.2.1	Mixing and curing	73
6.2.2	Measurement cycle	74
6.2.3	CPMG and Quad-echo details	74
6.2.4	Data analysis	75
6.3	Results	77
6.3.1	Sample dried at 60°C	77
6.3.2	Severity of drying	79
6.3.3	Varying w/c ratio	81
6.3.4	Second sorption cycle	85
6.3.5	Study of robustness of data fitting	85

6.4	Discussion	87
6.5	Conclusions	90
7	$T_2 - T_2$ on the C_3S	91
7.1	Introduction	91
7.2	Prior work	92
7.3	NMR theory	93
7.3.1	Three-Site exchange model	95
7.3.2	Code validation: 1D exchange rate	96
7.3.3	Code validation: 2D exchange rate	97
7.4	Materials and methods	101
7.4.1	Materials	101
7.4.2	NMR experiments	101
7.5	Experiment development	102
7.6	Results: $T_2 - T_2$	103
7.7	Results: model	106
7.8	Conclusions	111
8	Conclusions	113
8.1	Future work	114
	References	115
	Appendix A Matlab 3 site exchange $T_2 - T_2$ model	121
	Appendix B $T_2 - T_2$ pulse sequence	125

Chapter 1

Introduction

Cement is the binding phase of concrete, the most abundantly produced man-made material amounting up to one cubic metre per person per year in the world (Gartner, 2004). It is cheap, easy to operate material. Although cement is an inherently low CO₂ material compared to all other widely used construction materials, the volumes used nonetheless mean that it accounts for circa 5% of global CO₂ emissions Gartner (2004). About half of these emissions come from the breakdown of limestone $\text{CaCO}_3 \rightarrow \text{CaO} + \text{CO}_2$ to make CaO used in the production of Portland cement - the most common cement - and CO₂. The other half of emissions is from the heat required for the production process. The production process is already highly optimized therefore reduction of CO₂ requires the use of alternate, or supplementary cementitious materials to lower the limestone requirement and/or improvements to cement durability to lower the amounts used.

The principal component and binding phase of Portland cement and thus concrete is calcium silicate hydrate (C–S–H). C–S–H is a highly disordered, semi-crystalline nanoscale porous material comprising sheets of Ca ions and silica tetrahedra interspersed by layers of water. Further nanoscale pores known as gel pores separate locally aggregated layers. In order to replace limestone in cements or to improve durability, it is necessary to have a good knowledge of the hydration process, meso-structure and durability of C–S–H and other related hydrates arising from different cementitious materials. Mesostructure is important because porosity determines water transport properties and water ingress and egress is ultimately linked to all forms of cement degradation. Surprisingly, the mesostructure of C–S–H from even Portland cement is poorly understood. At the outset of this work, there are several competing models to describe the morphology of C–S–H. They tend to centre on either colloidal models such as that proposed and widely adopted by Jennings (2008) or on continuum sheet models as proposed by Feldman and Sereda (1970).

This thesis describes work to better understand the porosity of cement hydrates and in particular C–S–H.

^1H nuclear magnetic resonance (NMR) relaxometry is a non-invasive and non-destructive method of characterizing porous material. It is widely used by the oil and gas, chemicals, medical and food industries (Mitchell et al., 2014). It directly probes the pore fluid. Although it has been applied to cements for over 40 years (Blinic et al., 1978), only recently has it been shown to be quantitative for cements with a proper interpretation of the different signals (Peemoeller et al., 1981), (Greener et al., 2000), (Muller et al., 2013, 2012). In recent years, multi-dimensional methods have been developed that can show the exchange of pore fluid between pores (Monteilhet et al., 2006).

Using ^1H NMR relaxometry the drying shrinkage of gel pores of C–S–H has been studied. Use of an innovative combination of two dimensional ^1H NMR relaxometry $T_2 - T_2$ exchange experiments and temperature variation has allowed new insights into the pore connectivity of the C–S–H.

Cryoporometry is an alternate means to characterize porous media dependent on the melting point depression of fluids in small pores (Petrov and Furó, 2009). It has been used in the form of NMR cryoporometry as a means to measure unfrozen pore liquid since the mid 1990's (Strange, 1994). It has been applied to concrete (Valckenborg et al., 2002). In this work cryoporometry is used paired with relaxometry to allow the study of the water signal evolution on thawing in model cement materials C_2S and C_3S .

Results presented here are obtained during work carried out under an EngD research collaboration between the University of Surrey (UK) and LafargeHolcim Research Centre (France). It is part of a larger EC funded Marie Curie Initial Training Network known as TRANSCEND, that comprise 15 doctoral projects across an Europe wide academia-industrial network. TRANSCEND research focuses more widely on the transport properties of water at different length and time scales from cement paste to concrete.

The specific objectives of this project and thesis are:

- To introduce advanced NMR techniques, including cryoporometry, relaxometry and multi-dimensional relaxometry to the LafargeHolcim industrial R&D laboratory.
- To study cement drying shrinkage and rewetting by means of relaxometry.
- To develop the methodology for multi-dimensional combined NMR relaxometry and NMR cryoporometry for low temperature characterization of model porous materials and cement.

- To characterize the connectivity of the C–S–H inter-layer space and the gel porosity in cement pastes and to better quantify exchange between the two using the combined methodology.
- To find evidence that may help to distinguish between two competing models of C–S–H morphology: colloidal models or continuum sheet models.

Chapter 2 describes the essential theory and methodology to understand ^1H NMR as used in this thesis.

Chapter 3 reviews the essential elements of cement materials science as understood at the outset of the thesis. It includes a summary of results obtained using a variety of techniques including ^1H NMR.

Chapter 4 describes the essential work that was undertaken to introduce the new ^1H NMR technique onto the instrumentation available at the LafargeHolcim laboratories.

Chapter 5 describes the new ^1H NMR cryoporometry results.

Chapter 6 describes the new experiments to measure C–S–H shrinkage using ^1H NMR

Chapter 7 describes the results of experiments to combine ^1H NMR $T_2 - T_2$ exchange experiments and cryoporometry.

The thesis ends with a short conclusion and appendices with computer codes developed as part of the work.

Chapter 2

Theory

2.1 Basic principles of NMR relaxometry

2.1.1 Theory of NMR relaxometry

Overview; Spectroscopy; Relaxometry

The history of NMR begins in early 1920s, when a number of groups studied electron spin. The most notable work for NMR is the Stern-Gerlach experiment. In 1938 Isidor Isaac Rabi (Breit and Rabi, 1931) developed a technique, by extending Stern-Gerlach experiment, for measuring the nuclear spin. In 1944 Rabi received a Nobel prize for this work. Two different groups led by Felix Bloch and Edward Mills Purcell respectively tried experiments to measure the nucleus spin gyromagnetic ratio of proton using a Larmor precession resonance experiment on water and solids. Both worked well and in 1952 they shared a second Nobel Prize. For the next decade, NMR was predominantly used by chemists. This was the start of NMR spectroscopy of liquids. They started to measure chemical shifts and spin-spin coupling to gain information on molecule structure. Hahn (1950) showed that sequences of pulses not only made experiments fast but also provided new information on dynamics. However, due to the difficulties of recording free induction decay signal, that followed the pulses, the field did not progress a lot until the late 1950s. It was noticed that Fourier Transformation of the signal following the pulse gave the spectrum. With the appearance of the first minicomputers, Fourier Transform (FT) NMR made data processing much quicker.

It was found in 1960 that spectrum of solids is much better resolved when the sample is rotated about the axis inclined by $54^{\circ}44'$ to the direction of the magnetic field. This discovery led to the high resolution spectroscopy of solids.

Another development of the NMR technique was made by Lauterbur (1973). It was shown that by repeating measurements with magnetic field gradients applied in different directions and Fourier Transform the signals it is possible to reconstruct a 2D image of a sample. This discovery led to the 2D imaging technique which later evolved into the magnetic resonance imaging (MRI).

A much more complete historical review could be found in books by Callaghan (2011) and Kimmich (2012).

Resonance and Larmor Equation

The principle of the NMR method is that atomic nuclei with odd numbers of protons and neutrons possess a magnetic moment or “spin”. The hydrogen proton ^1H is one of such nucleus. This thesis work has been performed on the materials that contain hydrogen as a key constituent of water: H_2O .

When water molecules are placed in a magnetic field, the hydrogen spins align with the field to create a bulk nuclear magnetisation. If the spins are disturbed from this alignment with the field, they precess at a frequency f_0 which is proportional to the strength of the field B_0 . It is the Larmor or resonance frequency. It is given by the Larmor equation:

$$f_0 = \gamma B_0 \quad (2.1)$$

The effect could be explained in other terms. In the presence of an external magnetic field \mathbf{B}_0 the energy of a magnetic moment μ depends on its orientation relative to the field:

$$E = -\vec{\mu}\vec{B}_0 \quad (2.2)$$

The energy is minimum when the magnetic moment is aligned parallel to the magnetic field and maximum when it is anti-parallel. From the quantum mechanical prospective, when a nucleus is introduced into a magnetic field its magnetic moment will align itself in $2I+1$ orientations relative to the z direction of \mathbf{B}_0 where I is the nuclear spin quantum number. For ^1H $I=1/2$. In this case the allowed energies are given by

$$E_m = -\mu_z B_0 = -m\hbar\gamma B_0 \quad (2.3)$$

Hence for hydrogen there are only two orientations for the magnetic moment μ : 1) a lower energy orientation parallel to \mathbf{B}_0 with a magnetic quantum number $m=1/2$ often referred to as the α spin state and 2) a higher energy anti-parallel orientation with $m=-1/2$ referred to as the β spin state. This is shown at Fig 2.1. These are the Zeeman energy levels.

The frequency f of the electromagnetic radiation used to induce an NMR transition between the Zeeman levels in an external magnetic field \mathbf{B}_0 is found with Larmor equation:

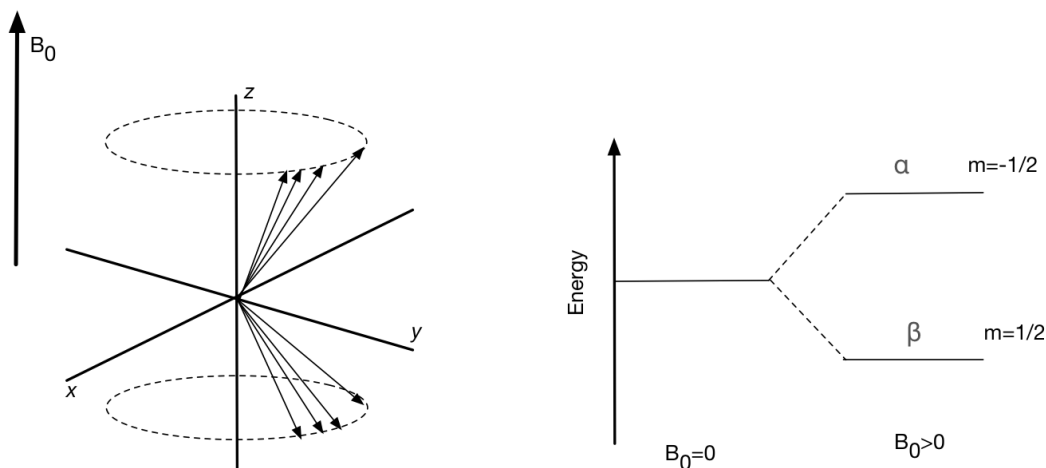


Fig. 2.1 Vector visualisation of spin precession (left) and Zeeman energy levels for nucleus (right).

$$f_0 = \frac{\gamma}{2\pi} B_0 \quad (2.4)$$

where γ is the magnetic ratio of the hydrogen proton, such that $\frac{\gamma}{2\pi} = 42.57$ MHz/T. This is the same as equation 2.2 for the classical picture.

Boltzmann Statistics

In the presence of an external magnetic field different nuclear spin states (with different values of m) have different energies. The energy difference is proportional to \mathbf{B}_0 . At thermal equilibrium, these states will also have different populations, the ratio is given by the Boltzmann equation

$$\frac{N_{high}}{N_{low}} = e^{-\Delta E/kT} \quad (2.5)$$

with N_{high} and N_{low} the respective populations of the upper and lower spin states (such as β and α for an $I=1/2$ nucleus), $\Delta E = E_{high} - E_{low}$ the energy difference between the two states, k the Boltzmann constant, and T the absolute temperature.

FID and 90° excitation pulse

In order to flip the spin of nuclei away from the magnetic field a pulse of electromagnetic radio frequency should be applied at the resonant frequency polarised in x - y plane. The

pulse that rotates the magnetization 90° away from the field alignment with \mathbf{B}_0 consists of a single pulse called P^{90} . It can be of variable duration, but usually it is of an order of few microseconds. If the strength of the electromagnetic field is B_1 then the length of the P^{90} is:

$$t_{p^{90}} = \frac{A}{2\gamma B_1} \quad (2.6)$$

After the P^{90} application the precessing magnetisation generates a current in a coil of a wire around the sample that can be detected as the NMR signal. Usually the same coil is used both for the detection and excitation. The intensity of the detected signal M_0 is directly proportional to the amount of ^1H in the sample. Normally, the signal $M(t)$ decays exponentially with time, so that:

$$M(t) = M_0 \exp\left(\frac{-t}{T_2}\right) \quad (2.7)$$

The signal response detected is called the NMR free induction decay or FID. It decays with time constant T_2 which is known as spin-spin or transverse relaxation time. The T_2 shows how confined and/or mobile the water within the sample is. Loss of signal is due to \mathbf{M} dephasing which is due to inter-nuclear magnetic dipole-dipole interactions. In solids it is microseconds. In bulk liquids it is seconds.

The spins experience both B_0 and B_{local} , small local magnetic fields that due to their neighbours that depend on their local environment. Hence they precess at slightly different rates and loose coherence. This causes a loss of a signal. The loss of signal intensity decays exponentially with time constant T_2 known as the spin-spin or transverse relaxation time. The magnetisation recovers in the z -direction towards equilibrium with B_0 in a time $T_1 \geq T_2$. T_1 is known as the spin lattice or longitudinal relaxation time.

In real experiments, the FID signals decay with the time T_2^* that is related to true T_2 by

$$\frac{1}{T_2^*} = \frac{1}{T_2} + \frac{1}{T_2^{\Delta B}} \quad (2.8)$$

This is because of the loss of magnetisation coherence due to the magnet inhomogeneity which causes dephasing with a time $T_2^{\Delta B}$. Only for short T_2 (i.e. solids) or for very homogeneous magnets $T_2^* = T_2$.

After a pulse, there is a short period of time during which the receiver amplifiers are saturated by the pulse and no signal is seen. This is known as the "dead time". In solids the dead time can be a significant fraction of T_2 .

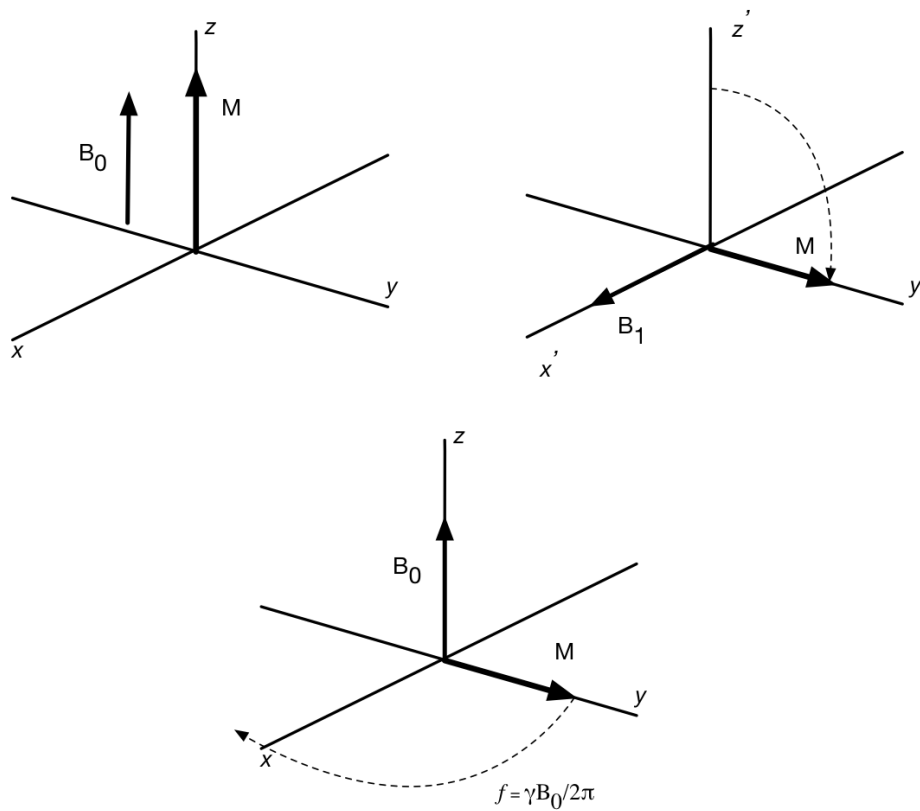


Fig. 2.2 Vector model sketch of the FID pulse. The pulse is shown in a rotating reference frame ($x'y'z'$) that rotates about z of (xyz) at $f_0 = \frac{\gamma}{2\pi}B_0$.

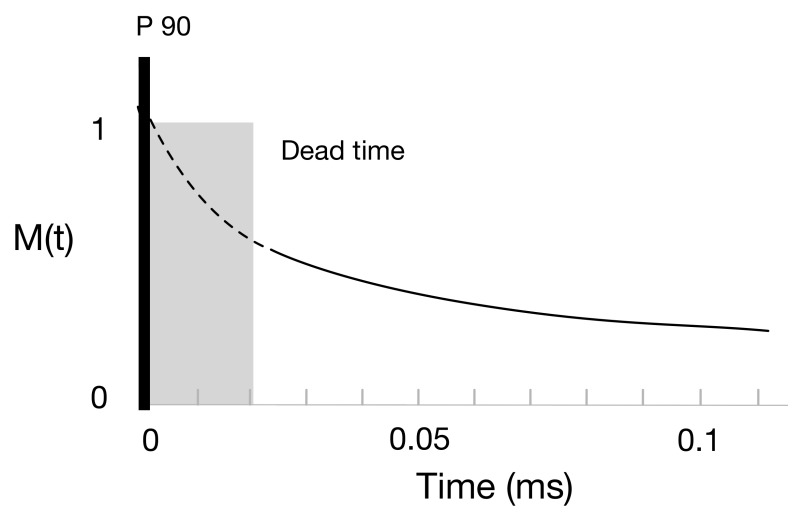


Fig. 2.3 FID is a single pulse, followed by a dead time.

Relaxation in liquids, pores and solids

In free, bulk water all the hydrogens experience the same local field, which due to averaging by molecular motion, is near zero. Thus the relaxation rate is very slow and the relaxation time T_2 is long ~ 3 s for the water at room temperature. If molecular motion is reduced by lowering the temperature or increasing viscosity of the fluid T_2 will reduce.

In crystalline solids the molecular motion is highly reduced. Local fields are strong. Relaxation is very rapid with T_2 of around $10 \mu\text{s}$.

In small pores ^1H relaxation is different in layers of water at the pore surfaces and in the pore core. The relaxation is quick at the pore surface but at the pore core it behaves as a bulk water. Due to the rapid diffusion between the pore core water and water at the pore surface the observed relaxation rate is a weighted average of the surface rate T_2^{surf} and the bulk rate T_2^{bulk} :

$$\begin{aligned} \frac{1}{T_2^{obs}} &= \frac{\lambda S}{V} \times \frac{1}{T_2^{surf}} + \frac{V-S}{V} \times \frac{1}{T_2^{bulk}} \\ &\sim \frac{\lambda S}{V} \times \frac{1}{T_2^{surf}} + \frac{1}{T_2^{bulk}} \\ &\sim \frac{\lambda S}{V} \times \frac{1}{T_2^{surf}} \end{aligned} \quad (2.9)$$

if $T_2^{bulk} \gg T_2^{surf}$, where S is the pore surface area, λ is the thickness of a thin layer of water molecules (usually assumed a monolayer) and V is the pore volume. Hence a measure of T_2 is a measure of pore size if λ / T_2^{surf} is known via calculation or calibration by measurement of a sample dried to monolayer water coverage.

Methods to measure T_2 and T_1

The FID is a one pulse measurement technique that measures T_2^* . In order to measure true T_2 on the low-field NMR equipment multi pulse sequences are used.

The Carr-Purcell-Meiboom-Gill sequence (**CPMG**) is a pulse sequence developed by Meiboom and Gill (1958). As shown in Fig. 2.4 it consists of the P^{90} pulse followed by the number of P^{180} pulses that refocus the magnetization coherence loss due to magnet inhomogeneity, but not due to spin-spin interactions. Pulses are applied at times $\tau, 3\tau, 5\tau \dots$ and series of echoes are obtained at times $2\tau, 4\tau, 6\tau$. The intensity of the echoes decays with time constant true T_2 .

Cement pastes have a big range of pore sizes. In order to cover the whole range of relaxation times CPMG echoes may be logarithmically spaced. With the use of ordinary

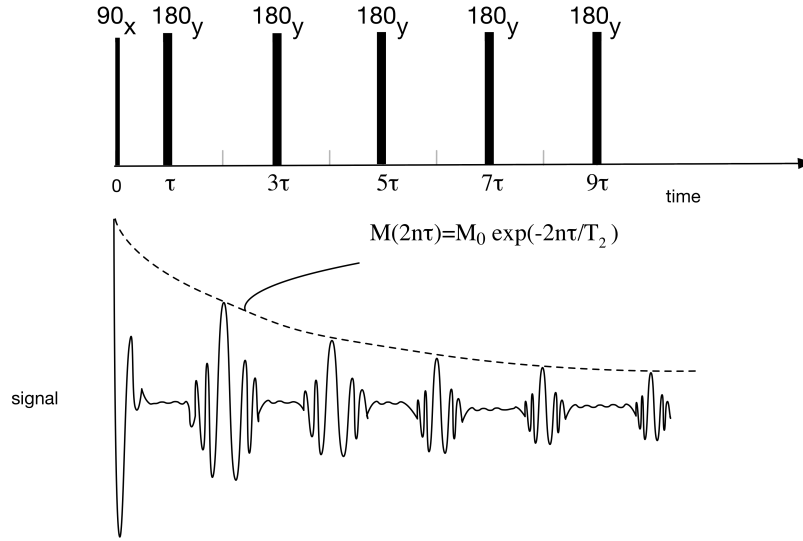


Fig. 2.4 CPMG pulse sequence exhibits with simulated echoes that follow a T_2 relaxation time profile.

linear spacing, too much energy would be put into the system and the sample may heat. This should be avoided during low temperature experiments where temperature stability and control is needed. In addition, power deposition and over use of the coil can cause damage to the NMR spectrometer.

Two methods can be used to measure T_1 . The first method, **saturation-recovery**, consists of the first string of P^{90} pulses that dephase the magnetisation. After a delay τ_{sat} a single P^{90} pulse is applied and the recovered FID signal is measured. The experiment is repeated for different τ_{sat} values in order to build the full recovery curve:

$$M(\tau_{sat}) = M_0 \left[1 - \exp\left(-\frac{\tau_{sat}}{T_1}\right) \right] \quad (2.10)$$

where $M(\tau_{sat})$ is the magnitude of the equilibrium magnetisation recorded along the z -axis and τ_{sat} is a time value of the delay after the first dephasing pulses.

The other method, called **inversion-recovery**, is similar but a P^{180} pulse is used instead of the first dephasing pulses. Inversion-recovery is more sensitive than the first method, however, it is a longer experiment. For the inversion-recovery, a sufficient time needed for the full recovery of the magnetisation between experiments with different τ_{inv} values is required.

The recorded data is given by:

$$M(\tau_{inv}) = M_0 \left[1 - 2 \exp\left(-\frac{\tau_{inv}}{T_1}\right) \right] \quad (2.11)$$

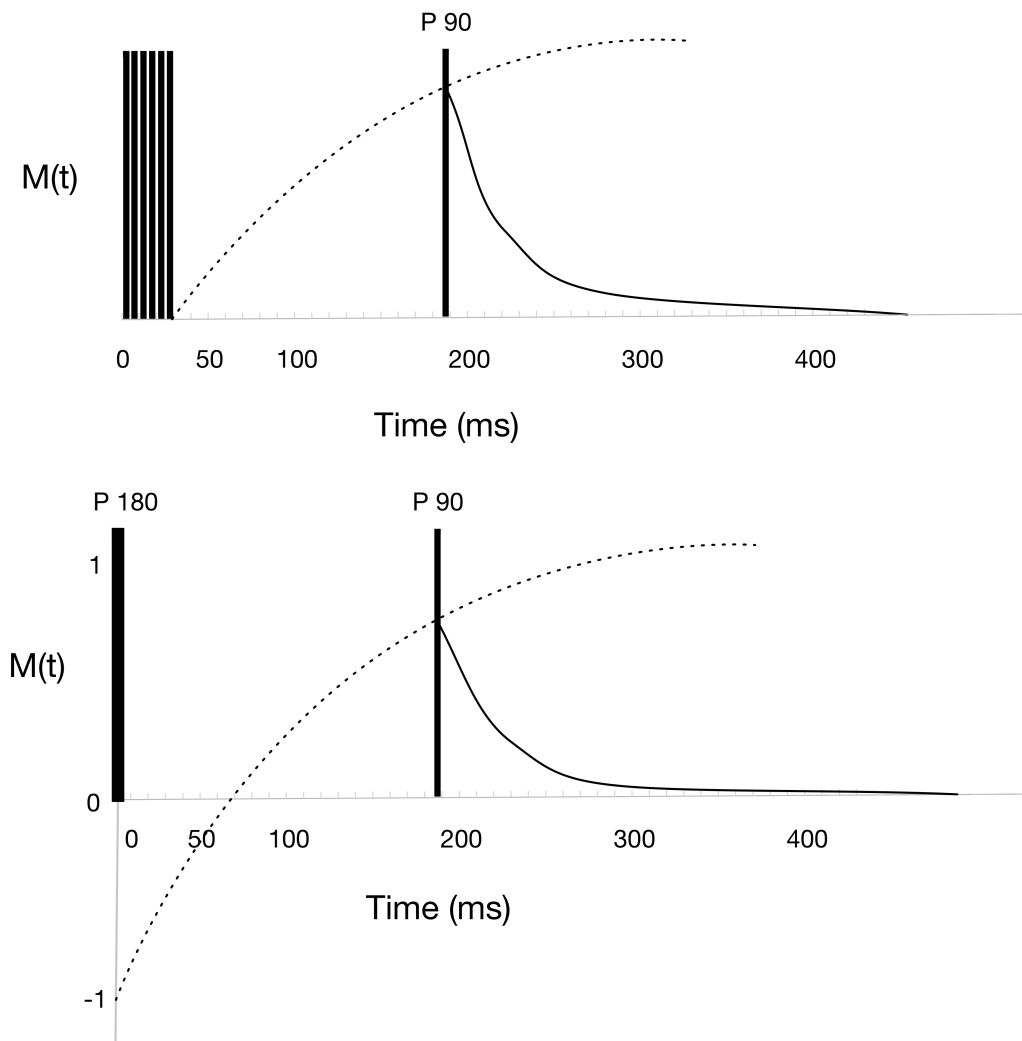


Fig. 2.5 Two methods to measure T_1 . Top: Saturation recovery, bottom: Inversion recovery.

Quad-echo or Solid Echo is an experiment that is used to quantify the amount of crystalline water. Strong magnetic interaction lead to the fast T_2 relaxation in solids that is hidden by the pulse "dead time". Also, the signal originating from solids is so short that it can not be measured by CPMG. The solid echo consists of two P^{90} pulses separated by the gap τ_q . Then P^{90} pulses should be out of phase (Powles and Strange, 1963).

The echo intensity is described as:

$$M_{sol}(\tau_q) = M_{sol}^0 \exp\left[-\frac{(t - \tau_q)^2}{T_{2sol}^2}\right] \quad (2.12)$$

where T_{2sol} is a measure of the solid decay time and M_{sol}^0 is the value of M_{sol} at $\tau_q=0$ which is proportional to the total solid ^1H content.

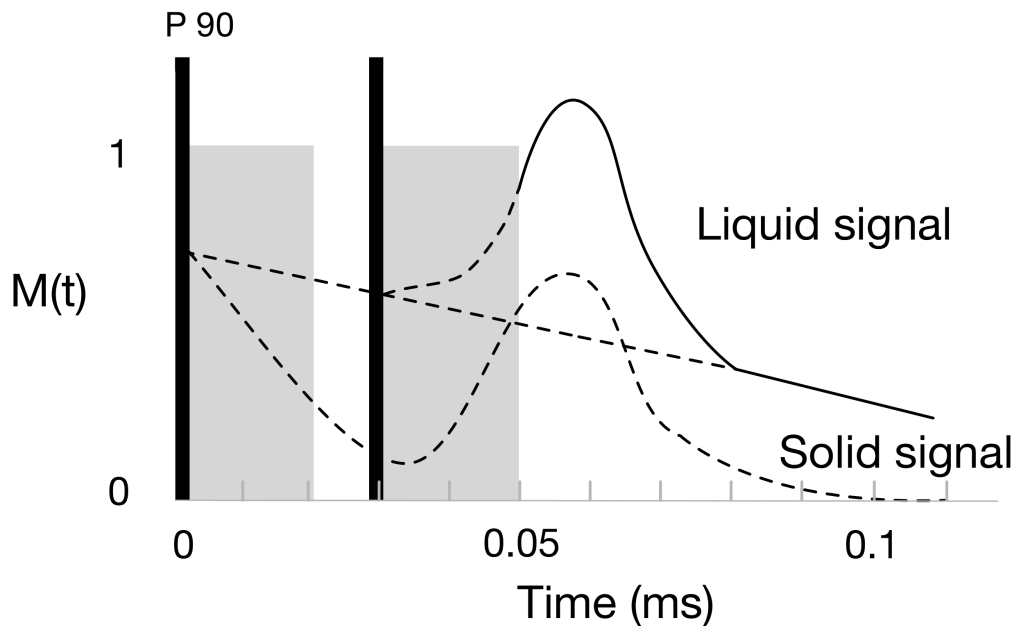


Fig. 2.6 Solid echo.

2D exchange experiment

Two dimensional relaxation experiments are used to investigate water exchange between pores. In 2D $T_2 - T_2$ experiments, T_2 is encoded by 2 CPMG sequences separated by a magnetisation storage interval (Fig.2.7). The recorded T_2 values of two encoding are plotted against each other. If T_2 does not change through the interval time i.e. there is no exchange and diagonal features are seen in a 2D spectrum of relaxation intensities. If it changes the features are off diagonal as seen on the Fig.2.8.

It was noted in the previous section, that T_2 time corresponds to the pore size. If a molecule in the second interval relaxes in the same pore where it has been excited in the first interval, then T_2 relaxation time of two encodings would be identical. If the molecule travels from one pore population to another during the storage time, then T_2 relaxation times in two encodings would be different and plotted against each other would give off-diagonal peaks. Off-diagonal peaks tell us where molecules have moved between the pore populations of different relaxation times. Pore exchange times can be extracted from a measurement of off-diagonal peaks intensity as a function of the storage times.

Callaghan (2011) in his book refers to experiment as REXY (relaxation exchange). Some authors call it T_2 - store - T_2 experiment. In this thesis it is called 2D $T_2 - T_2$ exchange experiment.

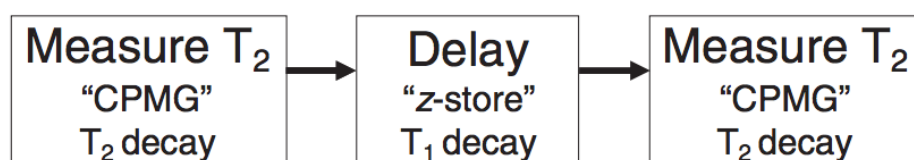


Fig. 2.7 2D ^1H NMR T_2 - store - T_2 consists of two CPMG sequences divided by the varied storage time.

Cryoporometry

Liquids such as water confined in small pores freezes/melts at a lower temperature than the corresponding bulk liquid.

NMR allows separation of a solid phase and a liquid phase via their very different T_2 (long for liquid, short for solid) Mitchell et al. (2008). Thus it is possible to detect the temperature at which the solid-liquid phase change happens in pores through the change in T_2 . In a typical experiment, the sample saturated with liquid is cooled down until the liquid is completely frozen. Then is warmed slowly until the liquid is fully molten again. The NMR signal intensity of the long T_2 component (or the long T_2 fraction) of the liquid phase is recorded on warming. The solid-liquid phase change results in a measured long T_2 signal intensity rise. The signal intensity vs temperature curve can be analysed to calculate corresponding pore size, since melting point depression inversely proportional to the pore size:

$$\frac{dv}{dx} = \frac{dv}{dT} \frac{k_{GT}}{x^2} \quad (2.13)$$

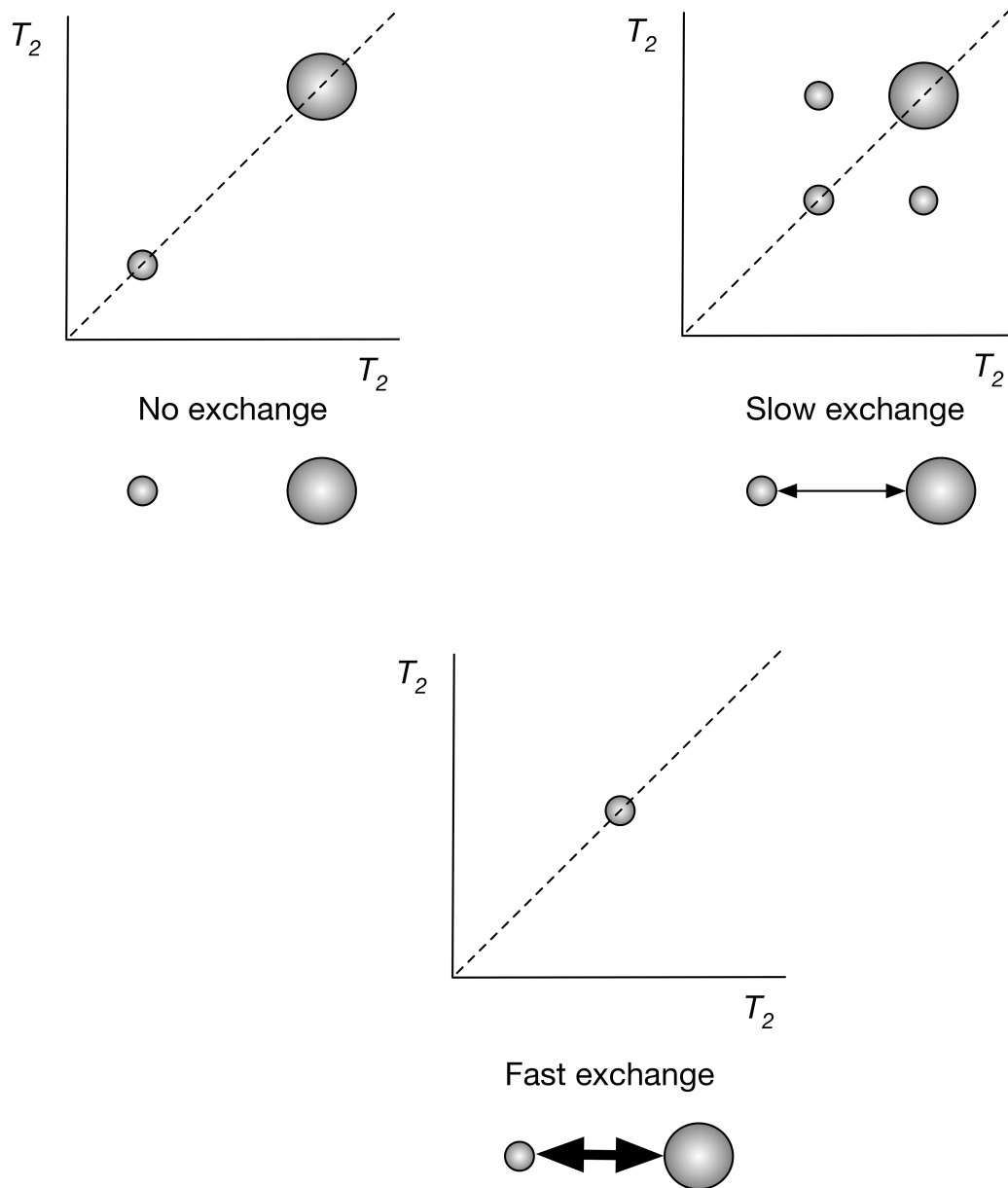


Fig. 2.8 Different exchange patterns as seen by $T_2 - T_2$ exchange experiment.

where v is the volume of liquid in pores with a dimension less than or equal to x . After a small increase in temperature dT , the total volume will increase by dv and then will represent a volume of liquid in pores with dimension less than or equal to $x + dx$. k_{GT} is the Gibbs-Thomson coefficient for the liquid in the pores. The pore size distribution dv/dx can be obtained from the slope of the curve of signal intensity against T .

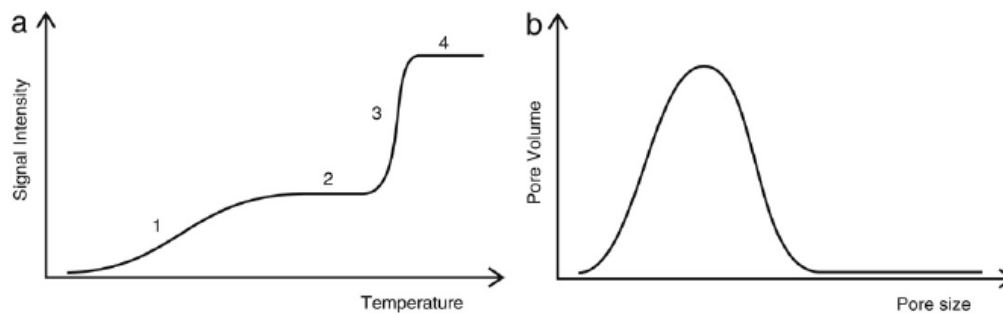


Fig. 2.9 (a) An ideal NMR cryoporometry melting curve with four main features: (1) pore melting step; (2) total pore volume plateau; (3) bulk melting step, and (4) total liquid volume plateau. (b) The pore distribution derived from the melting curve. Graphs reproduced from (Mitchell et al., 2008).

Different researchers used different liquids. Cyclohexane (C_6H_{12}) is a popular choice Petrov and Furó (2009). It has a strong 1H NMR signal. It also has a convenient bulk melting point $T_m = 6.7^\circ C$ and a large melting point depression. It is a non-polar liquid so that molecules do not interact with the surface and confuse the data interpretation. A disadvantage is that C_6H_{12} forms a plastic crystal below the melting temperature T_m of $6.7^\circ C$ that leads to an intermediate T_2 signal that has to be carefully analysed.

Water is another choice, mainly because it is the natural pore fluid of many materials, including cement.

2.1.2 Data Analysis

Data preparation

Firstly NMR data should be phased. The signal has two components recorded along the x' and y' axis of the NMR rotating frame. These are usually called the 'real' and 'imaginary' signals. The phase angle is adjusted for maximum signal in the 'real' channel. In this thesis auto-phasing has been used. However, sometimes raw data is phased manually in order to check auto-phase corrected data. In this case, a few, typically 3 first points are averaged and the phase angle is found as

$$\Theta_p = \tan^{-1}\left(\frac{\langle M_I \rangle}{\langle M_R \rangle}\right) \quad (2.14)$$

where $\langle M_{I,R} \rangle$ is the average of the imaginary and real data point. Thus phase corrected data $\langle M'_{I,R} \rangle$ is:

$$\begin{aligned} M'_R &= \cos(\Theta_p)M_R + \sin(\Theta_p)M_I \\ M'_I &= -\sin(\Theta_p)M_I + \cos(\Theta_p)M_I \end{aligned} \quad (2.15)$$

On other occasion, if the signal to noise is poor it is better to take the magnitude signal $M = (M_I^2 + M_R^2)^{(1/2)}$. However, this can lead to a positive baseline offset error equal to $(M(t \rightarrow 0))^{(1/2)}$.

Echo intensity

Some spectrometers record more than 1 data point per echo and for some data analysis methods it is necessary to average all points in echo in one point. It is needed for the 2D $T_2 - T_2$ analysis. An alternative is to fit a Gaussian-Lense or a SIN curve (liquids) to the echo shape to find the echo intensity.

Inverse Laplace Transform

Inverse Laplace transform (ILT) is actually a multi exponential fitting. However, the algorithm does not assume the number, position and width of the T_2 components. The T_2 distributions in this work were obtained by applying the algorithm developed by Venkataramanan et al. (2002).

The main advantage of the ILT is that it gives an opportunity to analyse any CPMG decay without prior knowledge of the material, i.e. number of the T_2 components.

The main disadvantage, is that it requires a regularisation parameter that should be carefully adjusted. With too little smoothing ILT finds a big number of sharp peaks, but with a lot of smoothing it tends to average all the T_2 components into one wide peak. Venkataramanan provided a scheme to optimise the parameter based on the analysis of the residuals of the fit.

Data in this work always had a signal to noise ratio (SNR) > 500 . This is needed for the correct ILT work. When data has low SNR resultant T_2 distribution will have an artefact. Artefacts usually appear as peaks outside the range of the recorded echo times.

Another problem of ILT is known as pearling. There is a tendency for two close components to be drawn together, raising the relaxation time of the shorter component and lowering that of the longer.

This fitting method is used in this thesis for the well hydrated cement samples as well for the model materials.

Multiexponential fitting

If the number of T_2 components is known and based on previous experience the T_2 values can be reasonably constrained, then multi-exponential fitting can be applied. This method can provide a better consistency in the T_2 values and corresponding intensities from measurement to measurement, especially for the systems with ongoing diffusion process that are not in equilibrium. However, the multi-exponential fitting does not give a T_2 distribution curve that can be visualised.

This fitting is used in the *rewetting* chapter, where measurements were done straight after dry cement samples were measured in the non-equilibrium state.

Exponential stripping

This is a third method, not used in this work. Here a tail of the data decay is fit to a single long relaxation time. This fit is subtracted from the data and the next component fitted in the same way. This is continued until all components are fit.

Chapter 3

Literature review

3.1 Introduction

This chapter reviews current understanding of the growth of C–S–H and of its resultant mesostructure. The application of NMR relaxometry and cryoporometry and other porous media analysis methods to cements are reviewed.

3.2 C–S–H

3.2.1 What is unhydrated cement?

Portland cement is a fine anhydrous powder principally composed of tricalcium silicate and dicalcium silicate with minor fractions of other components such as aluminate and ferric phases. It is made by sintering at temperatures of the order of 1450°C a mixture of limestone (CaCO_3) and source of alumino-silicates such as clay or shale. The product of sintering is called clinker. It is finely ground with other additives such as gypsum to make Portland cement powder. Gypsum helps to control hydration rate.

The four main phases of cement clinker in chemistry notation are tricalcium silicate – C_3S called alite (50-70% of normal Portland cement clinker), dicalcium silicate – C_2S called belite (15-30%), an aluminate phase – C_3A (5-10%) and a ferrite phase – C_4AF (5-15%).

CO_2 is waste product of the sintering. Already introduced here in cement chemistry notation. It is used throughout cement science in order to simplify the use of formulas. The main oxides present in cement expressed in cement chemist notation are given in Table 3.1.

Cement science notation	Chemical composition	Oxide
C	CaO	Calcium oxide
S	SiO ₂	Silicon oxide
A	Al ₂ O ₃	Aluminium oxide
F	Fe ₂ O ₃	Iron (III) oxide
\bar{S}	SO ₃	Sulphur trioxide
\bar{C}	CO ₂	Carbon dioxide
H	H ₂ O	Dihydrogen oxide / Water

Table 3.1 Chemical notation in cement science.

3.2.2 Cement hydration

The principal component and binding phase of Portland cement and thus concrete is calcium silicate hydrate (C–S–H). C–S–H is formed when water and anhydrous cement powder are mixed. C₃S and C₂S together constitute around 70-90% of the cement powder. When mixed with water a chemical reaction takes place (eq. 3.1,3.2).



The exact chemical composition of C–S–H is poorly defined since C–S–H is not a crystalline material. It rather depends on factors as C/S ratio, the amount of water available and other conditions of the reaction as temperature. C–S–H is the main product of cement hydration occupying approximately 50-65% of hydrated paste.

A second product of the reaction is CH (or calcium hydroxide or Portlandite). CH is thought to occur as nano-crystals within and alongside the C–S–H.

Alumina phases give rise to other crystalline solids and ferrite phases such as Aft and Afm. There is also a slightly different material which is aluminum substituted C–S–H (C–A–S–H). Calcium aluminosilicate hydrate is formed when portland cement is hydrated in the presence of Al³⁺ ions, which are present in high quantities when fly ash and slag are dissolved in water.

If there is insufficient water then unreacted cement is left over. If there is too much water, then capillary pores are left filled with H₂O. Also, when hydrates form, there is chemical shrinkage which creates capillary voids that are left empty of water.

The water (w) to cement (c) ratio required for full and complete hydration using all the available water is about 0.4 w/c ratio by mass.

Generally C-S-H is considered to be based on the tobermorite structure as shown at Fig. 3.1, with repeated layers of CaO octahedra sandwiched between layers of SiO₂ tetrahedra to make layers, with water between the layers. There is further nanoscopic porosity between aggregated layers known as gel porosity.

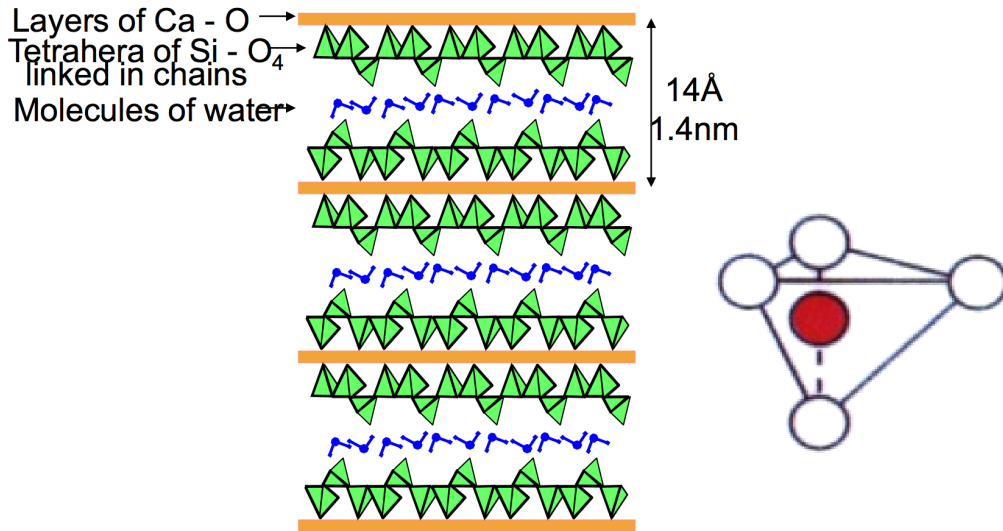


Fig. 3.1 Pore with water confined between the layers of Si atoms. The surface oxygen atoms are tethered and Ca₂⁺ ions are present near the surfaces and are mobile.

3.2.3 Rate growth

C-S-H grows by a dissolution – precipitation reaction during cement hydration. The detailed kinetics is still poorly understood, although it is well established that there is at least one nucleation step. The nano- and meso-structures evidently must depend on the hydration mechanism, but the relationships are not yet established well.

With the use of isothermal calorimetry it is possible to follow the hydration process. Figure 3.2 shows a schematic calorimetry curve of cement hydration divided into different stages. Usually 4 stages could be identified. There is (I) an initial dissolution period, (II) an induction period of a few hours followed by (III) the main period of hydrate precipitation and (IV) deceleration period.

3.2.4 Powers and Brownyard model

In the 1950's Powers and Brownyard developed a model of cement hydration (Powers, 1958) from which they calculated the different fractions of different phases in hydrated cement.

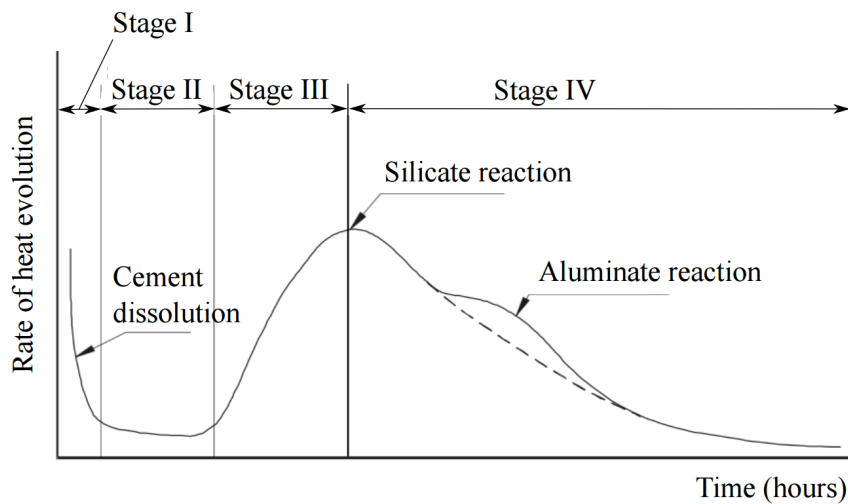


Fig. 3.2 Schematic representation of heat released during ordinary cement hydration: Stage I: dissolution; Stage II: induction period; Stage III: acceleration period; Stage IV: deceleration period.

The model was developed by measuring water vapour adsorption on carefully controlled material of known composition.

The model divides the hydrated cement paste by volume into unhydrated powder, cement gel solids (which includes C–S–H, CH, AFt and AFm phases), gel water, capillary pore water and unfilled capillaries. Fig. 3.3 shows the volume composition as a function of degree of hydration.

They also showed that depending on w/c ratio the capillary pore content varies. As shown in Fig. 3.3 with less water available, capillary pores are occupied by the hydration products. With more water available capillary pores are filled with water not used in hydration.

It should be noted that this model of hydration assumes that product volume is proportional to degree of hydration so the plot has straight lines.

3.2.5 C–S–H models

The microstructure of C–S–H is a subject where cement science continues to have controversy and uncertainty. At the same time it is probably one of the most important factors for the determination of water transport properties.

It is known that C–S–H is nano to meso porous (1-100 nm). Over the years there have been a number of proposed models for the meso-structure of C–S–H. The way C–S–H grows

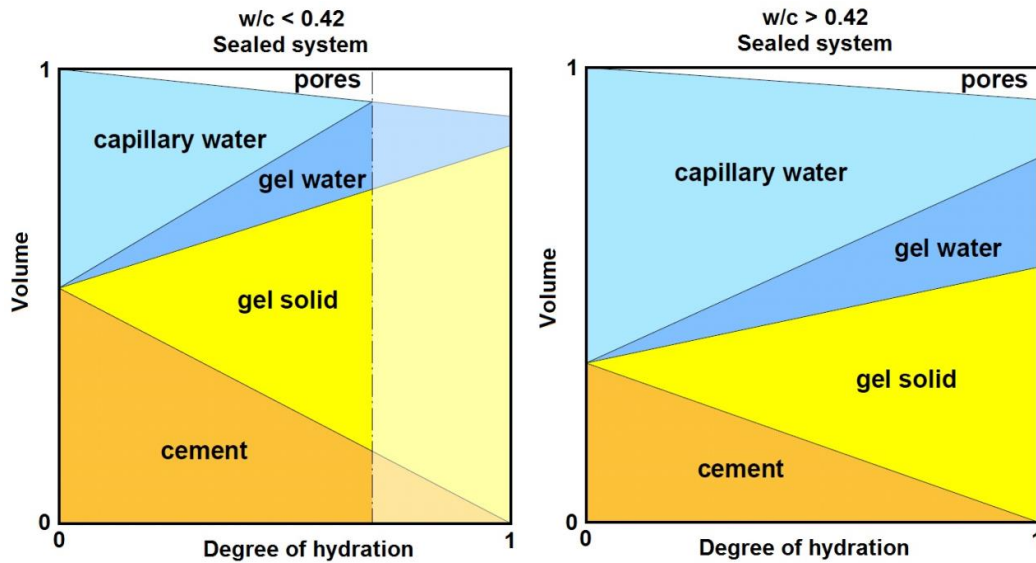


Fig. 3.3 Volume phase composition diagrams by Powers for sealed cured cement paste as reworked by Jensen (2005). The dashed line in the graph for $w/c < 0.4$ indicates the degree of hydration at which hydration stops due to insufficient amount of capillary water.

and its internal pore space has been much debated over the years. There are two very different broad concepts of the nano-structure.

Feldman Sereda model

The first serious model was proposed over 30 years ago by Feldman and Sereda (1970). Their proposal is that C-S-H comprises a 3 dimensional network of quasi continuous, disordered layers as shown in Figure 3.4. Gel pores are spaces between regions of disordered layers.

The idea of quasi-continuous sheet growth structure was developed by Gartner (1997). However it was not until very recently that a successful numerical simulation of this kind of growth was achieved in 3 dimensions by Etzold et al. (2014) The results were qualitatively in-line with the small-angle neutron scattering data gathered by Allen et al. (2007), with calorimetry data and with NMR porosity data. As the sheets are of the order of 1.4 nm thick, so the gel pore must be a few nm also.

3.2.6 Jennings

Another very popular, conceptual model of C-S-H mesostructure is a colloidal structure, such as that proposed by Jennings (2008). Here C-S-H comprises aggregated colloidal particles made up of small tobermorite like layers (Fig. 3.5). Jennings perceives a hierarchy of pore sizes ranging from spaces between disordered sheets in particles, through to spaces

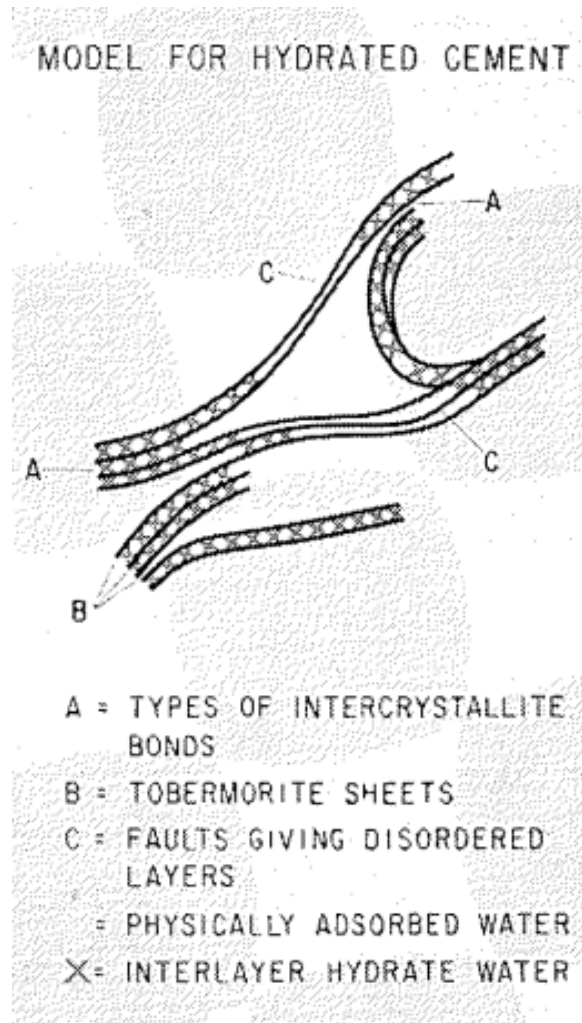


Fig. 3.4 Feldman and Sereda (1970) model.

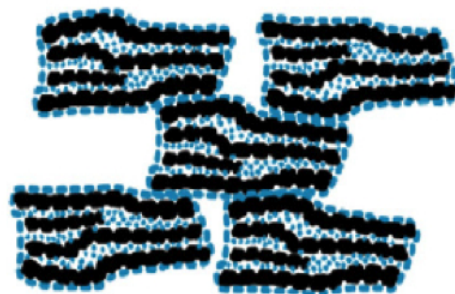


Fig. 3.5 Jennings colloidal model (Jennings, 2008)

between particles in aggregated particle flocs and larger spaces between flocs. The particle sizes can be fine tuned so that the model agrees with a broad range of experimental data.

However, one of the problems with this model is that it can never have a sufficiently low permeability for a colloidal packing. Also it is difficult to understand how it grows.

3.2.7 Cement porosity

The essential point of difference between the colloidal and quasi continuous model is whether there are small bricks of C–S–H that do not connect to each other or whether we have sheets that extend from one region to the next. Either way, there are nanosized pore within the gel that are called gel pores.

On the micro-level, there are also larger interhydrate pores, and filled capillary pores and air voids due to chemical shrinkage of reacting cement and water.

3.3 Methods to measure cement porosity

3.3.1 MIP

Mercury Intrusion Porosimetry (MIP) is a method based on the idea that mercury does not wet the surface of cementitious material and therefore requires an overpressure to force it into a small pore. First the sample is dried. The test dried cement sample is placed into a degassed chamber. Mercury is applied with the increasing pressure until it enters the pores. The pore size can be calculated with the Washburn equation:

$$d = \frac{4\gamma_s \cos(\Theta_c)}{p} \quad (3.3)$$

with d - diameter of pores, p - applied pressure, γ_s - mercury surface tension and Θ_c - is the contact angle between mercury and pore surface.

The main disadvantage of this method is that the sample must be dried. This may damage the structure, as may the excess mercury pressure. Also, it measures the pore throat size and a big pore may hide behind a small pore.

3.3.2 BET

Brunauer–Emmett–Teller (BET) theory (Brunauer et al., 1938) explains the process of gas adsorption onto pore surfaces. This theory is used in the gas sorption analysis technique. The test is made on a dried sample, in the degassed chamber. By forcing nitrogen gas into the chamber, the mass change of the sample is monitored as the function of the nitrogen pressure.

Sometimes water vapour is used, instead of nitrogen gas. The obtained sorption isotherm allows calculation of specific surface area, open porosity and pore size distribution.

This method has similar disadvantages to MIP, especially the prior test sample drying.

3.3.3 LTC

Low Temperature Calorimetry (LTC) is a cryoporometry method. It relies on the fact that a liquid in a pore freezes at a lower temperature compared to the same bulk liquid Wu (2014). The general principle of LTC is very similar to the NMR cryoporometry discussed in the next section except that it uses calorimetry to measure the liquid-solid phase change.

The main advantage compared to the previous techniques is that this method can be applied without prior drying. A sample is placed into the LTC machine at room temperature. Then during slow (4°C per hour) continuous decrease of the temperature, the heat flow of the sample is recorded. At a given temperature, around -60°C warming starts and heat flow is recorded again. Resultant melting curve with peaks, that are associated with water freezing/melting in pores of different size is recorded. The pore size distribution curve is calculated via Gibbs–Thomson equation:

$$\Delta T_m(x) = T_{mB} - T_m(x) = T_{mB} \frac{4\sigma_{sl}}{H_f \rho_s x} \quad (3.4)$$

as given by Jackson and McKenna (1990) where: T_{mB} is a bulk melting temperature, $T_m(x)$ is the melting point of crystals of diameter x , σ_{sl} is a solid–liquid interface energy (per unit area), H_f is a bulk enthalpy of fusion (per gram of material) and ρ_s is a density of solid.

The primary difficulty is calibration for a specific liquid-material system.

3.3.4 Disadvantages

These methods are well developed and used in the laboratories on the regular basis. There are a number of papers that show good data on porosity of hydrated cement pastes obtained with BET (Hall and Hoff, 2011; Johannesson and Utgenannt, 2001), LTC (Wu et al., 2015) and MIP (Gallé, 2001). However, there are some major disadvantages in using these techniques that should be considered.

The biggest problem is that first two of these techniques require sample drying prior to the test. Drying potentially damages the delicate nano structure of the cement-paste. Smaller pores may collapse causing irreversible damage (Taylor, 1997). Another disadvantage is that some inner disconnected porosity (if any) is inaccessible for these conventional techniques

(Hall and Hoff, 2011). None of these methods is easily applicable to the study of pore connectivity save that there has to be an entry to the pores to allow egress / ingress of fluid.

3.4 Meso-structural models of cement

3.4.1 Structure

During the 1990's at Swiss Federal Institute of Technology in Lausanne (EPFL) a model that simulates hydration of C_3S was developed by Navi and Pignat (1996). This resulted in the so called μ IC meso-structural model of cement by Bishnoi and Scrivener (2009). The μ IC model is a vector based model that grows hydrates on the surfaces of hydrating cement particles. Hydrates thus form in shells with spaces between. This model is very successful in getting the composition correct. Other, similar but less successful models are CEMHYD3D developed by Bentz (1997) and HYMOSTRUC3D developed by Van Breugel (1995).

3.5 NMR

3.5.1 Relaxometry

The first relaxation analyses of cements were made by Blinc et al. (1978). The study was performed on both C_3S and Portland cement mixed with water at $w/c=0.4$. They were monitoring T_1 and T_2 relaxation time changes with hydration. The first attempt to relate T_2 obtained with the CPMG experiment to the pore size was made by Halperin et al. (1994). Halperin et al. (1994) could only identify 2 pore sizes after 59 days of hydration due to the equipment used and method limitations. They showed that there is change in both T_2 times and in the amplitudes during the hydration of cement with the longer component amplitude decreasing in favour of the shorter T_2 component. T_2 times decreased throughout showing a reduction in pore size.

A later study by Bohris et al. (1998) attempted to see the difference in T_2 times, depending on the curing temperature and water to cement ratios (w/c). In their work, they reported 3-pore sizes in a hydrated cement sample.

Greener et al. (2000) monitored the hydration of the white cement and corresponding T_2 evolution. In this study three T_2 components were identified: one for the bulk water and two for the pores in C-S-H. Pore gel water with short T_2 and pore water with longer T_2 .

A key requirement for quantitative work is to detect the crystalline solid components such as, calcium hydroxide and ettringite. The first authors to make an assignment of signals

consistent with current understanding were Holly et al. (2007). Apart from solid, three liquid component were detected: the calcium silicate hydrate interlayer water (short T_2), gel pore water (intermediate T_2), and capillary pore water (long T_2). This assignment of T_2 component in hydrated cement paste is inline with current understanding.

In a later study McDonald et al. (2010) progressively dried out cement paste and by mapping the solid to liquid water signal ratio to the water content calculated pore sizes from the signal intensity and ratio. Two C–S–H pore sizes were found, 1.5 nm and 4.1 nm.

In most recent work, which is a part of the TRANSCEND project, Muller et al. (2012) measured the evolution of T_2 times as a function of age and as a function of equilibrated humidity. Muller et al. (2012) reported a number of T_2 components, that are assigned to Portlandite with T_2 about 10 μs , C–S–H inter-layer space water with T_2 about 110 μs and the gel pore T_2 about 330 μs . The next T_2 circa 1 ms correspond to the inter-hydrate pore water. In addition, they have found a T_2 component, longer then inter-hydrate and assigned it to the micron size capillary pores. In this work two main outcomes were reported: C–S–H density was calculated and Powers and Brownyard's model was updated. Powers and Brownyard's models of hydration was shown not to be linear (straight lines on the model graph), as was assumed in the original work.

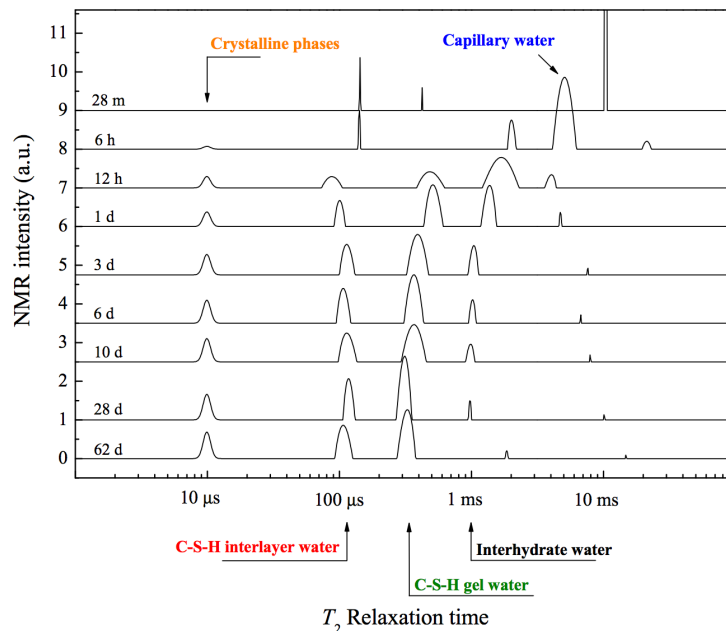


Fig. 3.6 Evolution of the NMR signal during hydration for the water to cement ratio $w/c = 0.40$ paste. Combined QE and CPMG results (Muller, 2014).

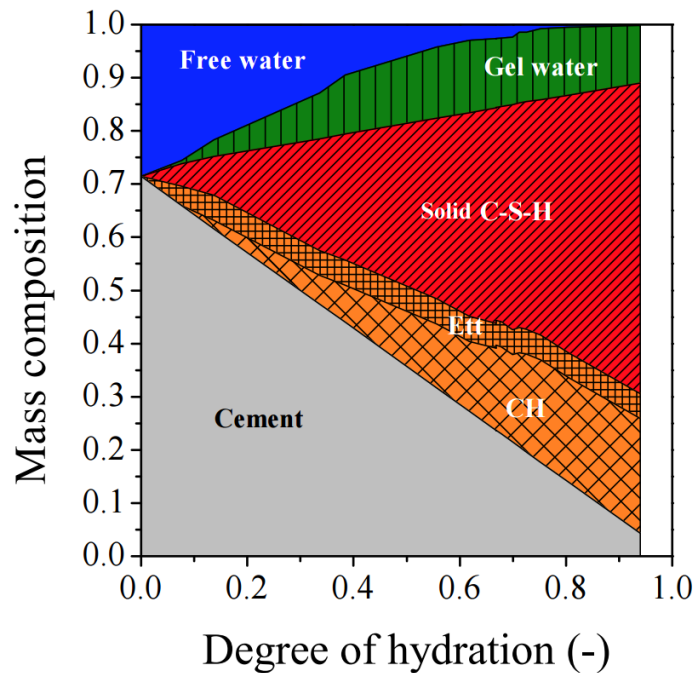


Fig. 3.7 Revised Powers and Brownyard model: mass composition of cement paste for $w/c = 0.40$ (Muller, 2014).

A later study by Muller et al. (2013) was done for mature white cement pastes as a function of relative humidity and hence yielded an NMR derived, pore size specific desorption isotherm.

The same group used double-quantum-filtered (DQF) NMR technique to study lateral size of sheet pores (Rodin et al., 2011).

An NMR technique called PFG (pulse field gradient) diffusometry has been applied to hydrated cements by Nestle et al. (2007). Compared to work above, this technique required more sophisticated equipment. The apparent diffusion coefficient is measured as a function of diffusion time. Due to restricted diffusion in pores it gives the pore size. Nevertheless, it has been showed that this experiment can be valuable for waste management studies.

Magnetic resonance imaging (MRI) studies of water transport and non-spatially uniform hydration in cements have been performed by different groups. In a study performed by Bohris et al. (1998) it was shown, that water transport is reduced with the w/c decrease. Balcom et al. (2003) applied MRI to demonstrate that it is possible to visualize the internal moisture distribution in concrete and even spatially resolve the freezing behavior of concrete.

Application of GARField (standing for Gradient at Right Angles to Field) NMR by Zamani et al. (2014) measured the water cement relative permeability as a function of relative humidity (RH).

In other NMR study done by Kowalczyk et al. (2014) hydrated cement paste was exchanged with isopropanol. In this work the interconnectivity of interlayers and gel pores with large interhydrate pores and capillary voids was demonstrated experimentally for the first time.

3.5.2 T_2 - T_2 exchange experiments

The idea of a 2D experiment was first proposed in a paper by Peemoeller et al. (1981) but the method was not taken up as there was no reliable means to perform a 2D inverse Laplace transform of data until the method of Venkataramanan et al. (2002).

Works by Monteilhet et al. (2006) and McDonald et al. (2007) were the first to apply 2D methods quantitatively to cements. These works showed evidence of the existence of the water exchange between inter-layer and gel pores in the first week of hydration. Resultant from these papers is the picture of water dynamics in C-S-H current at the outset of this work. Water moves across the C-S-H pore surface with a hopping time of circa 1 ns. It is adsorbed for circa 10 μ s after which it (re)-enters the pore bulk water. Water in interlayer and gel pore spaces exchange with a time constant of about 5 ms.

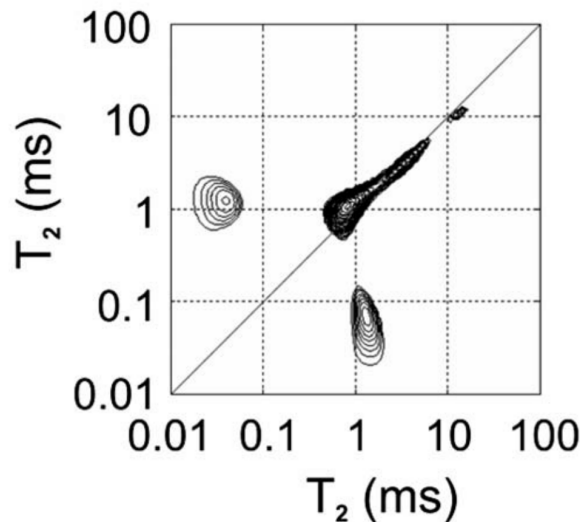


Fig. 3.8 Experimental T_2 - T_2 2D correlation spectrum for a white cement paste with w/c ratio 0.4 and three days old. The storage time is 10 ms. Adapted from McDonald et al. (2007)

3.5.3 NMR Cryoporometry

NMR cryoporometry is a technique that uses NMR in the way similar to LTC. The T_2 of solid is very rapid, thus need not be detected by the NMR spectrometer, but when the melting in the pores occurs a liquid water T_2 in the pores can be detected.

The first NMR cryoporometry was performed by Strange (1994). He noticed that data should be collected on melting (warming). In addition, it was noticed that excellent temperature control is essential if accurate pore size distribution is needed especially for over 100 nm in size.

There are two ways of conducting the experiment – scanning measurements with continuous temperature rising or with a discontinuous, step like temperature rise, Mitchell et al. (2008). In later works it is noted, that use of relaxation filter is needed especially for liquids such as cyclohexane, Petrov and Furó (2009). A pulse sequence with relaxation delay was introduced in order to catch the liquid only signal, Petrov and Furó (2009).

Valckenborg et al. (2002) recorded full CPMG echo trains in cryoporometry experiments, and thus combined cryoporometry and relaxometry for the first time. The further combination of two techniques discussed later in details.

One of the first attempts to measure the pore size distribution of cements by cryoporometry was done by Filippov and Vartapetyan (1997). In their work, they used cyclohexane as adsorbate. Later work by Leventis et al. (2000) was done on cements in its natural saturated with water state. They detected water in C–S–H gel of 1.8 nm and a broad distribution of pore sizes between 6–40 nm. Valckenborg et al. (2002) compared pore size distribution from NMR cryoporometry and NMR relaxometry of a mortar sample. Both techniques detected three discrete pore sizes.

3.5.4 Combined relaxometry and cryoporometry

Combining relaxometry and cryoporometry a very interesting synthesis can be achieved. The first application of the combined technique was shown by Valckenborg et al. (2002). Porous glass with controlled 5 nm pores saturated with water was used.

It can be seen on the Fig. 3.9 how water in pores start to melt at around -19°C and thus T_2 changes toward longer values. Existence of the plateau at -4°C to -3°C means that all the water in pores is melted.

A further attempt to combine relaxometry and cryoporometry was made by Mitchell et al. (2005) on the mono sized sample saturated with cyclohexane. However, the results obtained are not straightforward to interpret. For example, two different reference samples saturated with cyclohexane, show different T_2 patterns on melting. The main difficulty is that

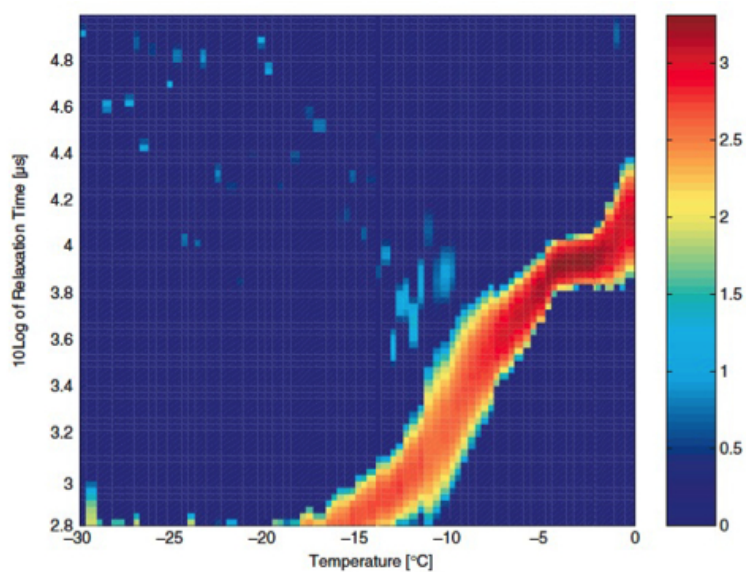


Fig. 3.9 Intensity plot of the combined relaxometry and cryoporometry measurements. Blue denotes low intensity and red denotes maximum intensity of the NMR signal. Valckenborg et al. (2002)

cyclohexane forms a plastic crystal phase at just below melting and this signal is difficult to separate from liquid and solid. This is not the case for the ice-water separation.

Chapter 4

Technique development

First tests on the NMR kit showed that there was a need of a calibration of the pulse sequences and temperature control. Thus a decision has been made to start from the scratch. The purpose of this decision was to make sure that the basic parameters are calibrated and are inline with the other NMR kits used in the project: one at Surrey and other at EPFL.

4.1 Coil height

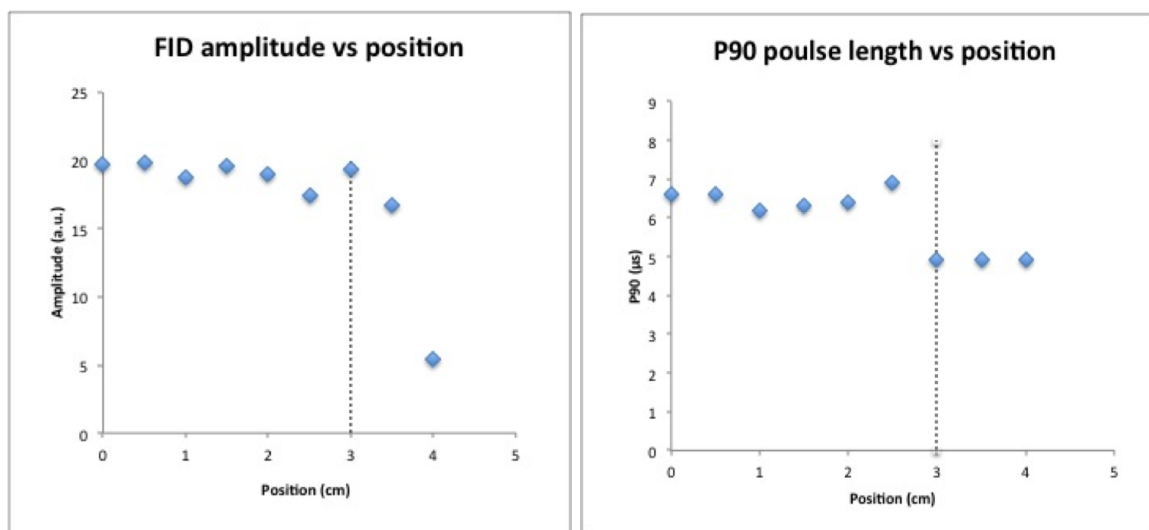
The coil height determines a sample's maximum length. A test was carried out to find out its height as follows: a capillary tube with 0.5 cm of water in height, was placed at the very bottom of the coil. While the capillary tube was gradually lifted the signal intensity was measured. A drop in intensity was detected over 3 cm above the coil's base. These results confirmed manufacturer's value of the coil's length of 3 cm.

As it was mentioned in *Theory* section good temperature stability is essential for the cryoporometry measurement. It is possible with the use of thermocouples to directly monitor temperature in the sample. With more than 1 thermocouple it is possible to record temperature at different heights of the sample and track a temperature gradient. However, the thermocouple cannot be used during data acquisition as they introduce noise.

The NMR thermometer is situated just a few centimetres below the sample. Data from the thermocouples compared to the NMR thermometer values makes it possible to derive fit formula. This relation is needed to calculate 'real' temperature in the sample based on the information from the thermometer.

For this check a 'texto 177-T4 Data Logger' thermocouple was used. This thermocouple allows to work in the temperature range from -195°C to $+1000^{\circ}\text{C}$.

A number of experiments were performed. Here we only highlight the main results.



(a) Signal strength vs. coil depth

(b) P_{90} pulse length vs. coil depth

Fig. 4.1 Results of the test on the hardware height limitation.

4.1.1 3 days old cement paste with water to cement ratio 0.4 with 2 thermocouples.

Cement paste was kept underwater for 3 days. For the test two holes at the bottom and at the top of the sample were drilled. Thermocouples were placed in such way that they would align along the central axis of the cylindrical sample. The cryoporometry experiment was performed with the data logging on thermocouples every second. On the final plot, results were compared to the temperature obtained from the NMR thermometer. On the Fig.4.2 it can be seen, that for the temperature set up at $-35\text{ }^{\circ}\text{C}$ on the machine, 'real' temperature of the sample is different. Between bottom thermocouple and upper thermocouple (0.5 cm between them) there is about $3\text{ }^{\circ}\text{C}$ difference.

It was proposed, that a bulb like shape of the sample cell could reduce the temperature gradient across the sample. The idea was to increase area of contact of the sample with the air flow. So called *BET sample cells* were used to test this proposal.

For the BET cell check, cement paste ($w/c=0.4$) was cast in the tube with two thermocouples inside. In order to prevent direct contact of thermocouples with the paste they were isolated with the PTFE tape.

The downside of the BET sample cells, compared to the ordinary test tubes is that sample preparation becomes more complicated due to the casting of the paste inside the tubes i.e. delivering paste at the bottom of the cell through a small radius entrance.

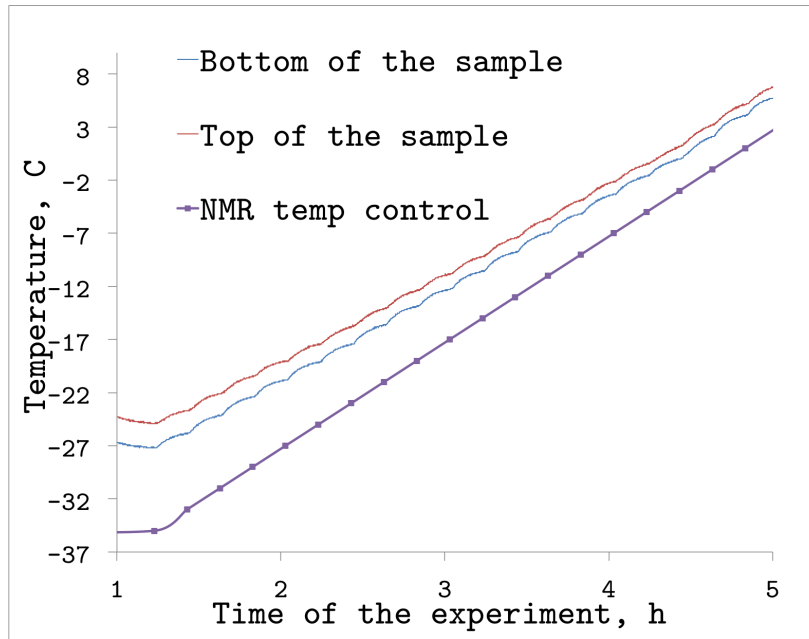


Fig. 4.2 3 days old cement paste $w/c=0.4$ with 2 thermocouples attached

At the lowest temperatures, gradient (difference between the temperature at the top and at the bottom of the sample) was $\Delta T=0.8^{\circ}\text{C}$ and at close to 0°C gradient was $\Delta T=0.3^{\circ}\text{C}$ as seen at Fig.4.3. The existence of a such temperature gradient is acceptable for the current research. However, for the systems with larger pores then C-S-H pores sizes a finer temperature set-up would be needed.

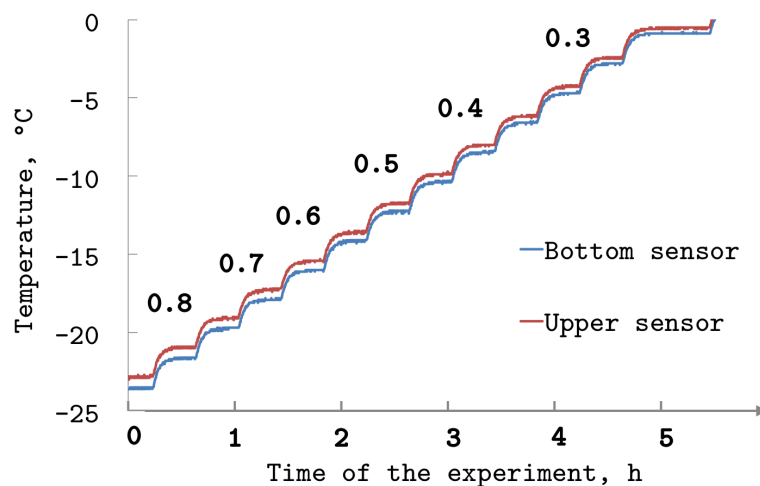


Fig. 4.3 Cryoporometry on cement paste in the BET tube. Numbers above the curve represent temperature gradient between 2 thermocouples.

4.2 Thermal equilibrium

The cryoporometry experiment can be done in two ways: with the continuous increase of the temperature or with the step like procedure. Our experiments imply use of the CPMG pulse sequence, which is not a rapid experiment. That is the reason for a step like increase to be used. From the previous results with the thermocouple, it can be seen that temperature across the sample changes very quickly. However, an experiment was conducted to test thermal inertia of the probe liquid. Different amounts of bulk cyclohexane were warmed after being quenched with equilibrating temperature times varied. From the cumulative plot on Fig.4.4 it can be seen, that with 470 mg of cyclohexane, 10 minutes is a sufficient time to reach equilibrium. When the equilibrating time increased, the melting curve doesn't change. However, when we reduce the amount of the cyclohexane to 146 gr, the scaled melting curve has much sharper melting step. It is plausible, that this happens due to the smaller temperature gradient in the 146 mg sample.

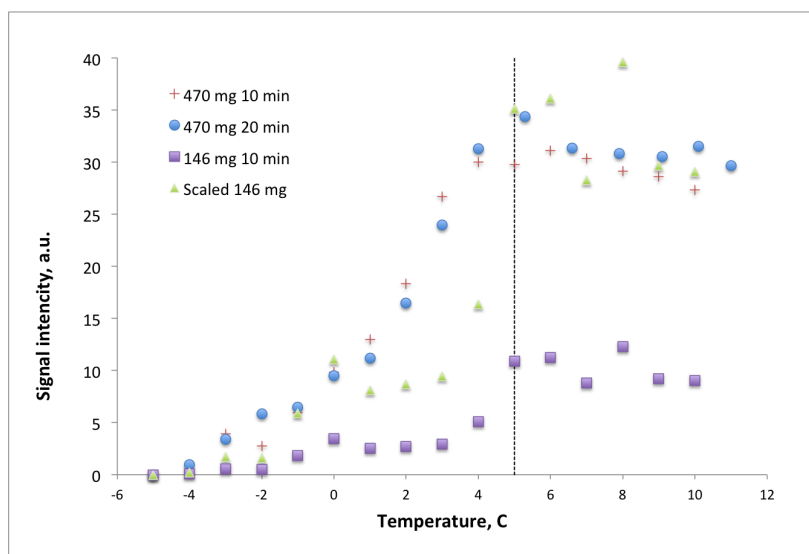


Fig. 4.4 Cryoporometry run on the cyclohexane of different quantities and with different equilibrating times.

4.3 Curie's correction

It is known from the literature, that signal intensity is inversely proportional to the temperature. In order to see the impact of the signal variation with the temperature a cryoporometry run on the non-freezing ethanol was conducted Fig.4.5. An inverse dependency $1/T$ detected.

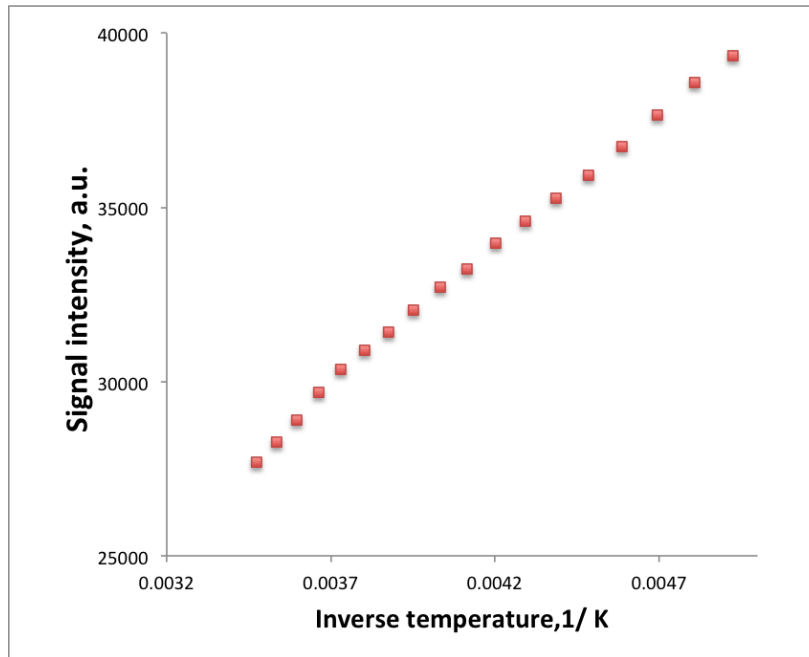


Fig. 4.5 Signal intensity of the ethanol vs. temperature. Intensity dependency on the temperature is called Curie factor. This correction factor should be applied to the cryoporometry data

This correction factor is used during cryoporometry data analysis. Otherwise, calculated PSD would not be correct.

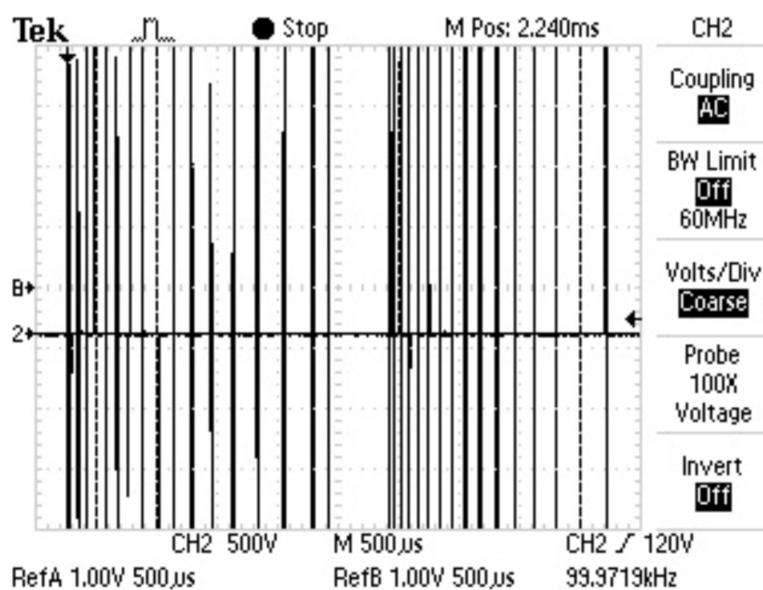
4.4 $T_2 - T_2$ validation

Fig.4.6 shows the P_{90} pulse followed by 15 logarithmically spaced P_{180} pulses followed by the storage P_{90} pulse. A mixing time is followed by the P_{90} pulse and next 15 logarithmically spaced P_{180} pulse sequences.

Saturated with water Alumina with two different pore sizes was used for the validation of the technique. The T_2 of pores and the ratio between the pore volumes (signal from the pores) was known.

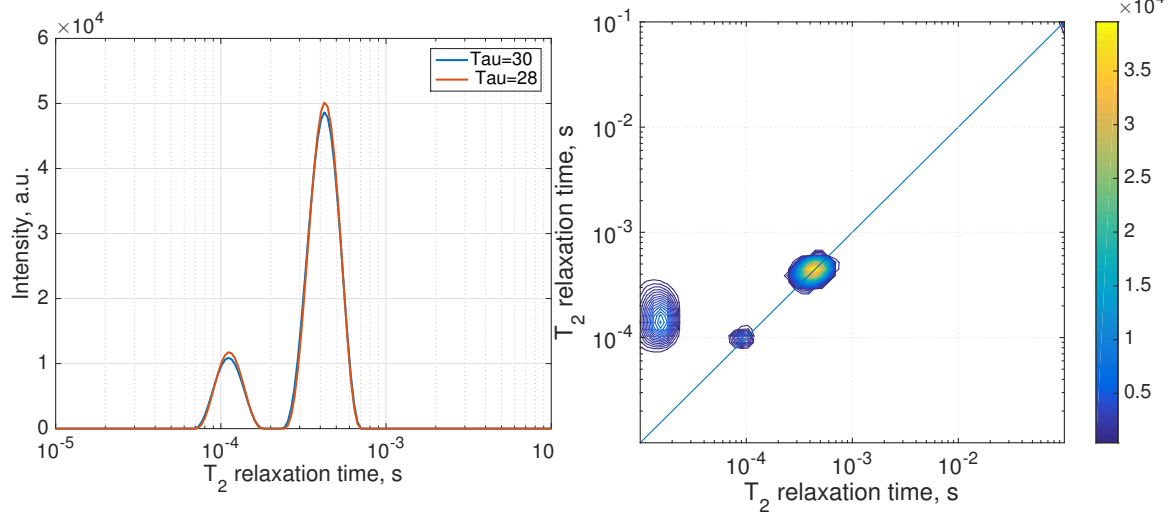
CPMG was performed on the Alumina reference sample and compared with the NMR installed at Surrey. Both results were consistent, T_2 times appeared with roughly same T_2 values of $\sim 120\mu\text{s}$ and $\sim 400\mu\text{s}$. In both labs the ratio of the two intensities was the same.

2D $T_2 - T_2$ was performed on the same material with two storage times: $100\mu\text{s}$ and $500\mu\text{s}$. The on-diagonal peaks appeared at the expected T_2 's. A shorter on-diagonal peak of $\sim 100\mu\text{s}$ has the lower intensity seen in 4.7c than in 4.7b; this happens due to the undergoing T_1 relaxation process during the mixing time period. The off-diagonal peak seen in 4.7c



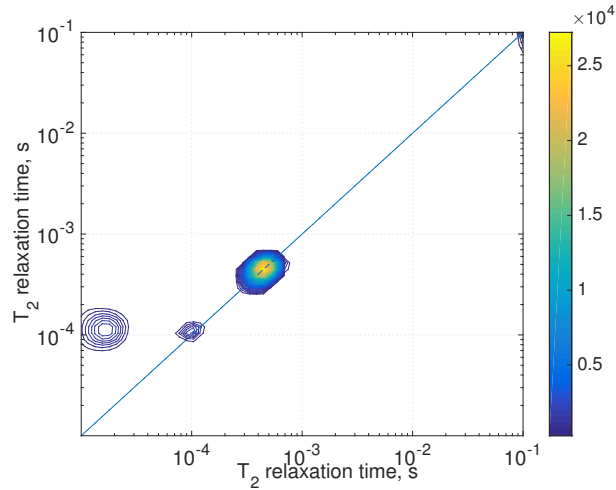
The $T_2 - T_2$ pulse sequence was written in-house, as the Maran-Ultra NMR installed at the LafargeHolcim laboratory could not use the $T_2 - T_2$ pulse sequence from the University of Surrey. Thus, firstly, we have verified the timing of the pulse sequence with the oscilloscope Fig.4.6.

Fig. 4.6 Screen shot of the $T_2 - T_2$ pulse sequence as it can be viewed on the screen of the oscilloscope. Only a limited number of pulses and a short storage time are used for this test.



(a) ILT output of the reference Alumina CPMG experiment.

(b) $T_2 - T_2$ experiment on the reference Alumina with $100 \mu\text{s}$ storage time.



(c) $T_2 - T_2$ experiment on the reference Alumina with $500 \mu\text{s}$ storage time.

Fig. 4.7 Validation of the technique with the referent sample of known two pore sizes.

and 4.7b is an artefact introduced by the software. During the later experiments we would indicate time of the first and the last echo on the figure. This approach makes it obvious that any signal outside these boundaries is an unphysical artefact introduced by the inverse Laplace transformation. The later is known to be an ill-posed problem.

4.5 Conclusions

At the beginning of the EngD project a decision has been made to perform tuning of the NMR spectrometer. Calibration tests very successfully performed. NMR data output was compared with outputs from the other two labs involved in the project EPFL and University of Surrey. It was agreed that NMR was fully operational and experimental objectives of the project could be achieved.

New pulse sequence T_2 - T_2 was introduced at the industrial laboratory. The pulse sequence was verified with the model materials and CuSO_4 doped water.

Chapter 5

Cryoporometry and relaxometry on model materials

In early work on cryoporometry cyclohexane (C_6H_{12}) was used as the probe fluid (Mitchell et al., 2005; Strange, 1998). The main reason is that C_6H_{12} is a nonpolar fluid, which for many applications is an advantage, as it does not get adsorbed to the pore surface. It has a melting point of $6.7^\circ C$ so it is a liquid at room temperature which is a practical advantage. It has an unusually large melting point depression of $K_f = 20^\circ C/m$ which makes the freezing temperature very sensitive to pore size. Finally, the first solid-phase on freezing is a plastic crystal that is sufficiently soft not to destroy the delicate pore nanostructure. However, it is unsuitable for cements where water is the natural fluid of choice notwithstanding it is polar liquid. Also the plastic crystal phase of cyclohexane can make it difficult to differentiate the solid and liquid phases in the CPMG NMR experiment. The fact that water is polar leads to a non-frozen surface layer problem as it will become clear in the results subsection.

In this chapter results of the combined NMR cryoporometry and NMR relaxometry are presented. These work has been done with water and model materials and cementitious materials such as C_2S and C_3S .

5.1 Water in silica glass

5.1.1 Materials and methods

The investigated model materials are: SiO_2 with 8.7 nm pores, SiO_2 with 11 nm pores and MCM-41¹ with 3 nm pores. The materials were obtained from three different producers.

¹MCM-41 is a mesoporous material with a hierarchical structure from a family of silicate and aluminosilicate solids.

Table 5.1 Model materials used for cryoporometry.

Material	Producer	Average pore diameter (nm)	Pore volume (cm ³ /g)	Specific surface area (m ² /g)	Mean Particle Size (μs)
MCM-41	Tianjin Chem Sci	3.0	0.70	≥ 800	-
SiO ₂	Glantreo	8.7	0.5	171	3
SiO ₂	NLAB	11	1.17	710	1.5

The details of the samples can be found in the Table 5.1. Typically 0.1-0.5 gram of the dry powder was saturated with deionized water at room temperature for 2 days. There was a small amount of excess water above the saturated powder in the sample tube equivalent to about 10-20% of the total volume as shown in Figure 5.1.

The pore size distribution analysis for the SiO₂ with 8.7 nm pores was provided by the producer Galantreo. Data in Fig. 5.2 confirms pore width of 8.7 nm.

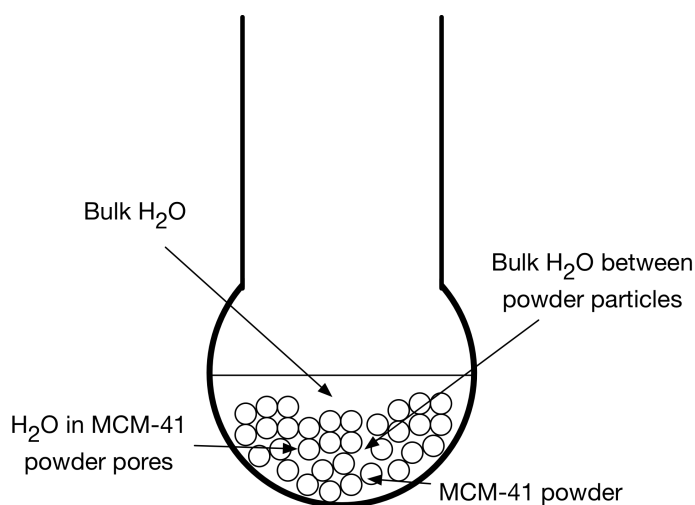


Fig. 5.1 Sample sketch.

The water saturated sample was quenched in liquid nitrogen for at least 10 minutes. This was to ensure that all NMR measurements were made on a warming cycle and so avoided super-cooling effects. The quenched sample was placed in the NMR spectrometer for which the sample space was already cooled to -80°C. The sample was left to equilibrate for 20 minutes at this temperature.

CPMG echo train data was recorded as a function of temperature during a warming cycle. Data was recorded at 1°C intervals. The temperature was left to stabilize for 2 minutes at each new temperature. The NMR parameters are given in Table 5.2.

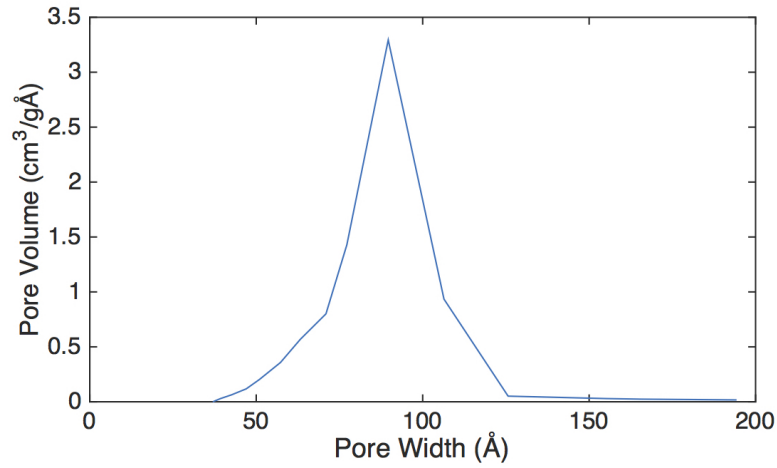


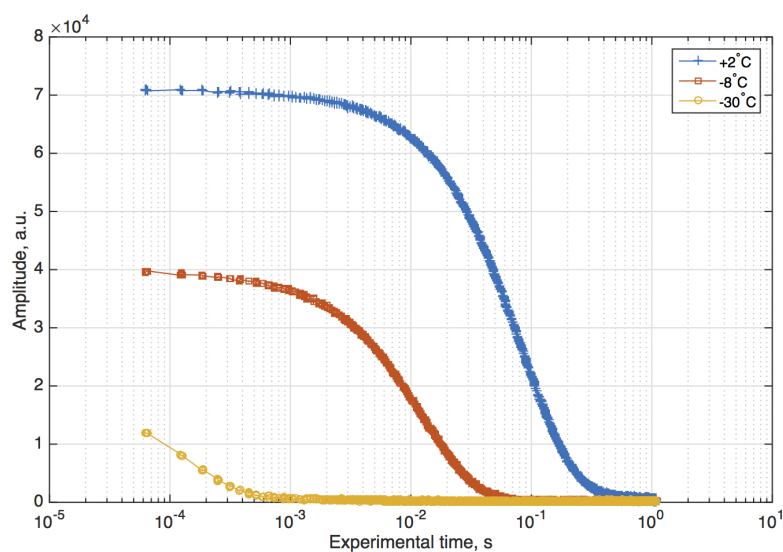
Fig. 5.2 The Barrett-Joyner-Halenda (BJH) analysis results of desorption for the 8.7 nm SiO_2 powder provided by Galanteo.

Parameters	SiO_2 (8.7 nm)	SiO_2 (11 nm)	MCM-41 (3 nm)
Pulse gap, τ (μs)	30	30	30
Number of echoes, N_{echo}	512	320	512
Points per echo, pts/echo	4	4	4
Repetition time, τ_R (s)	0.5	2.5	0.25
Number of scans, N_s	128	64	128

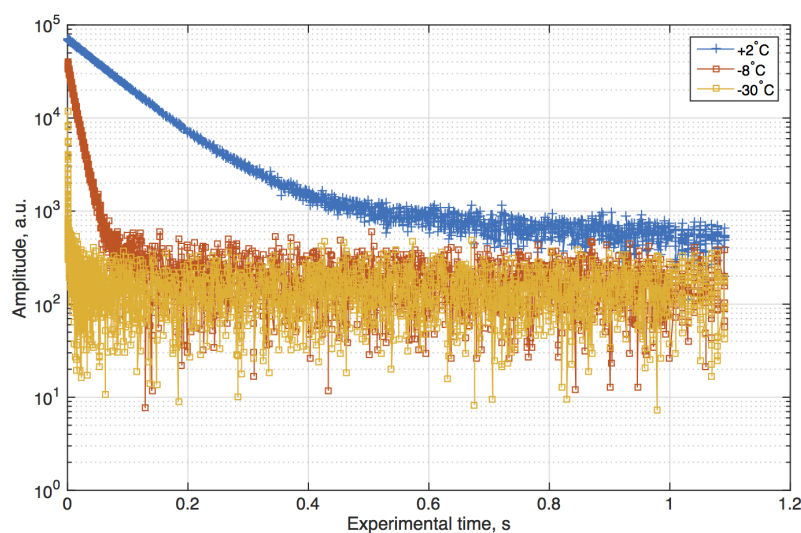
Table 5.2 Parameters of CPMG experiments for silica glasses

5.1.2 Results: 8.7 nm porous glass

Figure 5.3a shows the CPMG echo train decays for three exemplar temperatures recorded in the order -30°C , -8°C and $+2^{\circ}\text{C}$, but discussed in reverse order. The data is shown on a linear log scale. The same data is shown in Figure 5.3b on a log linear scale. The data signal intensities have been corrected by the Boltzmann factor and normalized to account for the temperature dependence of the NMR signal intensity.



(a) Lin-Log plot.



(b) Log-Lin plot.

Fig. 5.3 A (a) Lin-Log and (b) Log-Lin plots of the CPMG traces for three different temperatures for the SiO_2 with 8.7 nm pores, saturated with water.

Table 5.3 Parameters for the single exponential fit of the SiO₂ with 8.7 nm pores, as stated by the producer, saturated with water.

Temperature	Single exponential fit value	Magnitude (Norm, %)
+2°C	88 ms	100
-8°C	12.5 ms	55.9
-30°C	0.236 ms	16.9

The Figure 5.3 shows that at +2°C there is approximately mono-exponential decay with a long relaxation time of the order of 90 ms. A single component exponential fit to the data gives value of 88 ms, Table 5.3. The decay is dominated by the signal from the water that at 2°C is not frozen either in the pores or in the bulk.

At -8°C, the first echo is approximately 55 % of the intensity of the first echo at +2°C. This is because the bulk water outside particles have frozen and now have a relaxation time of only a few microseconds, too short to be seen by CPMG. However, the water in the pores of the SiO₂ powder remains unfrozen. A single exponential decay fitting gives a relaxation time of 12.5 ms and normalized intensity of 55.9% as given in Table 5.3. 55% is reasonable since there is about 20% of the sample volume as water above the powder and for a close packed powder bed there is about 30% of water filled space in the interstitial volume between the grains.

At -30°C there is still some CPMG signal left. It is expected that at this temperature the water in the pores will also freeze. However, the remaining signal suggests that there is a pore surface layer of water that has not frozen. Alternatively this may be a signal from hydrogen associated with silanol groups at the pore surface. According to a single exponential fitting it has a T_2 of 0.236 ms and a normalised amplitude of 16.9%, Table 5.3.

More insight is gained from an inverse Laplace transformation analysis that is essentially a fit of the echo train data to a continuous distribution of T_2 relaxation times. The relaxation distribution for the sample at +2°C is given in Fig. 5.4c. It has one peak. This peak is attributed to the signal of non-frozen water in the sample.

Figure 5.4b shows the ILT distribution of relaxation times for the sample at -8°C. At -8°C the ILT shows again one peak with smaller intensity at shorter T_2 compared to +2°C data. This signal attributes to the water in the pores.

Figure 5.4a shows the ILT distribution at -30°C. At this temperature the water in the pores is frozen and so not seen. The hydrogen associated with the surface remains sufficiently mobile to see. However, the T_2 value is reduced compared to -8°C due to the the lack of averaging with the previously unfrozen water contained in the central pore volume.

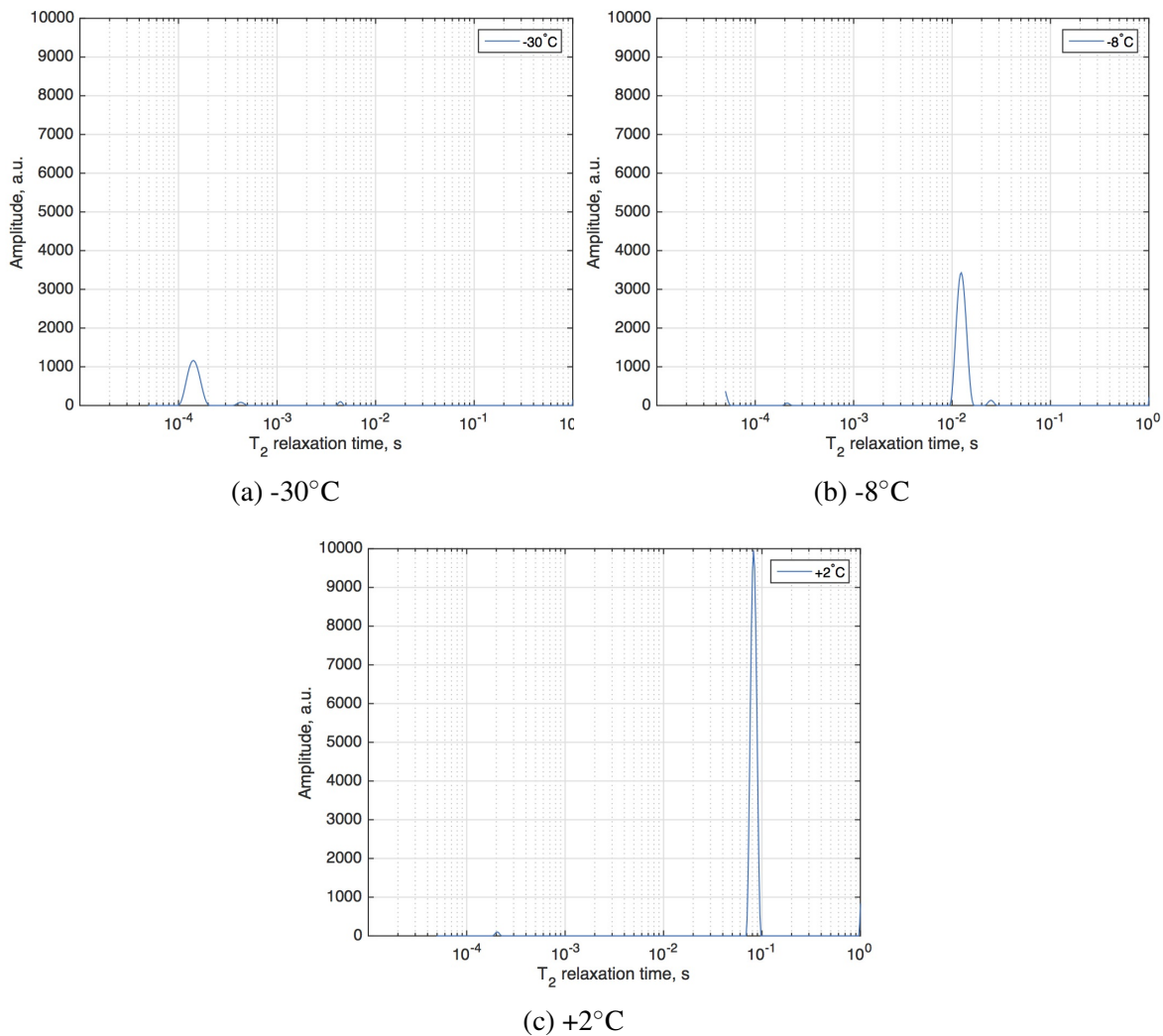


Fig. 5.4 A Lin-Log plot of the ILT data for three different temperatures (a) -30°C, (b) -8°C and (c) +2°C for the SiO₂ with 8.7 nm pores, as stated by the producer, saturated with water.

The full process of water thawing in the SiO_2 with 8.7 nm pores as viewed by the NMR cryoporometry is shown at Fig.5.5. The signal associated with the non-freezing monolayer of water is detected through the temperature range from -70°C up to the -10°C . With the temperature increase the T_2 relaxation time shifts to the higher values as well as the intensity increases. The T_2 time changes by nearly 2 orders of magnitude from -70°C to -10°C .

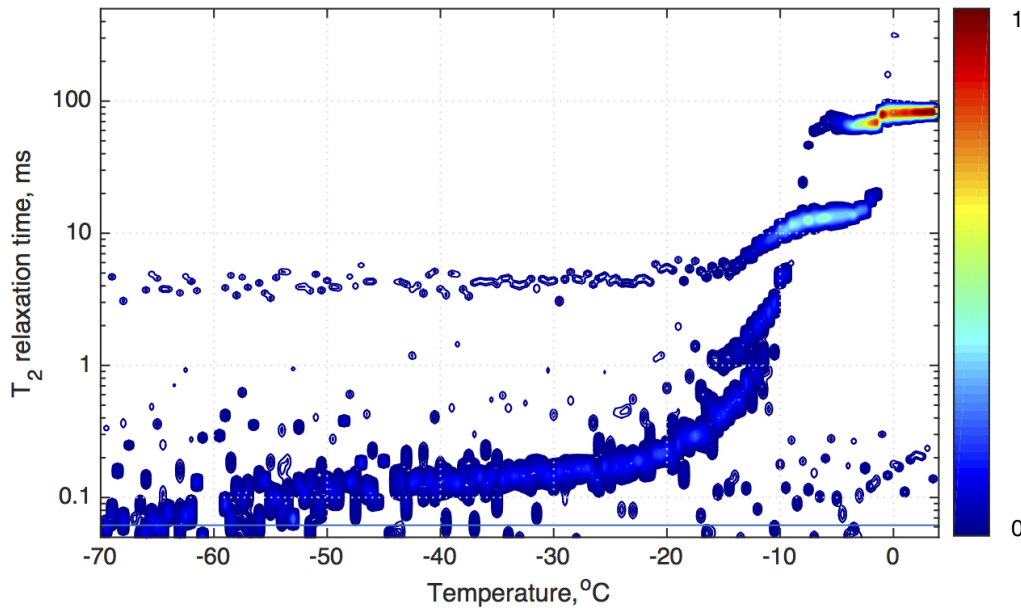


Fig. 5.5 A log 3D plot of the ILT for thawing NMR cryoporometry for the SiO_2 with 8.7 nm pores, as stated by the producer, saturated with water.

Water in the pores is seen as a peak with T_2 of around 12 ms in the temperature range from -12°C to -2°C . After water thawed in the pores, the monolayer water signal is not detected, due to the rapid exchange with the pore core water, thus two of these signals are averaged and seen as one single peak.

A peak with the T_2 around 100 ms appears in the temperatures from -5°C to 5°C . It is attributed to the bulk water signal. It has a high intensity and long T_2 as expected, especially above 5°C .

It is surprising that a separate pore water peak is not seen when the bulk water is not frozen. One reason, as suggested by Mitchell et al. (2005), is that the pore water is exchanging with the bulk water outside the particle grains on the T_2 time-scale so that an average rate it seen. This might also explain why the bulk T_2 is significantly less than the few seconds normally expected for bulk water. It would also explain the step in the relaxation time of the bulk water at 0°C . It may be that the water in the interstitial space melts before the bulk water above the sample. When the bulk water is frozen, the pore water cannot exchange with

it and its true T_2 value is seen. There is also possibility that the top and the bottom of the sample are at slightly different temperatures. Also the melting in different environments may be time dependent as suggested by Petrov and Furó (2011). This may further account for some of the "step" detail around the transition temperatures.

5.1.3 Results: 11 nm porous glass

The same experiment was performed on the SiO_2 with 11 nm pores. In this case, the results are very much as expected with similar explanation to the 8.7 nm material. Thawing of water in 8.7 nm pores occurs at lower temperature, compared to 11 nm SiO_2 . Thus, for the single exponential fit, the temperatures were chosen as: -25°C , -10°C , $+5^\circ\text{C}$.

A linear-log plot Figure 5.6a shows that at $+5^\circ\text{C}$ the decay is mono-exponential with a long relaxation time of around 60 ms. A single exponential fit gives a value of 53.8 ms, Table 5.4. This value is a bit shorter than for the SiO_2 with 8.7 nm pores, perhaps because the volume ratio of bulk water to water in pores that weights the relaxation average is different.

At -10°C we expect only water in the pores to remain unfrozen. Figure 5.6b shows that first echo of the CPMG data is less intense and has a short T_2 of circa 2 ms. A single exponential fit gives T_2 value of 2.2 ms and 12% in normalized intensity, Table 5.4.

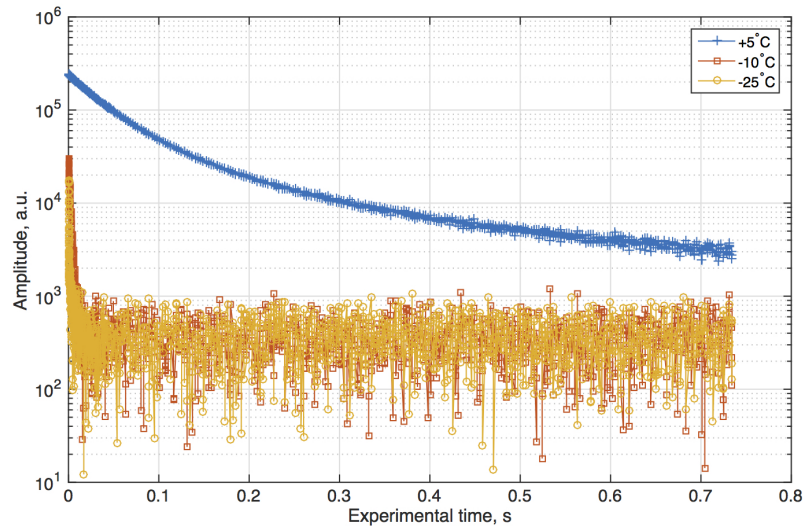
At -25°C there is still a small intensity, just like in the case of the SiO_2 with 8.7 nm pores. According to a single exponential fitting it has a T_2 of 0.394 ms and a normalised amplitude of 7%, Table 5.4.

Temperature	Single exponential fit value	Magnitude (Norm, %)
$+5^\circ\text{C}$	53.8 ms	100
-10°C	2.2 ms	12
-25°C	0.394 ms	7

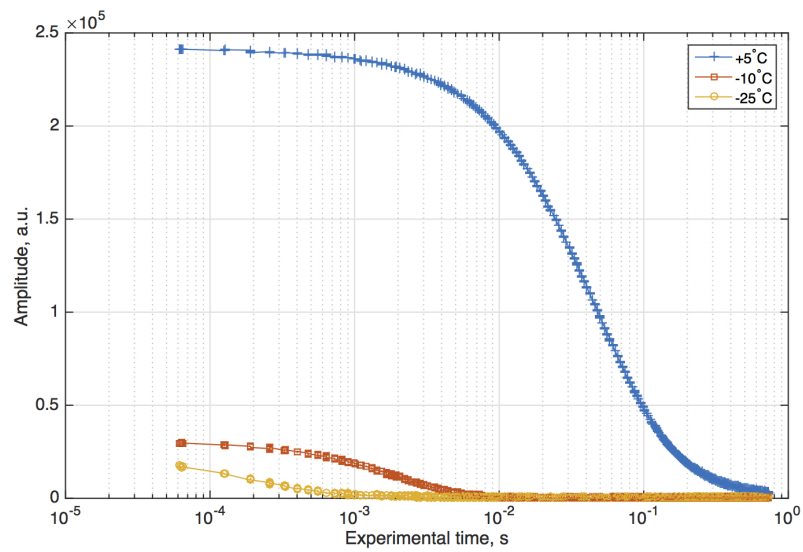
Table 5.4 Parameters for the single exponential fit of the SiO_2 powder (11 nm pores) saturated with water for three temperatures.

For a better understanding of the data visualisation Fig 5.7 shows same data as in Fig. 5.8 but at different angle. This view doesn't give extra information, but helps to better understand figures in the thesis.

The full ILT dataset for the temperature range from -45°C to 5°C shows more details of the thawing process, Figure 5.8. From -45°C to -20°C there is low intensity of a short T_2 signal of circa 0.2 ms. Single temperature point ILT for the -25°C dataset at Fig. 5.9a shows three peaks, one dominant at about 0.2 ms and two smaller peaks. The smaller peaks



(a) Lin-Log plot.



(b) Log-Lin plot.

Fig. 5.6 (a) Lin-Log and (b) Log-Lin plot of the CPMG traces for three different temperatures for the SiO_2 (11 nm pores) powder saturated with water.

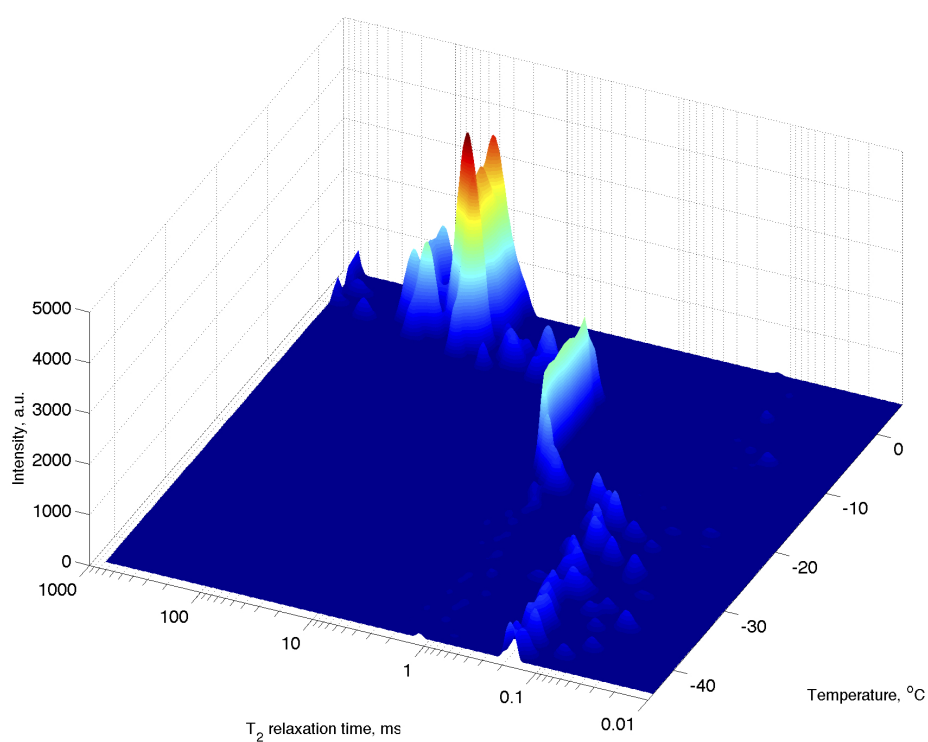


Fig. 5.7 A log 3D plot of the ILT of NMR cryoporometry for the SiO₂ with 11 nm pores, saturated with water. Data same as Fig. 5.8 but at different angle.

combined represent only 13% of the total intensity. Thawing of water in the pores starts at around -17°C . Thawed water becomes detectable and T_2 shifts towards longer values, as well as the amplitude of the peak increases. Figure 5.4b of the ILT data for -10°C shows one peak at around 2 ms. Thawing in pores is finished at around -15°C . Until the bulk water starts to thaw at around -4°C , the peak corresponding to the water in the pores remains constant. Neither T_2 nor the peak magnitude changes with the temperature increase from -15°C to -5°C . At 5°C all water is thawed and we detect a high intensity, long T_2 peak around 50-100 ms. A closer look at the 5°C data, Fig. 5.9c reveals three, maybe four peaks. This will be discussed in detail, with the next material, MCM-41.

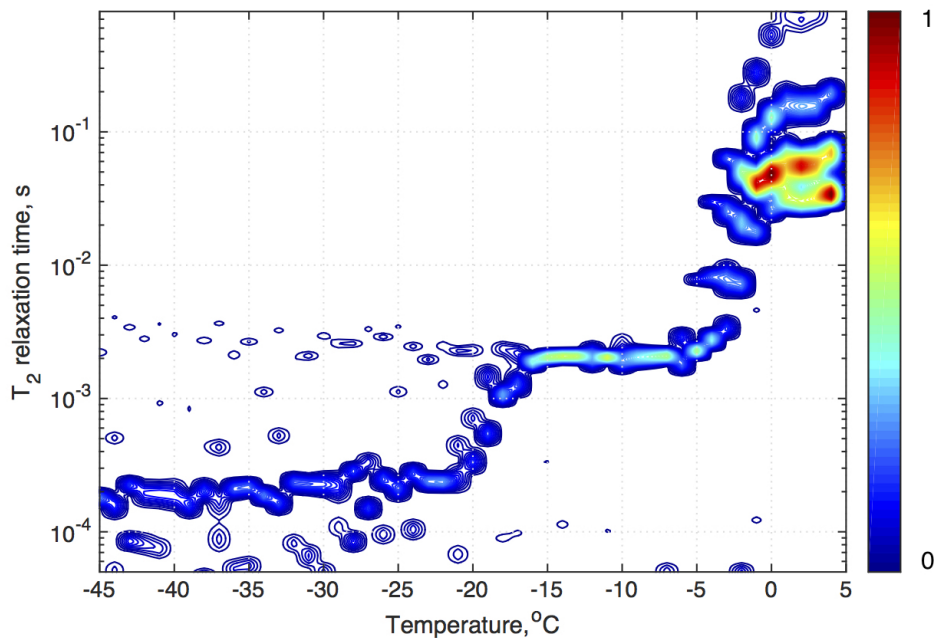


Fig. 5.8 A log 3D plot of the ILT of NMR cryoprometry for the SiO_2 with 11 nm pores, as stated by the producer, saturated with water.

5.1.4 Results: 3 nm MCM41

Fig.5.10a shows three CPMG traces for three representative temperatures recorded in order: -50°C , -20°C and $+9^{\circ}\text{C}$, but discussed in reverse order as previously. At the highest temperature 9°C the liquid is not frozen and the data can be approximately fit to a single exponent with the value of 23.4 ms, Table 5.5. The decay is dominated by the signal from the bulk water. However, the fact that it is not a true single component decay is interesting and discussed further below.

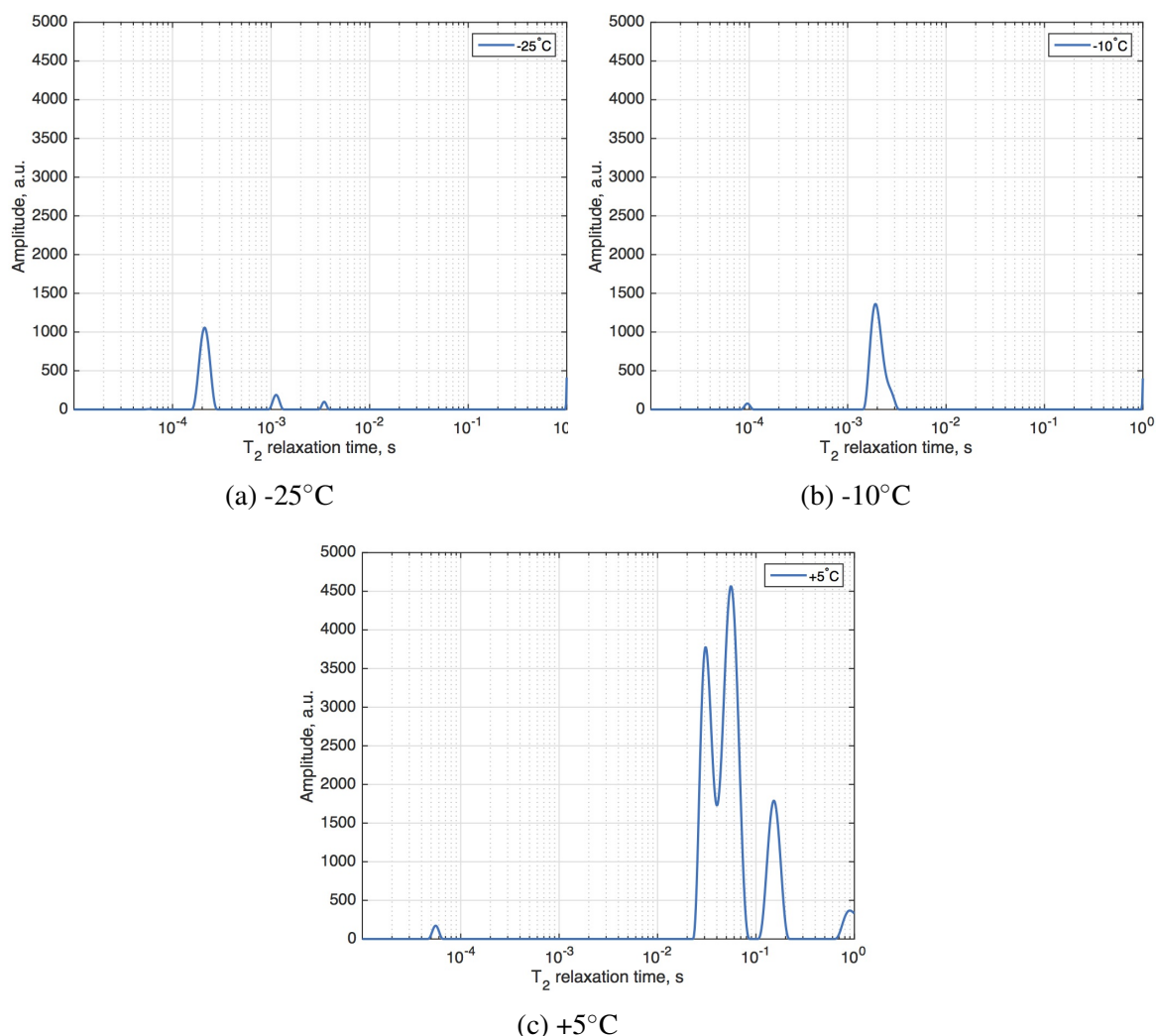
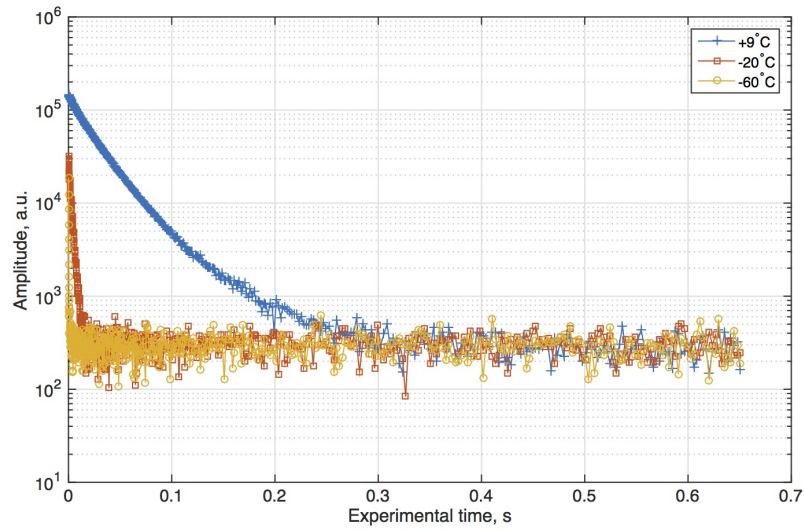


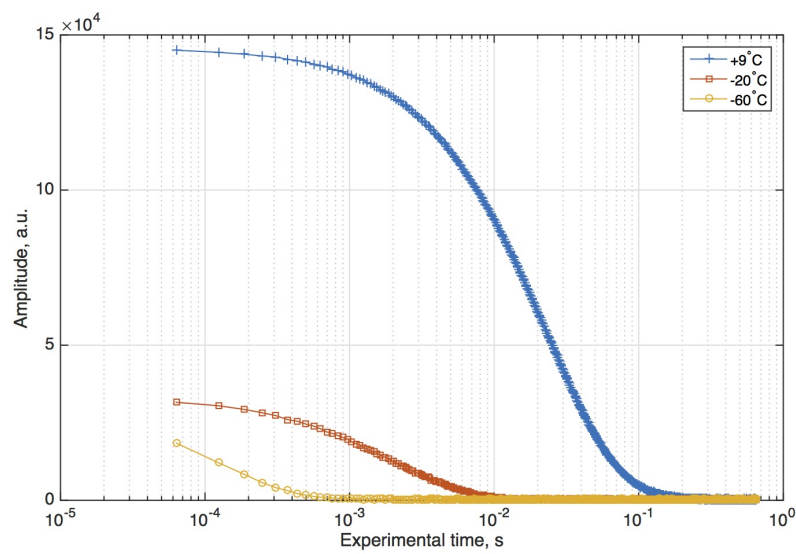
Fig. 5.9 A Lin-Log plot of the ILT for three different temperatures (a) -25°C, (b) -10°C and (c) +5°C for the SiO₂ (11 nm pores) powder saturated with water.

At -20°C, the first echo is approximately 20 % the intensity of the first echo at +9°C. This is because the bulk water has frozen and has a relaxation time of a few microseconds, too short to be seen by CPMG. However, the water in the pores of the MCM-41 powder remains unfrozen. A single exponential decay fitting gives a relaxation time of 2.3 ms and normalized intensity of 22% as given in Table 5.5.

At -50°C there is still some CPMG signal left, just like in the previous materials. It may be a single layer of unfrozen water. Alternatively this may be hydrogen associated with silanol groups at the pore surface. According to a single exponential fitting it has a T_2 of 0.2 ms and a normalised amplitude of 13%, Table 5.5.



(a) Lin-Log plot.



(b) Log-Lin plot.

Fig. 5.10 (a) Lin-Log and (b) Log-Lin plot of the CPMG traces for three different temperatures for the MCM-41 materials saturated with water.

Temperature	Single exponential fit value	Magnitude (Norm, %)
+9°C	23.4 ms	100
-20°C	2.3 ms	22
-50°C	0.2 ms	13

Table 5.5 Parameters for the single exponential fit of the MCM-41 powder saturated with water for three temperatures.

More insight is gained from an inverse Laplace transformation analysis that is essentially a fit to a continuous distribution of T_2 relaxation times. The relaxation distribution for the sample at +9°C is given in Figure 5.11a. It has 3 main peaks. Let's discuss peaks from left to right.

The first peak has a relative integrated area of 8% and a T_2 of 0.45 ms. It is attributed to water in the MCM-41 nano pores. The next largest peak has an amplitude of 67 % and a T_2 of 2.1 ms. It is attributed to water in the interstitial spaces between the MCM-41 powder particles. The third peak has a T_2 of 4.1 ms and an amplitude of 24%. It is attributed to the small amount of bulk water above the powder sample. The water in the nano-pores has a greatly reduced T_2 compared to the bulk water due to interaction with the pore surfaces and surface relaxation. The water between the particles has a slightly reduced T_2 compared to the bulk water. The reason is twofold. First there is interaction with the powder particles outer (macroscopic) surface. This effect is accentuated because the particles tend to agglomerate in the water leaving "macro" pores. The other reason is exchange of water between the pores and interstitial spaces that will average the relaxation rate between that of true bulk water and that in pores – as has been suggested by Mitchell et al. (2005).

Figure 5.11b shows the ILT distribution of relaxation times for the sample at -20°C. At -20°C the ILT shows two peaks. One interpretation is that the peak at $T_2 = 2.8$ ms is due to liquid water in the nano pores whereas the peak at 0.7 ms is due to hydrogen in silanol groups associated with the pore surfaces. The peaks have intensities of 73.5% and 26.5% respectively. An approximate calculation can be carried out to see if this interpretation is sensible. The MCM-41 pores are long cylinders of radius $R=3/2$ nm. If 73.5% of the water is in the bulk of the pore, then according to Figure 5.11, the expected thickness of the surface layer is 0.2 nm. This is of the same approximate size as an Si–OH bond length: 0.165 nm.

Figure 5.11c shows the distribution at -50°C. Now the water in the pores is frozen and so not seen. The hydrogen associated with the surface remains sufficiently mobile to see. However, the T_2 value is reduced to the the lack of averaging with the previously unfrozen water contained in the central pore volume.

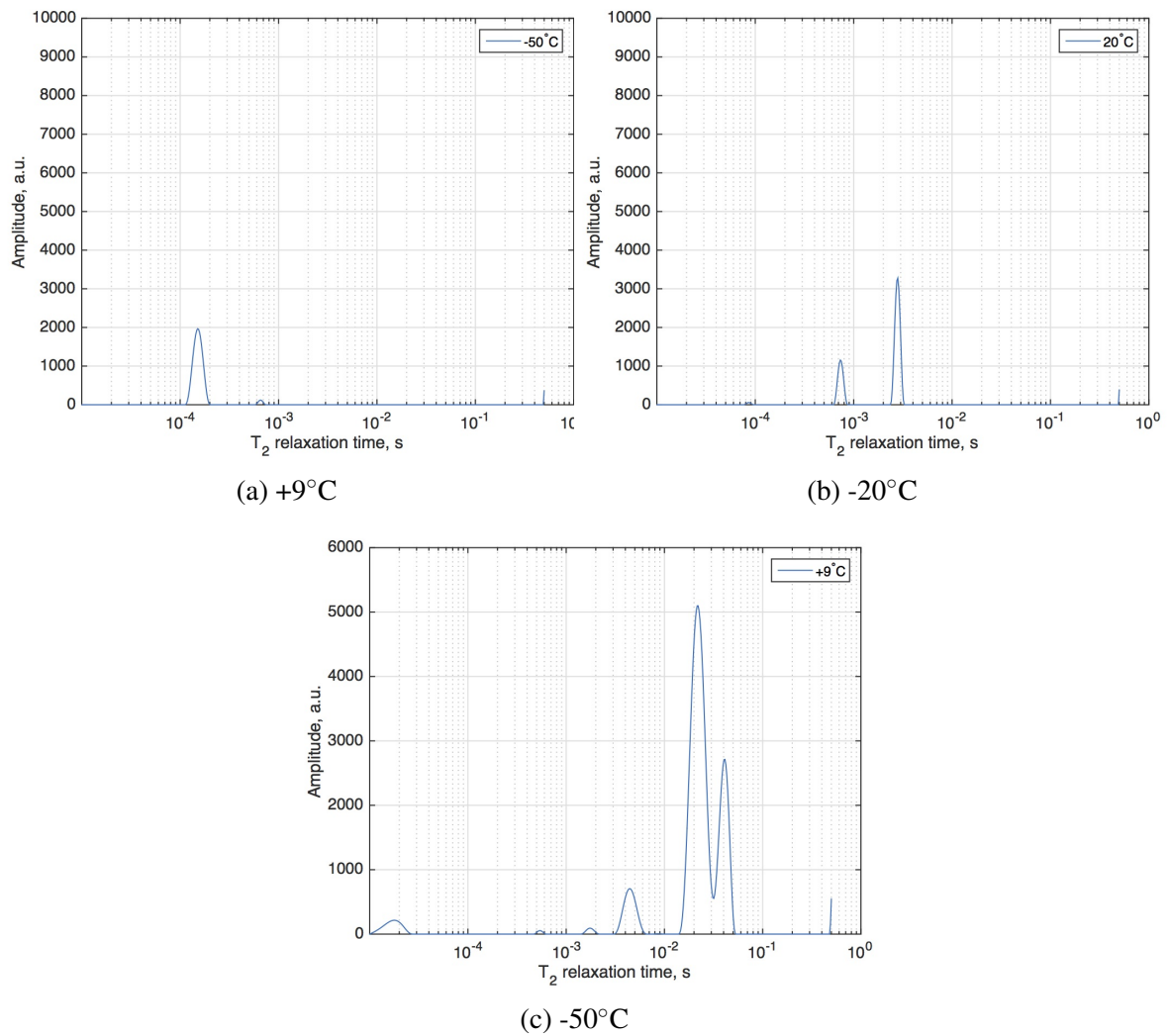


Fig. 5.11 A Lin-Log plot of the CPMG traces for three different temperatures for the MCM-41 materials saturated with water.

Greater insight can be obtained from the full data set as a function of temperature between -60°C and $+15^{\circ}\text{C}$. The data was recorded on a warming cycle. This data has been analysed using the Inverse Laplace Transform and is shown in Figure 5.12. This figure is a colour map of the signal as a function of T_2 and temperature and reveals far more detail.

There are three distinct regions at Fig. 5.12. Below circa -40°C , there is a single, low intensity peak with T_2 about $100\ \mu\text{s}$ that gently increases with temperature. Following the earlier discussion, this peak is assigned to mobile water in a monolayer between frozen pore water and a pore wall. A corresponding peak was not seen by others for cyclohexane (Mitchell et al., 2005), as cyclohexane is non-polar and does not interact with the pore wall. This signal has not been seen by others for water either (Valckenborg et al., 2002). Usually NMR cryoporometry experiments are performed on the sample with larger pores, thus there is no need to start to record CPMG at the very short times. At this particular experiment our first time point for the CPMG is $63\ \mu\text{s}$ which might explain why we were able to record such a short signal not seen by others. For example, Valckenborg et al. (2002) shows that the first echo point for combined NMR relaxometry-cryoporometry experiment was $400\ \mu\text{s}$ only.

From -40°C to 0°C there are two peaks. One has T_2 about $700\ \mu\text{s}$, the other about $3000\ \mu\text{s}$. The one with longer T_2 is about 10 times more intense than the other and we assign this to water thawed in the pores. Above 0°C , there are three peaks with T_2 values of the order of tens of ms. One is clearly bulk water residing above the compacted particles in the tube. The other is water on exterior particle surfaces and between powder grains in exchange with pore water as has been discussed above.

The data shown so far was obtained on the warming cycle. By way of warning, data for the same material is plotted for the cooling cycle. Supercooling is a known phenomenon that leads to the delayed freezing. As can be seen on a Fig. 5.13 bulk water freezes only at about -12°C due to the supercooling. This value is in agreement with other experiments studying supercooling phenomenon. Ignoring the temperature shift, the freezing data looks like a mirror reflection of the warming data. This proves that different peaks that have been captured on warming are not any kind of artefact. The same number of peaks with the same behaviour and similar intensities are detected on the cooling, as well as on the warming.

5.1.5 Discussion

Petrov and Furó (2011) calculated temperatures of thawing in spherical pores. What follows is a comparison of the experimental three points data presented to the Petrov theoretical analysis. Petrov finds that the melting temperature T_m and freezing temperature T_f are related to pore radius, r , by:

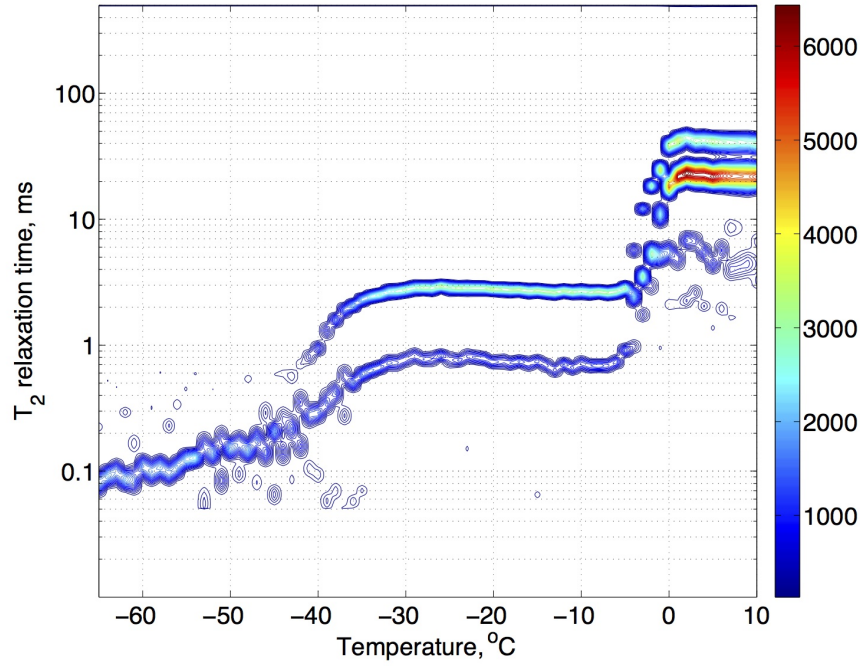


Fig. 5.12 A log 3D plot of the ILT for thawing NMR cryoprometry for the MCM-41 materials saturated with water.

$$F(z, T) = (\Delta H/v)(T/T^0 - 1)V_s(z) + \gamma_{sl}S_s(z) + \Delta\gamma g S e^{-z/\xi} \quad (5.1)$$

where T^0 , ΔH and v are bulk melting point, enthalpy of melting and molar volume of the probe fluid; V_s and S_s volume and the surface area of the solid core; S the surface area of the pore wall; γ_{sl} the solid–liquid surface tension (approximated to that for the planar interface); $\Delta\gamma$ the excess surface tension on the solid-wall interface over that on the solid–liquid-wall interface; and ξ the correlation length of the crystalline order at the solid–liquid interface; z is a thickness of pre-molten layer.

Figure 5.14 shows a plot of Petrov’s pore size against melting point depression evaluated using equation 5.1 as reported in Petrov and Furó (2011). Two lines are calculations made for spherical (upper line) and cylindrical (bottom line) pores. The Figure also shows the three experimental points for the three model materials.

Generally, it can be said that the results are very close to the theoretical values especially for the smaller pores. With larger, 11 nm and 8.7 nm pores the results are a bit off set. However, we don’t know exactly what type of pore the studied silica glasses have, thus it is difficult to judge on differences between our results and theoretical calculations.

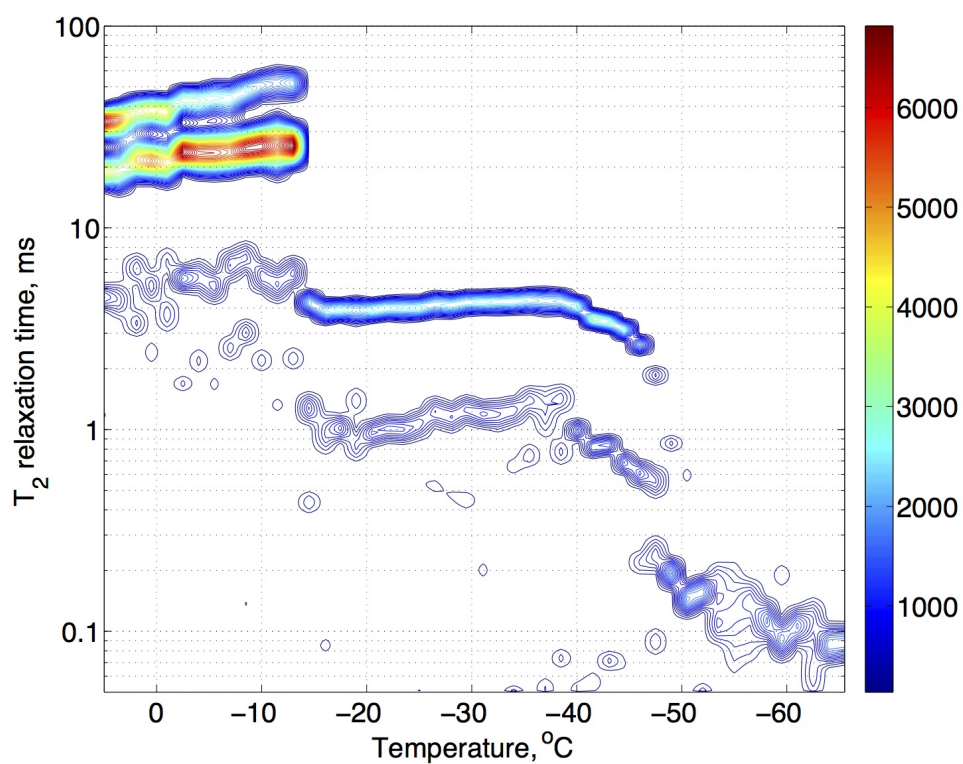


Fig. 5.13 A log 3D plot of the ILT for thawing NMR cryoporometry for the MCM-41 materials saturated with water.

Thawing in the pores starts from the non-freezing water layer of water, that propagates toward the solid with the temperature increase. Three tested materials were obtained from different producers, have different particle size and most likely different pore structures. All of these factors can affect water thawing behaviour in the pores. Latter it affects calculation of the pore size based on the melting temperature.

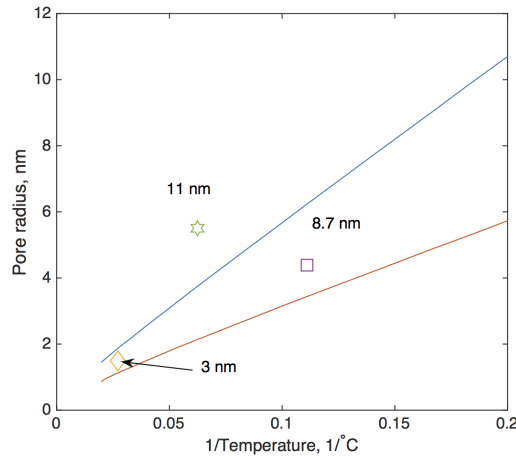


Fig. 5.14 Comparison of the theoretical predictions calculated by Petrov and Furó (2011) (upper line — for the spherical pores, bottom line – cylinder pores) and experimental data. ΔT was used to calculate x axis.

But looking at the Fig. 5.14 it can be said that results from three silica glasses are generally in agreement with theoretical predictions.

In conclusion, experiments on glasses, showed ability to detect the signal originating from unfrozen water in pores and from non-freezing mono-layer of water. Thus we conclude that this technique is suitable for the investigation of the cementitious materials. Application of the temperature varied relaxometry for the cementitious materials is presented in the next section.

5.2 Relaxometry-cryoporometry on the cementitious materials

The next step for our experiments is to apply developed technique to cement paste. However, preliminary experiments tests showed some difficulties. Paramagnetic ions present in cement paste drive relaxation times to shorter values. Theoretically there is a linear relation between relaxation rate and time and paramagnetic ion concentration. What is worse, the relaxation time decreases, as the temperature goes down. With cement paste we experienced the problem

that already at -30°C part of the shortest T_2 component was below the spectrometer detection limit, i.e. too short, below 0.1 ms. Thus at low temperatures we lose valuable information of the shortest T_2 .

Another possibility is to measure C_2S and C_3S pastes. Tricalcium silicate (also called alite, Ca_3SiO_5 or C_3S in abbreviation) and β -dicalcium silicate (C_2S , Ca_2SiO_4 or belite) are the major components in Portland cement clinker. Both C_2S and C_3S were synthesized at LafargeHolcim Research Centre by heating up pure calcium carbonate and silica. The resultant product has no paramagnetic iron or manganese in it.

5.2.1 Materials and methods

The following procedure was applied to prepare C_2S ² and C_3S pastes:

- at a temperature of 20°C , add powder of C_2S or C_3S to a required quantity of deionized carbonated water in less than 30 seconds, while stirring with a spoon;
- mix for 1 minute at a speed of 3000 rpm (revolutions per minute);
- pour the mixture into the cleaned cylinder molds ($d=11\text{mm}$, $h=70\text{mm}$) and vibrate molds on a vibrating table for 10 seconds to remove the trapped air bubbles
- seal the molds and rotate the sealed mold in order to prevent any segregation. The rotation lasted for 15 hours for C_3S and C_2S pastes before set

After rotation, the C_2S samples were demolded and cured in deionized de- CO_2 water at 20°C till given age. C_3S pastes were left in the plastic cylinder with couple of drops of water added on the top to insure the sample was fully saturated.

One C_2S sample of 1.5 years old was tested. C_3S samples were from two to eleven days old. Only data for the 11-days old C_3S data is presented. We learned from the experiment that C_3S paste reacts quickly and basically there are no differences in data obtained on 2 days or 11 days.

Data was obtained in the same manner as in the case of silica glasses. After hydration, first, the samples were crushed in order to get them in NMR tubes. However, unlike silica glasses no additional bulk water was added. The paste was quenched in liquid nitrogen. Then it was inserted into the NMR spectrometer that was pre-cooled to -60°C . It was given time to equilibrate to the temperature. A CPMG echo data train was recorded. After that the

²The C_2S sample was prepared by Qing Zhang, details of the materials are taken from *Qing Zhang. Creep properties of cementitious materials : effect of water and microstructure: An approach by microindentation. Universit e Paris-Est, France, 2014*

temperature was increased in a step-like manner with 2°C step for C₂S. The temperature was stabilised for 2 minutes and an echo train recorded each step. Due to the low signal to noise ratio of the data for later C₃S experiments, 5 CPMG echo trains were recorded each step for C₃S. Also, for C₃S, the step size was 1°C. Between each CPMG echo train the NMR frequency was reset. This was done to eliminate the problem of changing frequency offset as the magnet (as opposed to sample chamber) temperature slowly changed. For each step, the 5 CPMG trains were averaged into one and processed with ILT.

5.2.2 Results for C₂S

Fig. 5.15 shows the ILT distribution of relaxation times for C₂S at 3 different temperatures: -70°C, -20°C and +20°C after 1.5 years hydration. Fig. 5.16 shows the ILT processed data for the C₂S at 1.5 years for all temperatures. At -70 °C there are 2 clearly distinguishable peaks. The peak with shorter T_2 has a relaxation time of about 0.07 ms. The other peak has a relaxation time of 0.12 ms. The ratio of the integrated area of the first peak to the second peak area is almost exactly 4. The first peak is much more intense. Both peaks shift towards longer T_2 values with increasing temperature. By -20°C the T_2 of the shortest peak is 0.15 ms. However, the ratio of the areas has changed much more. The ratio of the first peak to the second peak areas is now 0.7: the second peak is much more intense. Above the room temperature three peaks were seen. These peaks were reminiscent of peaks seen for regular white cement by Muller et al. (2012) and will be discussed later. It should be noted from figure 5.16 that it is quite hard to estimate the peak intensity from the peak height as represented by the coloured contour map because the ILT peak width is very noise dependent. However, the area is not anywhere near as noise dependent (Muller, 2014). For this reason the two peak areas are plotted in figure 5.17 and the total sum of the peak areas is plotted in Figure 5.18. These plotted areas have been Boltzmann factor corrected. The border areas of the peaks were defined by drawing straight lines through the data as shown in Figure 5.16.

Figure 5.17 shows that below -10°C the total of the 2 peaks decreases with the decreasing temperature. This is because some water is freezing and is lost from the signal. However, there is no obvious, single freezing event for this water down to -80°C. It is a smooth gradual change. The intensity of the longer T_2 peak that is labelled "gel" water, also decreases with the decreasing temperature but at a faster rate. On the other hand, the intensity of the shortest T_2 peak increases slightly with decreasing temperature. The shortest peak is attributed to water in interlayer spaces of the C₂S gel. From earlier studies and analogue materials such as tobermorite the interlayer is expected to be just two or three monolayers thick (Richardson, 2004). The longer T_2 peak is attributed to water in gel pores. Since there is expected to be a distribution of gel pore sizes, this water freezes over a range of temperatures and accounts

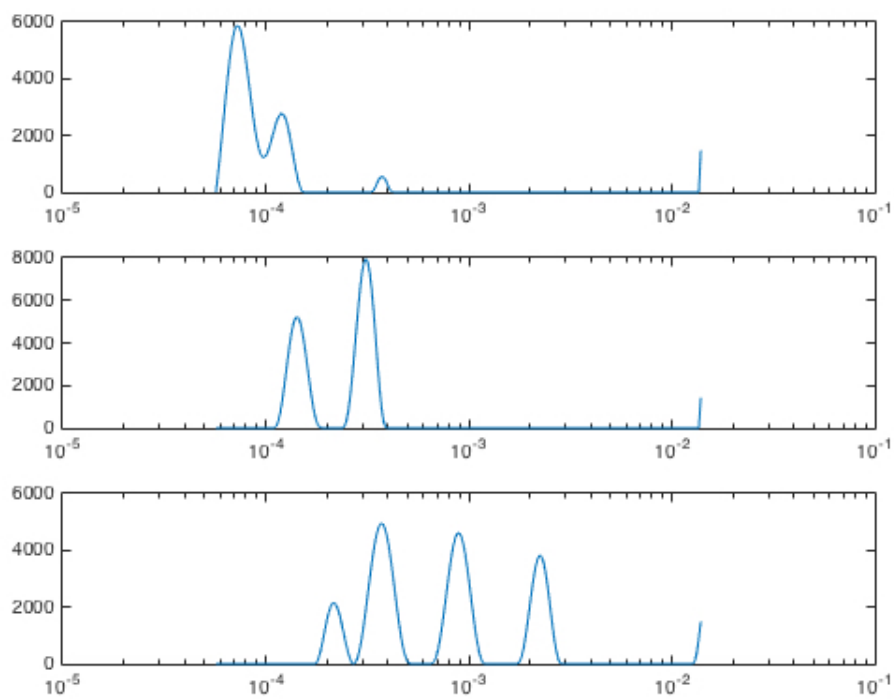


Fig. 5.15 3 ILT data for C_2S at three temperatures from top to bottom: $-70^\circ C$, $-20^\circ C$, $+20^\circ C$.

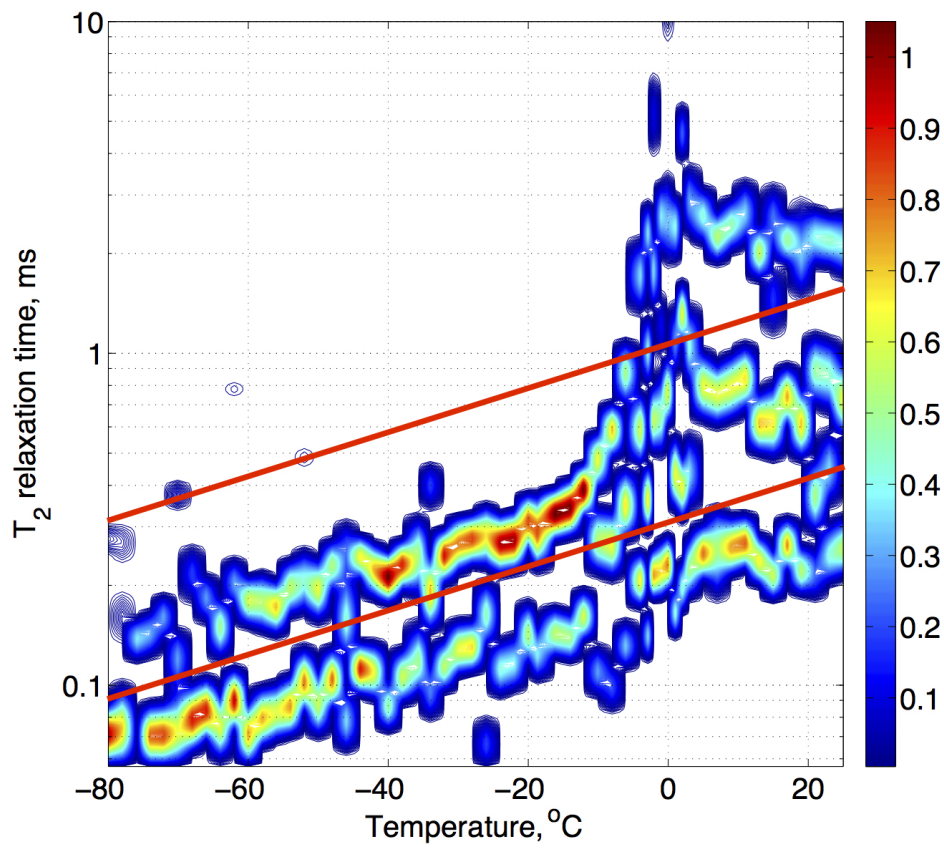


Fig. 5.16 A log 3D plot of the ILT for thawing NMR cryoporometry for the synthetic C_2S . Red lines indicate pore populations signal separation.

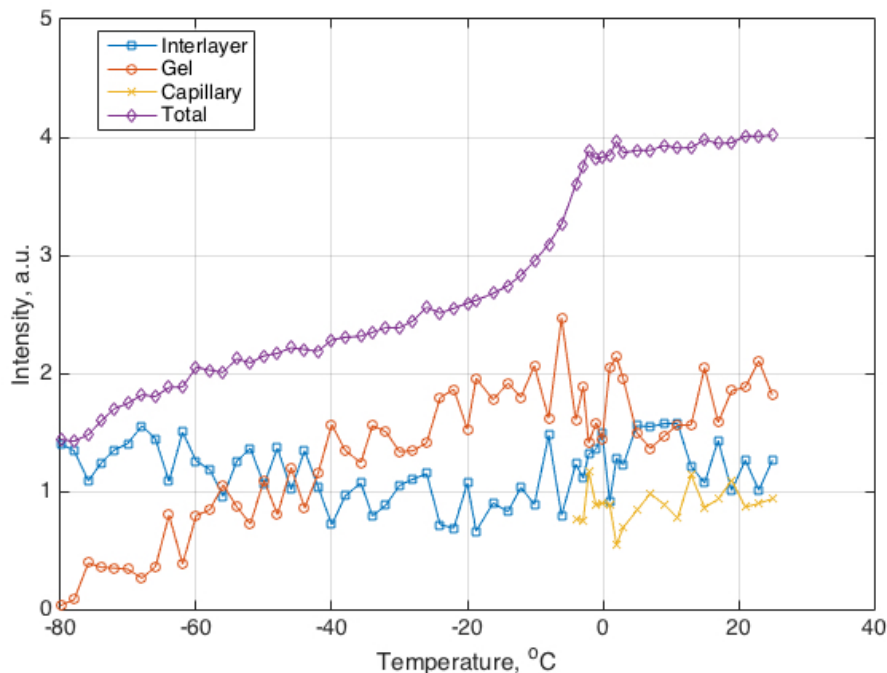


Fig. 5.17 Intensities for three different pore populations of the 1.5-years old C_2S paste as shown on Fig. 5.16.

for the gradual transition. However, as it freezes, it leaves behind an unfrozen surface layer that, from an NMR viewpoint, looks like interlayer water. This is why the interlayer water signal increases. At the lowest measured temperatures it is reasonable to assume that only unfrozen gel water is in gel pore surface layers or interlayers. In this case comparing the interlayer signal at -70°C and -10°C suggests that the volume of gel pore surface water must be about $\frac{1.4-0.8}{0.8}$ or 75 % of the interlayer volume. With reference to Fig 5.17, if it is assumed that there are two monolayers of water between each solid backbone in C_2S and the unfrozen surface is just one monolayer thick, then there must be $n=8/6$ or approximately 1.3 layers stacked in local C-S-H assemblages. Alternatively, if it is assumed that the unfrozen layer is 2 monolayers thick, then there are $n=16/6$ or about 2.6 layers in a C-S-H stack. These numbers are entirely consistent with those derived from surface relaxation analysis by Muller et al. (2012). These authors found 3 layers in white cement.

If it is argued that the gel pores are planar and that the surface layer of water is a monolayer on either side, then the ratio of total water of the gel pores to that on the surface is about $2/0.6$ so that the gel pore is $m = 2 * 2/0.6 = 6.6$ monolayers water thick. This suggests a gel pore thickness of about $7 * 0.29$ nm or about 2-3 nm. On the other hand, if the unfrozen surface layer is about 2 monolayers thick each side, then the gel pore is about $14 * 0.29$ or

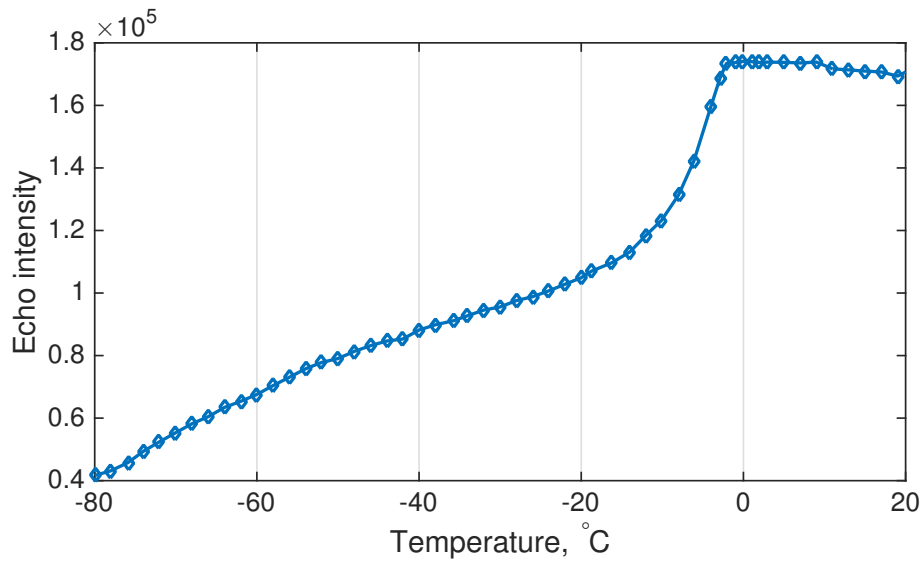


Fig. 5.18 C₂S first echo CPMG intensity plot.

4-6 nm thick. These sizes are also consistent with Muller et al. (2012) results from the other relaxometry method.

An alternate estimate can be made of the gel pore size distribution. This is done using the Gibbs-Thomson equation. In practice, the data in Fig.5.17 gel peak area is smoothed by 3-points averaging. The area beneath the curve and the curve gradient are calculated. The melting point depression is assumed to be the same as the measured value for silica glasses: 120. On this basis, Fig. 5.19 shows the calculated pore size distribution of the gel pores. Muller et al. (2012) gives a value of 0.85 nm for C–S–H interlayer spacing, 2.5 nm for gel pores, and 8.0 nm for interhydrate pores. These authors estimated the pore size based on the surface relaxivity. Compared to Muller et al. (2012), the cryoporometry method does not require the surface relaxivity to be known, but does require the melting point depression to be known. However, this is probably well estimated from the silica glass results. It is possible to say that our results are in line with Muller et al. (2012) work, since we detect most of the gel pores to be less than 2 nm. However, our data has been recorded with 2°C temperature step. For better pore size estimate it would be needed to record data with at least 0.5°C step.

The temperature dependence of the T_2 must also be considered. It is surprising that the interlayer value changes with the temperature. One possibility is that the water in the gel pore and interlayer peaks is exchanging as discussed in the next chapter. This would tend to average the relaxation times. As more gel pore water in larger pores freezes, so the average T_2 of the gel water decreases and hence so the exchange rate averaged value of the gel and interlayer T_2 also decreases.

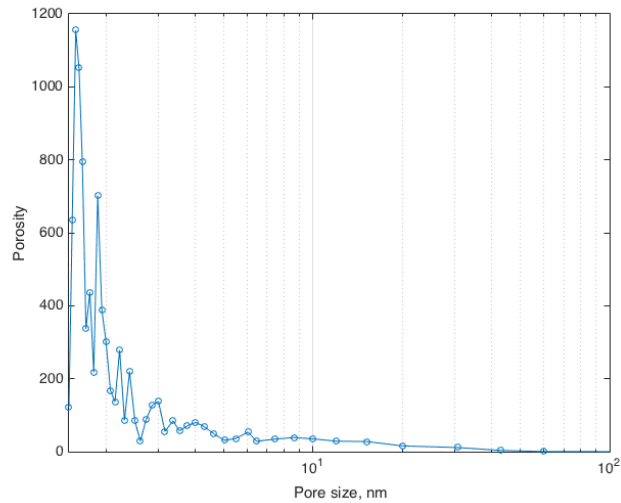


Fig. 5.19 Pore size distribution of the C_2S obtained by cryoporometry.

At 20°C we detect three peaks at the ambient temperature as shown in Fig. 5.16. The first two peaks with the lowest T_2 values are attributed to interlayer and gel pore water as before. The third peak, with longest T_2 is attributed to capillary pore water. Figure 5.17 suggests that the capillary volume is 23 % of the total water volume. Once all the water thawed, there is very little temperature dependence of the T_2 values. The T_2 values are about 2 to 3 times longer than the T_2 values measured by Muller et al. (2012) for white cement paste. This is almost certainly because pure C_2S is free from paramagnetic impurities while there are residual impurities in the white cement. Also, the pore sizes may be slightly different.

There are likely differences in materials, which may yet explain some of the more subtle differences in the results between C_2S and SiO_2 presented here, such as the fact that in one case the T_2 is strongly temperature dependent, in the other it is not and that in one case we see one peak per pore type, in the other two peaks. The most likely difference is the nature of the pore surface. The surface of C–S–H is poorly understood but involves hydrated calcium ions not present in SiO_2 glasses.

5.2.3 Results for C_3S

Figure 5.20 shows ILT for the 11 days old C_3S data at three temperatures -60°C , -25°C and $+10^\circ\text{C}$. At -60°C two peaks are distinguishable with T_2 of around 0.07 ms and 0.17 ms. At -25°C there are two peaks again, with a T_2 of around 0.2 ms and 0.4 ms. At $+10^\circ\text{C}$ there are three main peaks and two smaller peaks with T_2 's of circa 0.2 ms, 0.5 ms, 1.5 ms and 5 ms. The three main peaks have intensities of around 44%, 12% and 35%. This is different from

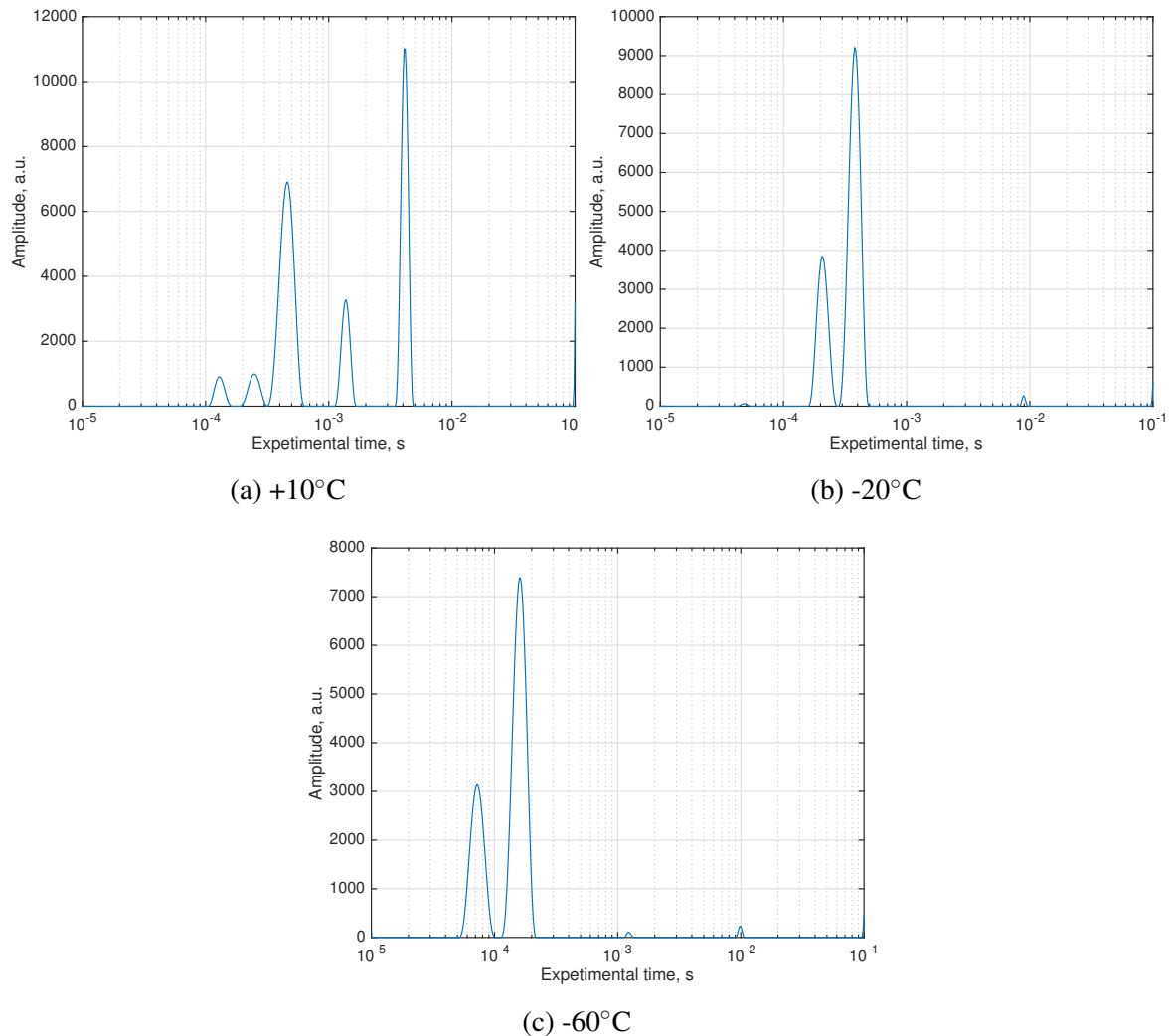


Fig. 5.20 Three different temperatures ILT of the C_3S 11 days old.

the white cement relaxation times detected at ambient temperatures. One possibility is that the three main peaks, in order of increasing T_2 correspond to interlayer, gel and capillary water respectively. The two smaller peaks both occur with lower T_2 values than any of these. The first has a T_2 of about $130 \mu s$ and the other $250 \mu s$. The intensities are around 1000 for both peaks. One or both of these peaks, as will be seen later, are frequently observed, but not always observed. For instance one of them is seen in a regular CPMG analysis of hydrating C_3S as a function of time Fig 5.21. The other occurs just outside the region of inspected T_2 's and may or may not be an artefact. These artefacts are seen at different temperatures in hydrated material but with unreliable T_2 . They are not seen in $T_2 - T_2$ experiments described in the next chapter. There is little obvious explanation for these peaks and hence they are considered artefacts.

One of the explanations is that the structure of C_3S is different from C_2S . Previous works have shown that C_3S microstructure is more compacted compare to C_2S . This could potentially result in different NMR signals. In case of C_3S it means that there are more interlayer pores and less gel pores. Thus the gel pores signal is not dominant. Also the volume of the larger pores is not-comparable to white cement either, as it is around 35% of total water as w/c ratio of the paste is 0.51. It could be a reasonable value since most of the unused water in the hydration will rest in the longest T_2 signal.

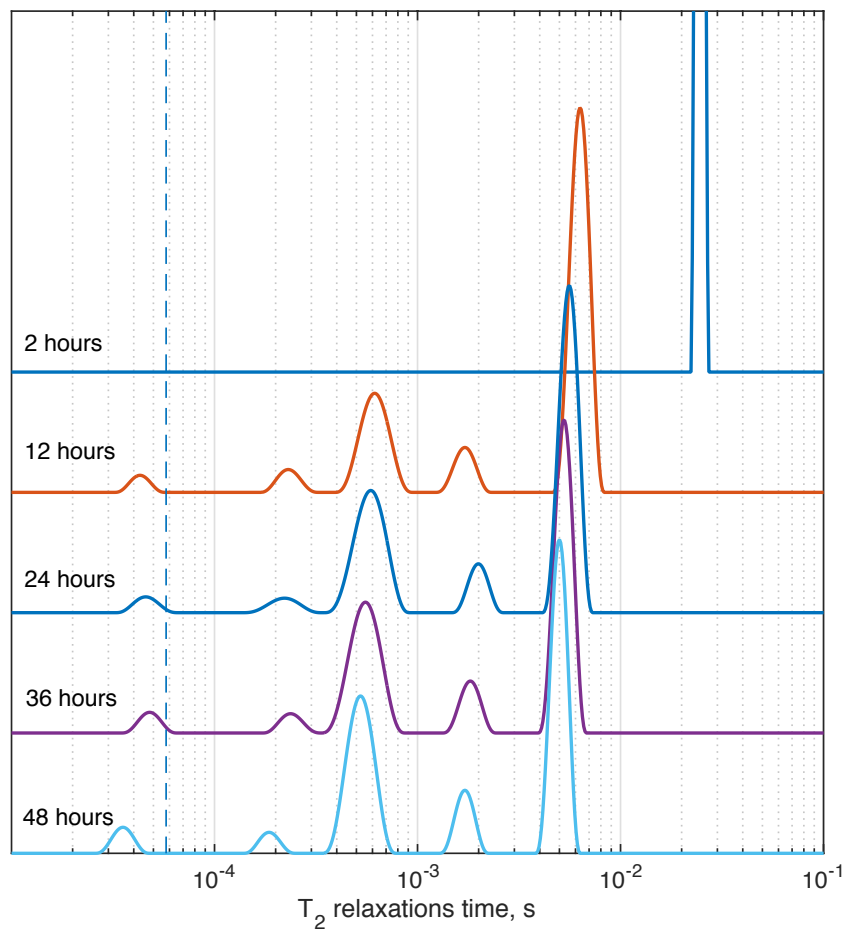


Fig. 5.21 Hydration of C_3S paste as a function of time.

More insight could be gained from the full ILT data set in the temperature range from -80°C to $+10^{\circ}\text{C}$. Fig. 5.22 shows data for the same C_3S paste hydrated for eleven days. At temperatures above 0°C there are three peaks. This is in-line with both C_2S and cement

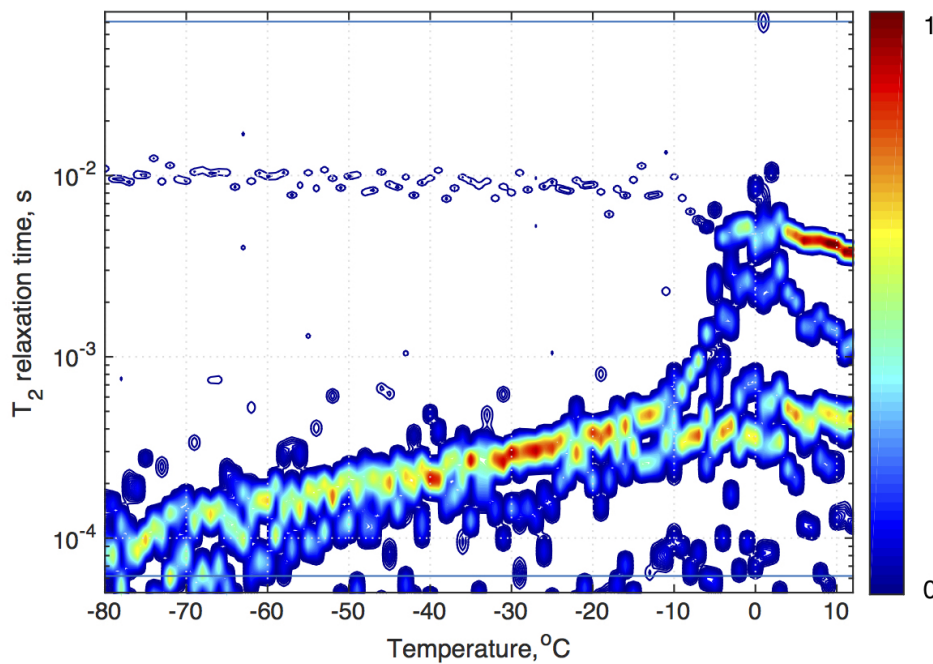


Fig. 5.22 A log 3D plot of the ILT for thawing NMR cryoporometry for the 11 days cured synthetic C_3S .

pastes. In the region between -80°C up to -10°C there is definitely one, probably two peaks. The judgement comes down to visual interpretation of Figure 5.22.

Therefore to infer information about interlayer water and gel bulk and gel pore surface water is difficult. However, the total signal intensity as a function of temperature upon thawing is shown at Fig. 5.23. It is very similar to the one has been shown for C_2S .

It is possible to argue that there are two peaks, just like in case of C_2S but these peaks are too close together to be clearly resolved. Even though we could see two peaks at some given temperatures, as shown in the Fig. 5.20. It may be that the ILT artificiality reduces the width of the T_2 distribution for a range of pore sizes. So called "pearling" of peaks is a problem with ILT algorithm (Callaghan et al., 2003). Therefore, as water in larger pores freezes so the average T_2 of the water remaining in smaller pores reduces and the average T_2 reduces.

It can be said that there is no thawing step between -80°C and -10°C . Peaks gently increase in amplitude and shift towards longer T_2 values. Temperature dependency i.e. T_2 increase with the temperature increase is the same as in the C_2S data. A T_2 value of around 0.1 ms is detected at -80°C with T_2 shifting towards 0.5-0.7 ms at -10°C . Noticeable thawing starts at around -10°C and is very similar to the C_2S thawing at this temperature. There is increase in intensity of about an order of magnitude shift in T_2 within the 10°C degrees.

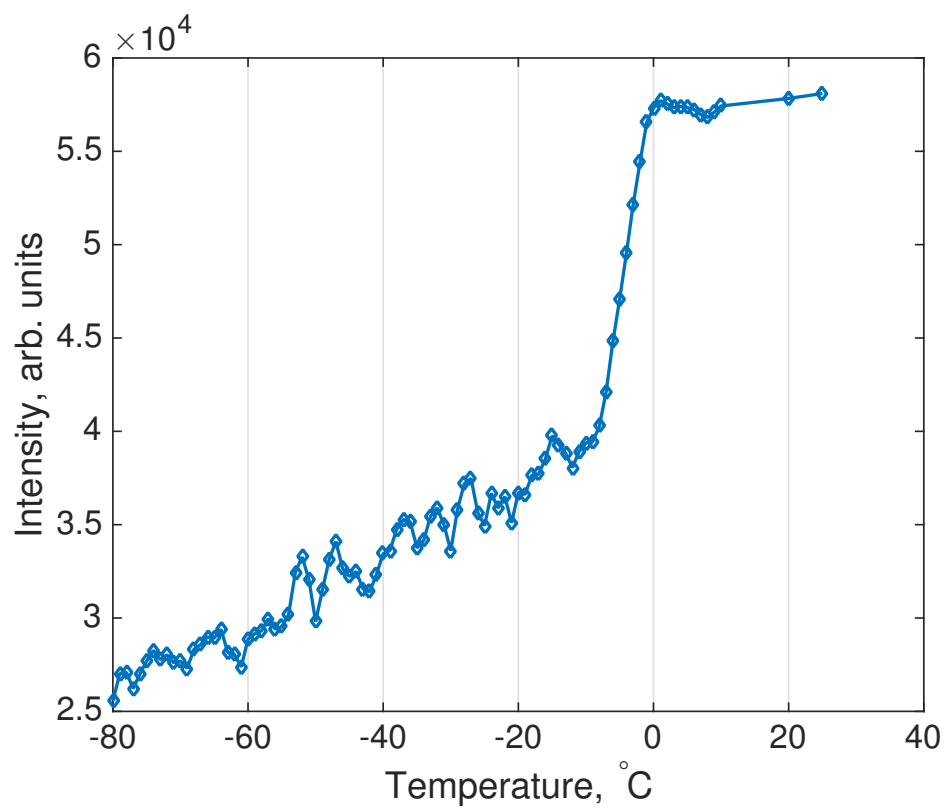


Fig. 5.23 Intensity of the integrated ILT data for the 11 days cured synthetic C_3S .

5.3 Conclusions

In this chapter results of the NMR cryoporometry and NMR relaxometry experiments presented. Water crystal thawing temperatures in the nano pores of both SiO_2 and MCM-41 detected with NMR cryoporometry are generally in agreement with theoretical predictions.

After the technique been validated on model porous silica glass (SiO_2) materials with known pore sizes it was applied to C_2S and C_3S . The ^1H NMR cryoporometry data was used to estimate the pore sizes in C_2S . It was found that the T_2 relaxation time depends on temperature in C_2S and C_3S , but not in porous glasses SiO_2 and MCM-41.

The T_2 temperature shift in cementitious materials is somewhat similar to the behaviour of the shortest T_2 signal of SiO_2 . There are two possible explanations. As mentioned above, it could be due to the interaction of water with the $-\text{OH}$ groups on the pore surface. It is known, that water, or a monolayer of water becomes physisorbed on silanol groups. Silanol groups are present both at the silica glasses surfaces and at the cement pores surfaces. NMR research has shown that at least two monolayers of physisorbed water do not freeze in silica pores at 140K. However, there are no many studies available on the interaction of water-silanol groups and temperature dependency below 0°C . The other explanation concerns hydrated calcium ions in cementitious materials not present in silica glasses. However, little is known about C-S-H surfaces.

Chapter 6

Study of C-S-H drying shrinkage and relaxation on rewetting.

6.1 Background

One of the TRANSCEND projects was devoted to the concrete water intake studies by means of the one-sided GARField NMR (Fischer, 2015; Fischer et al., 2015). These studies indicated that after saturated concrete had been dried and rewet, the volume of water filled capillary spaces increased, compared to the pre-dried concrete sample. With time, capillary water level dropped back close to the original value. One of the differences between the NMR used in this work and one-sided GARField NMR is that GARField is not sensitive to the inter-layer and gel water in the C-S-H. Thus the decision was made to investigate this phenomena with the NMR at LafargeHolcim laboratories. The advantage of NMR at LafargeHolcim is that inter-layer, gel water and capillary water volumes can be monitored simultaneously thus opening greater insight on the discovered phenomena.

6.2 Methods and materials

6.2.1 Mixing and curing

White cement powder with the composition: 65.3% C₃S; 26.9% C₂S; 2.9% C₃A; 2.1% CH; 0.8% CC and 1.4% CS was used. Typically water was added to 80 g of the anhydrous cement in the water to cement (*w/c*) ratios 0.36, 0.4, 0.44 by mass and mixed using the protocols established by Nanocem (www.nanocem.org) and published elsewhere (Muller et al., 2013). Samples were cast in moulds of about 1 cm³ volume and curing begun at room temperature under PURELAB®water which was added about 1 hour after casting to

the one part of the samples, just as the sample was starting to set, in order to compensate for chemical shrinkage associated with water taken up by the hydration reaction. Curing in sealed container continued for a total of 28 days at $20 \pm 1^\circ\text{C}$. At the end of the curing period, samples were individually crushed into millimetre-sized pieces to enable subsequent rapid drying and re-wetting and to avoid the problems associated with a spatially non-uniform distribution of water that occurs for larger samples, which might mask the effects we seek to measure. For instance, during wetting of a large sample, the evolution of porosity change near a water ingress front would be at a much “younger” stage of development than near the sample surface as the surface would have contacted water for a longer period. Crushed samples were measured by NMR “as-prepared”.

6.2.2 Measurement cycle

Crushed samples were subsequently dried. Drying methods were used as follows: drying at either 40°C or 60°C under slightly reduced pressure for a short period of 2 or 3 days respectively; drying at room temperature in a 23% relative humidity (RH) environment for 3 days. Previous NMR work suggests that drying for a short period at 40°C to 60°C or at 23% RH is sufficient to remove water from the gel porosity but not to remove water from the C-S-H inter-layer spaces (McDonald et al., 2010; Muller et al., 2013). Dried samples were measured by NMR and then immersed in, and stored under, water in order to rewet them. They were only removed from the water for the brief periods (a few minutes) necessary for NMR measurements at various wetting times.

For ^1H NMR relaxometry measurements, the crushed pieces of sample (the same pieces for any one experimental series) were dabbed dry with filter paper and placed in the bottom of a 10 mm diameter NMR tube. The free space was taken up by a solid glass rod to limit evaporation into the space above the sample and the whole assembly sealed with Parafilm®.

6.2.3 CPMG and Quad-echo details

A Carr-Purcell-Meiboom-Gill (CPMG) pulse sequence experiment was used for all measurements. As we have previously shown, the ^1H T_2 relaxation time distribution can be calculated from the measured CPMG echo sequence decay and directly reflects the pore size distribution of water filled porosity in the sample. The typical $\pi/2$ pulse length, $\pi/2$, was $6.5 \mu\text{s}$; 256 log-spaced echoes were recorded from $58 \mu\text{s}$ to 65 ms; the experimental repetition time was 0.565 s and 1024 averages were recorded. With these parameters it took about 8.5 minutes to record the CPMG data. Additionally, when the measurement was not thought to

be time-critical, in so much as the water distribution was not expected to change significantly during the measurement period, a quadrature echo sequence was also run.

From this experiment it is possible to determine additionally the fraction of all hydrogen protons combined in crystalline hydrates such as Portlandite (calcium hydroxide) and ettringite. Here, single quadrature or “solid” echoes were recorded for pulse gaps, τ , in the range 12 to 54 μs . The quad-echo signals were decomposed into “solid” and “liquid” fractions, and these were extrapolated back to zero pulse gap using Gaussian and exponential curves respectively. Further details of the measurement and analysis procedures are to be found in the literature Muller et al. (2015); Valori et al. (2013). Samples were weighed at every significant point of the sample preparation and measurement process.

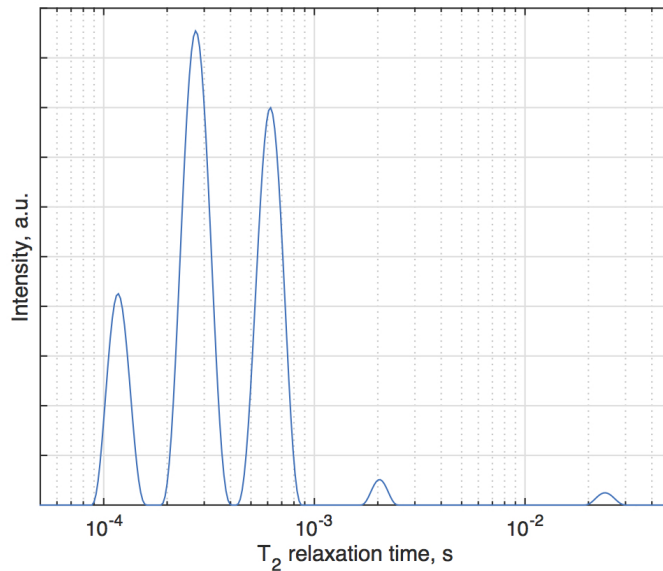


Fig. 6.1 A Lin-Log plot of the ILT fit. The data shown correspond to the 28 days underwater cured $w/c=0.36$ sample.

6.2.4 Data analysis

Most ^1H NMR CPMG data discussed in this thesis, recorded and analysed elsewhere with the TRANSCEND network is inverted using inverse Laplace transformation. This gives the quasi-continuous distribution of T_2 values for the sample Fig. 6.1. Although this method is not without its own problems, it is that method that makes the least a-priori assumptions about the T_2 distribution and is therefore preferred. The major problem is that the method requires a signal-to-noise ratio (SNR) in excess of several hundred. For the experiments discussed in this chapter, we have used small pieces of crushed sample which immediately lowers the

signal to noise ratio per scan. We have not wanted to increase the number of averages unduly for fear of changing the water or porosity distribution during the measurement time. Also, some samples are very dry, limiting the signal-to-noise ratio for want of signal from water in the sample. With lower signal-to-noise ratio, peaks in the inverse Laplace transform can become broadened or merged, masking the effects we seek to measure. In consequence, in addition to inverse Laplace analysis, we have also performed constrained multi-exponential fitting (Fig. 6.2) using as constraints the expected number of peaks and the T_2 relaxation time values of as prepared material now well-known from earlier published studies (Muller et al., 2013, 2012).

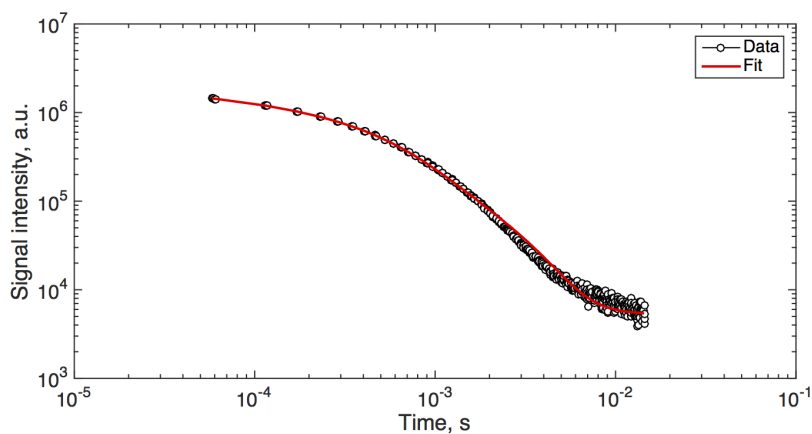


Fig. 6.2 A log-log plot of the CPMG decay together with a constrained multi-exponential fit as described in the text. The data shown correspond to the 28 days underwater cured $w/c=0.4$ sample.

The exponential fitting was constrained as follows. First, the “as-prepared” material was fit to a four component exponential decay for which the three shortest time constants were forced in the ratio 1:3:9. The actual relaxation time values of water in the smallest pores depend on the pore size and level of paramagnetic impurities in the sample. However, previous work (Muller, 2014) says that sizes and its T_2 values occur in this ratio, associated with, in order, water in interlayer spacing in the gel hydrates, water in gel pores and water in interhydrate pores. The fourth time constant was set equal to 40 ms - a generic value for large pores that has marginal effect on the quality of the data fitting. The amplitudes were left to float, so making a fit with five free parameters (four amplitudes and the shortest time constant). Thereafter, the time constants were maintained fixed across a sample set so that in analysis of re-wet material only the four amplitudes were varied.

6.3 Results

6.3.1 Sample dried at 60°C

Fig.6.3 shows the evolution of the different water fractions of a 28-day underwater cured sample $w/c=0.4$ before and after drying and then measured periodically during the first two weeks of re-wetting. The sample is oven dried at 60°C for three days at 0.9 bar. It is evident that there is minimal mobile water remaining in the hydrate interlayer spaces and almost none in larger pores of the sample after drying compared to pre-drying. What follows concerns the subsequent rewetting. The discussion is further aided by inspection of Fig. 6.4. This figure shows the combined water in the interlayer and gel pores and the combined water in interhydrate and capillary pores as well as their sum, the total mobile water. We continue to use names already introduced to differentiate between pores of different size where the meaning is clear. However, since we will envisage that some gel pores collapse to a size comparable to the interlayer and so enlarge other gel pores to a size comparable to the interhydrate, we also introduce the terminology “finer porosity” to reflect pores less than about 10 nm and “coarser porosity” for pores greater than about 10 nm. Hence Figure 6.4 shows water in these two categories and their sum.

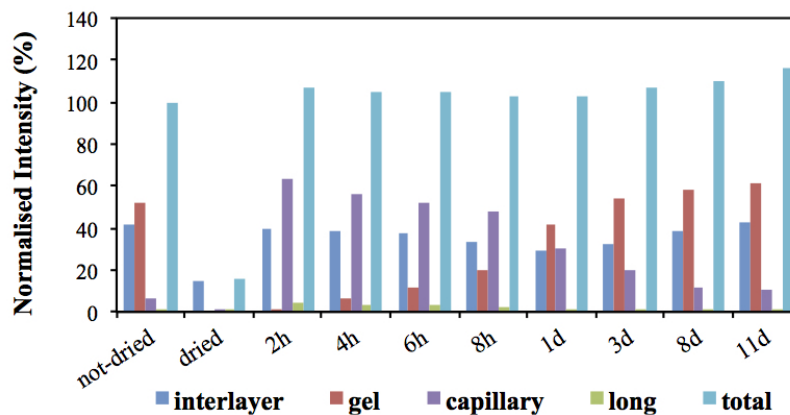


Fig. 6.3 The evolution of water components of a sample: as prepared; after drying and then after 2, 4, and 8 hours and \approx 1, 3, 8 and 11 days of rewetting expressed as a percentage of the NMR-total water in the “as-prepared” sample. The sample was cured for 28 days underwater with $w/c=0.4$; oven dried at 60°C and 0.9 bar for 3 days.

The first observation is that the total filled porosity of the sample very quickly re-establishes itself to its pre-drying value (Figure 6.4). It gets to 97% in 2 hours and exceeds the pre-drying value after 11 days. This is reasonable because the crushed samples contain a significant number of capillary pores that are empty due to self-desiccation in the “as-prepared” material notwithstanding the so-called underwater curing. It is also possible that

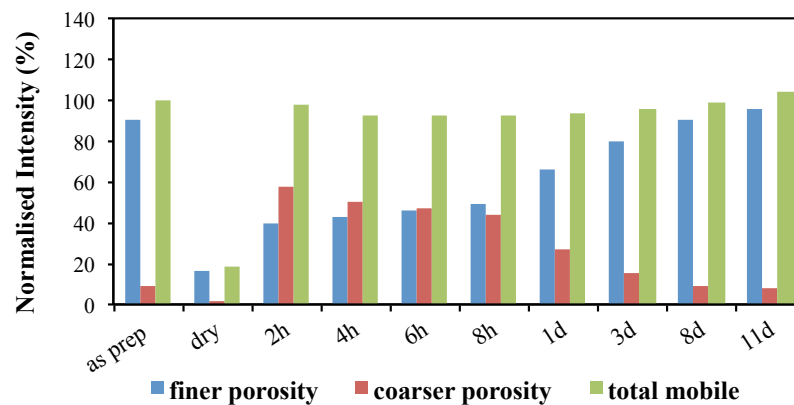


Fig. 6.4 The evolution of mobile water in finer (<10 nm) and coarser (>10 nm) porosity for sample dried for 3 days at 60°C expressed as a percentage of the total mobile water. The sample was underwater cured for 28 days, $w/c=0.4$.

the largest pores dried slightly during crushing. However, the former explanation is more likely since the increase is larger for a sealed-cured sample (data is shown below).

The second observation offers far greater insight. It is that the distribution of water between finer (<10 nm) and coarser (>10 nm) hydrate porosity changes dramatically during rewetting. It is seen most obviously in Figure 6.4. After 2 hours the amount of water in the finer porosity is approximately 39% the total pre-drying mobile water whereas the combined amount of water in coarser porosity is about 58%. This contrasts very strongly with pre-drying when the finer porosity was the dominant fraction, about 90%, while the coarser porosity was less than 10%, about 9 times smaller. However, by about 6 hours, the volume of finer porosity water has increased dramatically while the coarser porosity water has decreased. The two fractions are approximately equal. At 8 days, the finer porosity water is approaching equilibrium and has regained the pre-drying volume, (90%). The volume of coarser porosity water has continued to decrease correspondingly and is roughly the same as the pre-drying amount.

Figure 6.3 provides additional information. In the early stages of re-wetting, all the interlayer / gel pore water is seen as interlayer water. At 12 days, the amount of interlayer water is almost exactly equal to that pre-drying. The reduction in water in the finer porosity is associated almost entirely with the gel pores. For the coarser porosity, the increase in water in pores of interhydrate size (circa 20 nm) accounts almost exactly for the decrease in gel pore water. It is the capillary pores that account for the increase in the overall total of mobile water. This fact supports the idea that the total increase results from a filling of previously unfilled capillary porosity. If the data had sufficient signal to noise, a proper inverse Laplace transform might reveal details more precisely.

6.3.2 Severity of drying

The same story does not carry over to a sample oven dried at 40°C and 0.9 bar for a short period of just 2 days, Figure 6.7. Although, as before, the sample re-wets quickly, getting near the pre-drying level within 2 hours, the distribution of water between the finer porosity and coarser porosity remains essentially unchanged throughout the rewetting period. There is very little subsequent evolution of the amount of water in different pore types.

This study was performed in parallel with a second study by Gajewicz and Kang at University of Surrey. Independent sets of samples were prepared and analysed at Surrey University laboratories (NMR frequency 20 MHz). The parallel study also investigated the first sorption cycle and found broadly similar results. This study used different drying mechanism and the results were found to interleave with the results reported here when sorted in terms of severity. The study at University of Surrey went on to look at second sorption cycle.

Potentially, two factors are at play in these phenomena: the severity of drying and the duration of drying / storage. Table 6.1 seeks to separate the factors. It provides an indicator of the drying severity, measured as the fraction of the interlayer and gel pore water removed by drying. On the sample studied by the author at LafargeHolcim it is seen that oven drying for three days at 60°C is most severe. Drying at 40°C for 2 days is least severe by this measure. However, one of the Surrey samples is more extremely dried and another less extremely dried. The first shows time dependence, the second does not.

Drying	Duration of drying	Gel and interlayerpores removed (%)
LafargeHolcim data		
60°C oven at 0.9 bar	3 days	81
Direct to 23% RH at 20°C	3 days	54
40°C oven at 0.9 bar	2 days	44
Surrey data		
60°C oven at 0.9 bar	1 month	91
Progressively down to 15% RH at 20°C	1 month	64

Table 6.1 The duration and severity of the different drying regimes, the latter measured by NMR as the fraction of finer porosity water removed from the cement paste.

The data shown at of Fig.6.5 and Fig.6.6 allow us to explore the severity of drying more closely. Figure 6.5 is for a sample dried at 60°C for 3 days. The amount of coarse porosity seen after 11 days rewetting is reduced while the amount of finer porosity is increased.

The data shown in Fig.6.6 obtained from samples that were dried directly to 23% RH at room temperature for 3 days. This drying regime is less severe than the 60°C drying. Over half of the finer porosity water is removed. In this cases, the sample re-adsorb water to the overall pre drying level within the first two hours and do not show any subsequent redistribution. This is akin to the sample least severely dried at 40°C. However the distribution of water between finer and coarser porosity in the sample taken down to 15% RH is more-or-less the same in the taken to 23% RH. Again we conclude that, at least for these drying conditions, the period of drying is not significant. However, what clearly differentiates between samples behaving as in Fig.6.4 from those in Fig.6.7 is whether or not the drying has significantly impacted the water content in the interlayer spaces. Drying at 60°C removes a large fraction of interlayer water; drying at 40°C does not.

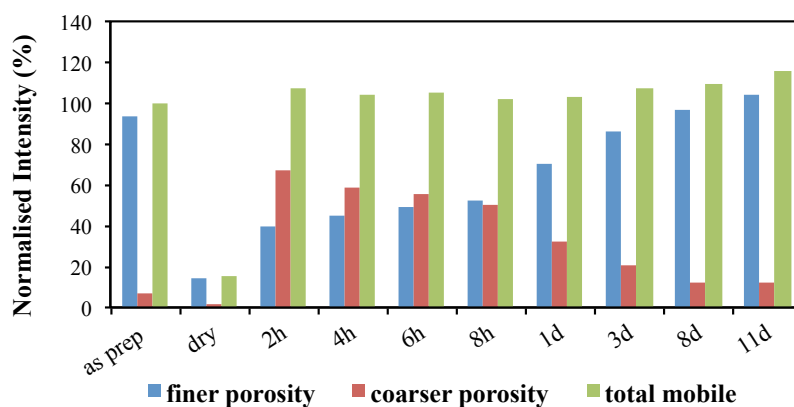


Fig. 6.5 The combined finer and coarser pore water for the sealed cured $w/c=0.4$ sample dried at 60°C for 3 days

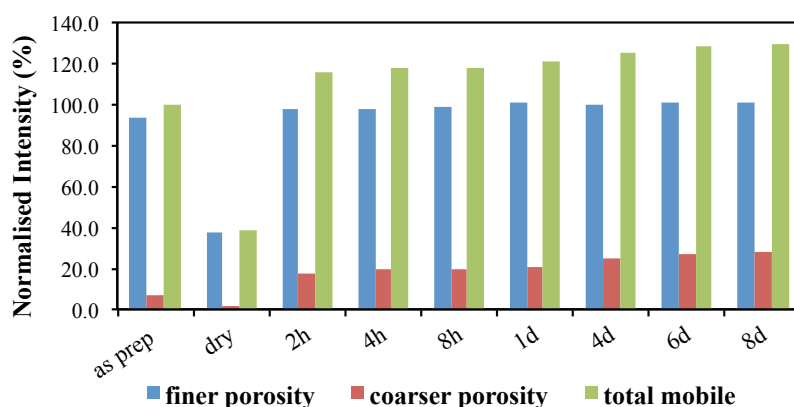


Fig. 6.6 The combined finer and coarser pore water for the sealed cured $w/c=0.4$ sample dried directly to 23% RH

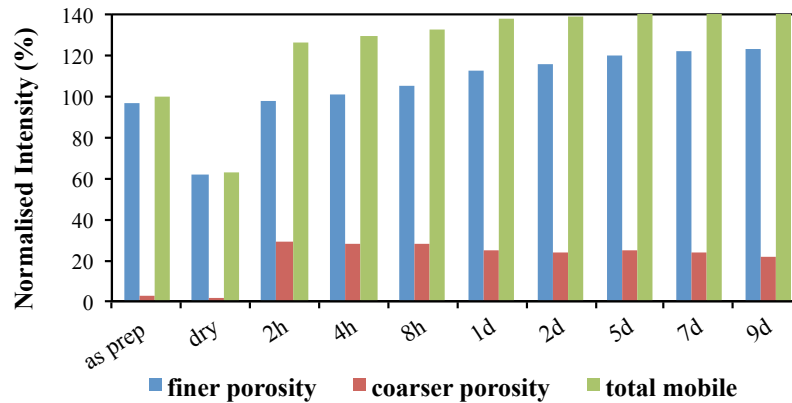


Fig. 6.7 The combined finer and coarser pore water for the sealed cured $w/c=0.4$ sample dried at 40°C for 2 days

6.3.3 Varying w/c ratio

The same experiments were performed on samples with $w/c= 3.6$ and 4.0 for both sealed and under water curing.

Sealed cured samples with $w/c=0.36$ were dried at 23% RH (Figure 6.8), dried at 40°C for 2 days (Figure 6.9) and dried at 60°C for 3 days (Figure 6.10). Same drying was applied to the water cured samples with the same $w/c=0.36$. Dried at 23% RH (Figure 6.11), dried at 40°C for 2 days (Figure 6.12) and dried at 60°C for 3 days (Figure 6.13).

For water cured samples with $w/c=0.4$ same drying was applied. Dried at 23% RH (Figure 6.14), dried at 40°C for 2 days (Figure 6.15) and dried at 60°C for 3 days (Figure 6.16).

For gently dried samples (dried at 23% RH and 40°C for 2 days) there is an irreversible change in the porosity distribution for each sample comprising a swing from smaller to larger pore size distribution. This is equivalent to about 10% of the total filled porosity in the sealed cured samples but it is about half this in the water cured samples. It does not seem to depend on w/c that only really affects the total porosity. The difference may be related to the way that shrinkage pores are filled in the "as prepared" water cured samples compared to the sealed samples, but we do not really know.

There is the dynamic dependence of the changes in the more severely dried samples (60°C for 3 days) for each of the different water to cement ratios whichever way the samples are prepared. In the sealed samples this is clearly additional to the irreversible change, but the irreversible change is more ambiguous in the severely dried water cured sample compared to the sealed sample. Again w/c ratio has little effect. The effect w/c does have is to change the total porosity but this is not seen from this data. Also, the change from underwater cured to sealed cured affects the total water content of the "as prepared" material, but again it is

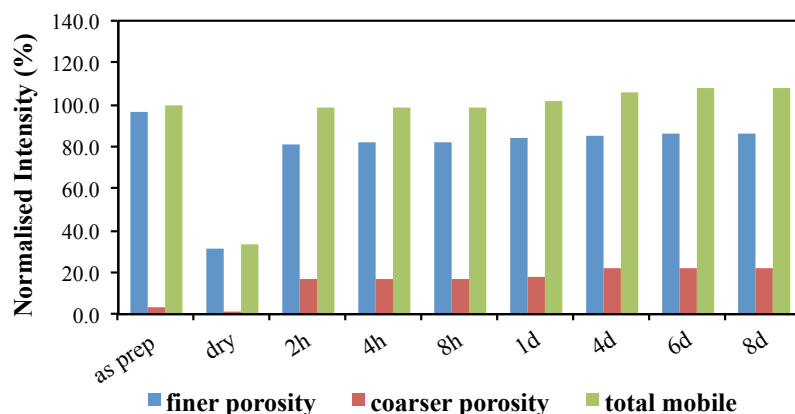


Fig. 6.8 The combined finer and coarser pore water for the sealed cured $w/c=0.36$ sample dried sample dried directly to 23% RH

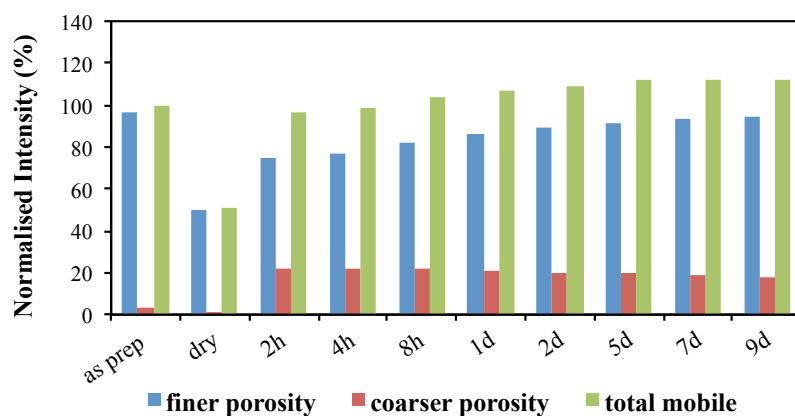


Fig. 6.9 The combined finer and coarser pore water for the sealed cured $w/c=0.36$ sample dried at 40°C for 2 days

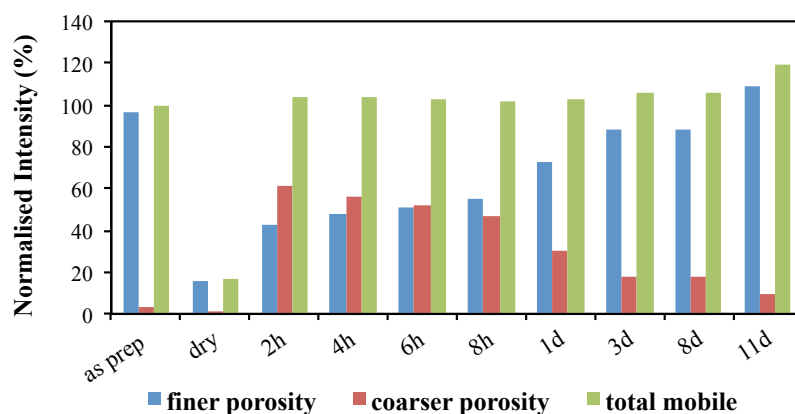


Fig. 6.10 The combined finer and coarser pore for the sealed cured $w/c=0.36$ sample dried at 60°C for 3 days

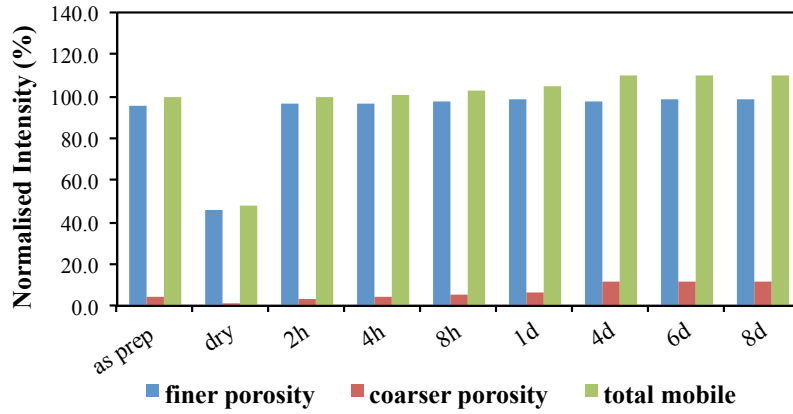


Fig. 6.11 The combined finer and coarser pore water for the water cured $w/c=0.36$ sample dried sample dried directly to 23% RH

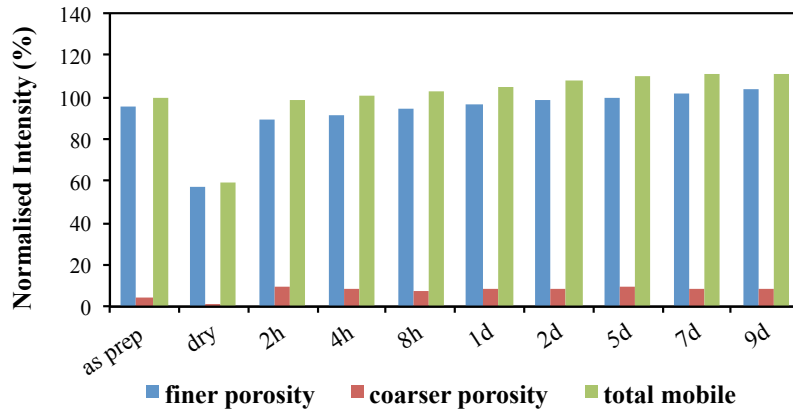


Fig. 6.12 The combined finer and coarser pore water for the water cured $w/c=0.36$ sample dried at 40°C for 2 days

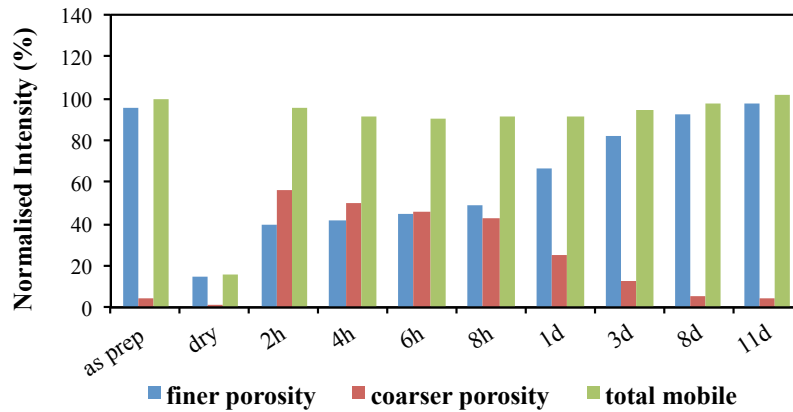


Fig. 6.13 The combined finer and coarser pore water for the water cured $w/c=0.36$ sample dried at 60°C for 3 days

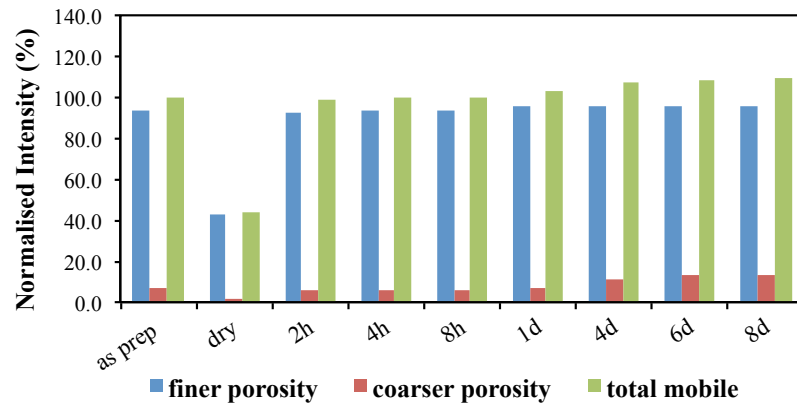


Fig. 6.14 The combined finer and coarser pore water for the water cured $w/c=0.4$ sample dried sample dried directly to 23% RH

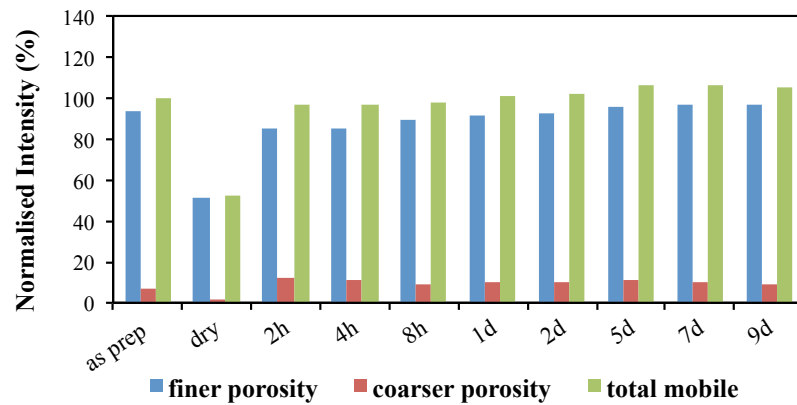


Fig. 6.15 The combined finer and coarser pore water for the water cured $w/c=0.4$ sample dried at 40°C for 2 days

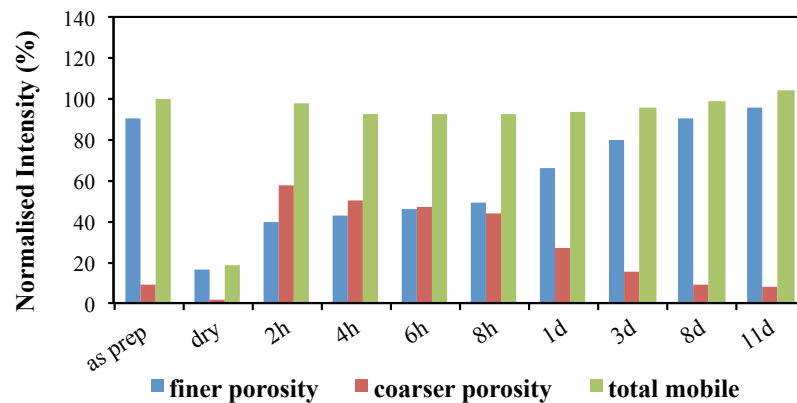


Fig. 6.16 The combined finer and coarser pore water for the water cured $w/c=0.4$ sample dried at 60°C for 3 days

not seen these data. Both effects are seen in different experiments without normalisation to 100% and without sample crushing (Cook and Hover, 1999).

6.3.4 Second sorption cycle

Further comparison could be found at Gajewicz et al. (2016). The first sorption data showed the existence of reversible and irreversible processes on the rewetting. In the second sorption cycle data the main question was whether these changes could be seen again.

Experiments were performed on samples with two cycles of drying and rewetting. Moreover, more severe "oven drying" and less severe "drying over RH salts" were used for the two cycles in all four possible combinations "oven – oven"; "oven — salt"; "salt — oven"; "salt — salt". These experiments were performed by Agata Gajewicz and Koljeet Kang at the University of Surrey. In summary, most irreversible changes were seen only in the first drying cycle. However, a dynamic (time dependent) change in the pore size distribution was seen after oven drying in either the first and/or second cycle.

6.3.5 Study of robustness of data fitting

The fit formula is a sum of four component fit:

$$M(t) = \sum_{i=1}^4 M_0^i \exp\left[-\frac{t}{T_i}\right] \quad (6.1)$$

As it was mentioned before, from previous experiments it has been concluded that for a standard white cement paste, the three shortest time constants could be fitted with values in the ratio 1:3:9, with the first T_2 equal 185 μs . In order to test the robustness of this forced fit we have varied first relaxation time value and fitted data with different ratios for an analysis of sample the earlier results of which are represented in Fig 6.17. The parameters used for the fit are gathered in the Table 6.2. The corresponding results can be seen at Figure 6.17.

As it can be seen on Figure 6.17 variation of the fit parameters change the output results. In most cases the broad trend of the earlier results is retained although there is now considerable "scatter" in the data. For instance, at Figure 6.17c and Figure 6.17e part of the gel pore signal is completely lost at 2, 4, 6 hours. Parameters used for the fits Figure 6.17b and Figure 6.17d show constant increase in interhydrate pores volume with time. Unconstrained fit shown at Figure 6.17f is absolutely random every new time it is used. Here only one possible fit is shown. Only the fit with the T_2 times ratio 1:3:9 and starting point at 185 μs is inline with the results obtained with the ILT and non-dried samples investigated in the past.

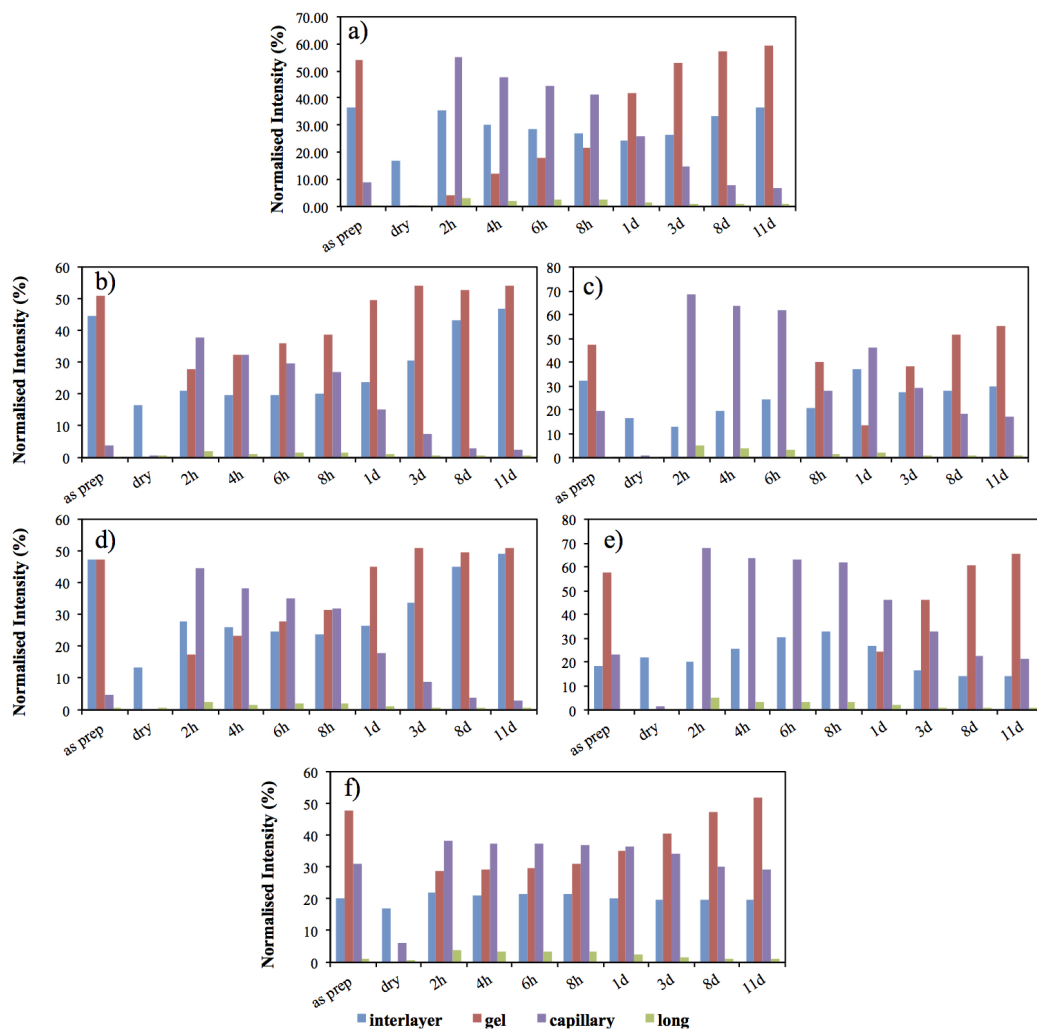


Fig. 6.17 Results of the fitting with the corresponding parameters gathered in the Table below with (a) fit parameters used in this work, (b)-(e) variety of parameters were used in order to test the robustness of the fit (see Table below) and (f) unconstrained fit.

Table 6.2 Fit parameters used to test the robustness of the forced fit.

	First T_2 μs	Second T_2 μs	Third T_2 μs
a	185	$1^{st} \times 3$	$1^{st} \times 3^2$
b	185	$1^{st} \times 3.5$	$1^{st} \times 3.5^2$
c	185	$1^{st} \times 2.5$	$1^{st} \times 2.5^2$
d	225	$1^{st} \times 3$	$1^{st} \times 3^2$
e	125	$1^{st} \times 3$	$1^{st} \times 3^2$
f	unconstrained		

During the first 24 hours of rewetting the sample was taken out of water every two hours for the measurements and put back into the water afterwards. From previous experience, it is known that CPMG data and thus ILT output is highly sensitive to such non-equilibrated samples. ILT gives a good output when measured sample resides in the tube untouched with minimum of disturbance and when the signal-to-noise ratio is excellent. It can be said that the unconstrained fit is in some sense similar to the ILT fitting. In both cases the result is not unique and can be different for different fitting initiation values. The fit parameters at Table 6.2a are reproducible and are in agreement with previous results (Muller et al., 2012).

6.4 Discussion

An explanation of the combined study represented by this work and the parallel study at Surrey is drawn schematically in Figure 6.18. The schematic is for a sample in which the gel porosity is completely emptied of water and then refilled. Figure 6.18a shows some C-S-H sheets separated by interlayer spaces. Gel pores are seen between regions of locally aggregated sheets. The gel pores are filled with water, drawn as circles. The interlayer spaces also contain water but this is not shown. The gel pores are a few (3-5) nanometres in size. Interhydrate pores are slightly larger and are original-mix water filled spaces between regions of C-S-H into which further C-S-H could possibly grow. However these are not drawn. As water is removed from the system, Figure 6.18b, we imagine that surface energy or disjoining pressure forces distort the local arrangement of the sheets so as to “zip them up” into locally-thicker stacks. The surface forces overcome local bending stresses in order to do this. The result is the average gel pore size increases although the total volume does not, at least to a degree measurable by NMR. When water reinvades the sample, it initially finds larger pores that are apparently more comparable to interhydrate pores in size. With time, the “zipped” sheets “unzip”. That is they relax in response to the changed balance of surface forces and bending stresses. Something closer to the original microstructure re-appears. It is very noticeable that we see this result most prominently with the most severe drying method: 2-3 days 60°C. We do not see it with the least severe methods. A key difference is that the more severe drying removes a significant fraction (over half) of the interlayer water. Perhaps with less severe drying, sufficient water is retained in the smallest spaces to prevent large surface energy or disjoining pressure forces from building up. Local “zipping” of sheets cannot occur. The vapour pressure of water is about 3 times higher at 40°C than at 20°C, and 9 times higher at 60°C. So, if the laboratory atmosphere is circa 60% RH at 20°C, then a sample in an unsealed oven at 60°C experiences about 7% RH, quite sufficient to impact the interlayer in an equilibrated sample. However, 40°C leads to 20% RH and is much less

impactful. It is striking that our results show the greatest effects for the most severely dried sample but that the drying rate does not seem to be a primary indicator of change. This contrasts with the work of Maruyama et al. (2014) who emphasise the importance of drying rate on the shrinkage strain of hardened cement paste during the first desorption process although the timescales in this work do not extend as far as those explored by Maruyama et al. (2014).

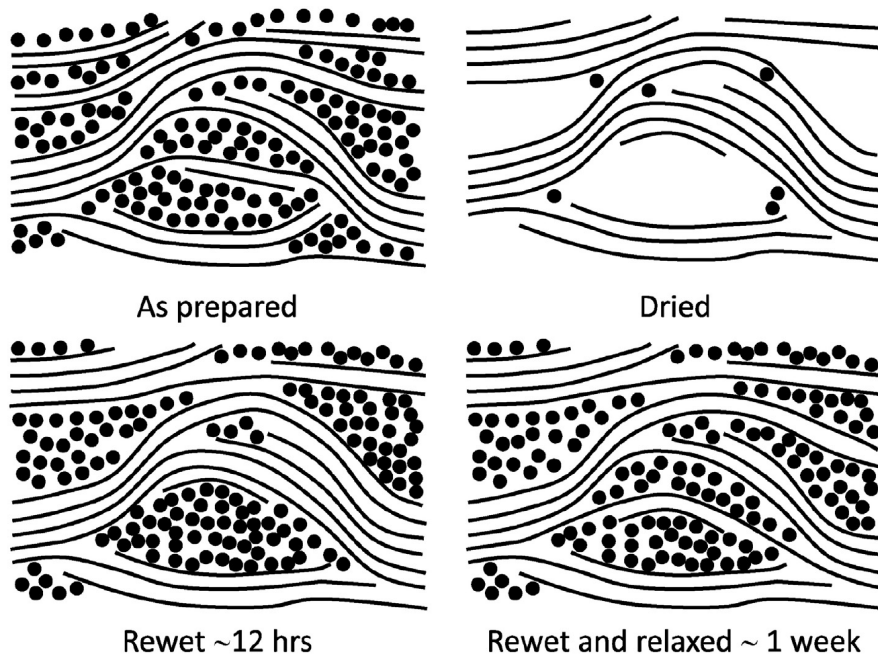


Fig. 6.18 Top left: A schematic of the water in the gel pores of an “as-prepared” paste. The solid lines are the hydrate backbone sheets of the C-S-H gel. The circles are water molecules. The interlayer water between the sheets is not shown. As a guide to scale, the layer spacing is about 1.5 nm. Top right: The hydrate after sufficient drying to remove almost all the water from the gel pores. Surface forces cause some sheets to distort and “zip-up”. Bottom left: the same structure shortly after rewetting. The exact same amount of water as top left is shown, but it is now in fewer, and, on average, slightly larger pores. Bottom right: after a few days the hydrate partially relaxes closer to the original microstructure. Again, the same amount of water is shown. The pores doesn’t look smaller than initial structure.

One surprise in our data is that we do not see more interlayer water in samples that show the evolving porosity at the end of the rewetting period compared to pre-drying. Figure 6.18 makes clear that if the average gel pore size at the end is increased, then this increase is accompanied by locally thicker stacks of layers. The number of interlayers is increased. One explanation is simply that we are unable to resolve differences of this magnitude. However, we think this is unlikely. Another explanation is that some of the original water

that is removed from interlayer spaces is not replaced. This decrease in water per interlayer compensates for the increase in the number of interlayers. It is well known that the first drying cycle of cement paste yields a mixture of reversible and irreversible changes in sorption isotherms and shrinkage. However, these differences tend to be associated with the high RH end of the drying spectrum (Jennings, 2008; Jennings et al., 2015; Maruyama et al., 2014). To first order, only reversible changes are seen after the first cycle. We note that in this work, the changes are associated with the most severe drying, that is the low RH end of the spectrum. However, there are reversible and irreversible changes. From the work performed by Agata Gajewicz at Surrey (Gajewicz et al., 2016) on the second cycle we know that irreversibility continues to be associated with the first cycle only. Maruyama et al. discuss the shrinkage mechanism in terms of Jennings' colloidal model of cement microstructure (Jennings, 2008). They conclude that the increase in porosity due to larger pores occurs by the flocculation of C-S-H globules whereas the decrease in porosity due to smaller pores arises from densification of the C-S-H through the loss of interlayer water. Thus they are seen as different processes. Moreover they are believed to occur in different ranges of RH. This is because the Kelvin Laplace equation links RH to the size of emptying pores. If the increase in apparent proper (micron) capillary porosity that we see through the filling of previously empty pores is removed from the equation, then the growth in coarser porosity is almost exactly matched by the loss of finer porosity. Given that Maruyama et al. describe different processes associated with different parts of the microstructure and different RH ranges, it is therefore surprising that the growth in finer porosity that we see in re-wetting is so closely mirrored by the decline in coarser porosity. It seems much more likely to us that they are opposite sides of a single process. Such a single process can be built on rearrangements of C-S-H sheets at the gel pore scale based on a Feldman and Sereda type micro-structural model (Feldman and Sereda, 1970) as it is depicted in Figure 6.18. However, this explanation is unable to explain the conclusion of Maruyama et al.: that the two processes come about at different ranges of RH. Macroscopic drying shrinkage, to which NMR is not sensitive, may provide part of the answer.

Notwithstanding the comments immediately above, there is ongoing controversy as to whether or not C-S-H is a quasi continuous (Feldman and Sereda, 1970) or colloidal particle like layered structure (Jennings, 2008). While the data in this work has been interpreted in terms of the quasi continuous model, it would be possible to rework the discussion in terms of the colloidal model. Nothing in the new data is incompatible with either.

6.5 Conclusions

Taken together, the results discussed in this study and the parallel study by A. Gajewicz and K. Kang indicate strong support for the idea of nanoscopic rearrangement of the gel porosity in dried cement pastes and that this rearrangement is partially reversible on timescale of 24-48 hours after rewetting. The combined studies have been published in Cement and Concrete Research, Volume 86, August 2016, "A ^1H NMR relaxometry investigation of gel-pore drying shrinkage in cement pastes".

Chapter 7

$T_2 - T_2$ on the C_3S

7.1 Introduction

In this chapter 2D 1H NMR exchange experiments performed on the synthesised C_3S are presented. The objective of the work was to try and identify the exchange pathways between the three main pore networks (interlayer space, gel pore and inter-hydrate or capillary pore) by freezing out successively larger pores as the sample is cooled to about $-60^\circ C$. Previous work on cement pastes had only looked at the connectivity of two of these pores types (interlayer and gel) and at room temperature only. An attempt to model the relaxation behaviour has been made in order to explain the results better. This involved writing a data simulation code in MATLAB. The mathematical model is an extension to three-sites of the two-site analysis by Monteilhet et al. (2006) for the two-site exchange. It is similar to the $T_2 - T_2$ experiment model discussed by Van Landeghem et al. (2010) that is also an extension of that work.

The $T_2 - T_2$ experiment is known to be effective for exchange monitoring. It consists of two encodings of the T_2 magnetisation decay at two successive times separated by a short magnetization storage interval during which only T_1 relaxation occurs. The time between two encodings τ_{ex} is varied to explore the time of the exchange. A 2D inverse Laplace transformation of the data is made. This converts the data to a map of T_2 in the first encoding interval against T_2 in the second. Diagonal peaks on the plot show nuclei which do not move between pores of different size during the τ_{ex} , that is they have the same T_2 in both encoding periods. Off-diagonal peaks indicate the presence of exchange between pores of different sizes (Washburn and Callaghan, 2006). That is T_2 is different in the two encoding periods.

7.2 Prior work

McDonald et al. (2005) studied cement pastes with the $T_1 - T_2$ experiment. It was confirmed by McDonald et al. (2005) that there are discrete reservoirs and there is ongoing exchange between them. However, only the exchange that is now believed to be between interlayer spaces and gel pores was studied. The disadvantage of the $T_1 - T_2$ method is that it is not possible to separate unambiguously off-diagonal exchange peaks between pores of different size from a signal from the crystal solid that has a long T_1 and short T_2 . Also it has been shown that one off-diagonal peak is inverted and not properly found by a ILT with non-negative constraint (McDonald et al., 2005).

One of the first applications of the $T_2 - T_2$ was done by Washburn and Callaghan (2006). The work has been performed on sandstone with different storage times τ_{ex} . By carefully extracting information of the T_2 values of the exchange peaks and corresponding magnitudes as a function of storage times, τ_{ex} , a numerical value for the exchange rate between different pore population in the sandstone was evaluated.

Monteilhet et al. (2006) performed $T_2 - T_2$ on white cement paste samples. Pores in cement are much smaller than in the sandstone. This paper provides the mathematical solution for the two-site exchange experiment analysis. Also the data for the white cement with storage times in the range $\tau_{ex} = 1$ ms and $\tau_{ex} = 6$ ms is shown. Intensities of the exchange peaks are studied as well. However, due to the quick relaxation in cement, only gel to interlayer pore exchange has been studied. Pore sizes and water diffusion coefficients were calculated based on the exchange data using a much fuller analysis than done by Washburn and Callaghan (2006). It is now believed that exchange was actually between interlayer and gel.

In other application of $T_2 - T_2$ by Valori et al. (2010) synthesised C-S-H and white cement samples were studied. The primary purpose was to exclude the possibility of exchange between 2 pores of the same size but different surface relaxivity. Another purpose of the work was to see the differences in relaxation times and corresponding T_2 times of C-S-H pore populations as a function of Fe^{3+} concentration. Synthesised C-S-H data compared to white cement data shows longer T_2 values due to the negligible Fe^{3+} concentration compared to white cement. The data for $\tau_{ex} = 3$ ms is shown. The exchange is detected in both cases, but with very different T_2 values.

Later Van Landeghem et al. (2010) built a numerical model for the 3 site exchange for the $T_2 - T_2$ experiment. This was done in order to explain the existence of the non-symmetrical exchange peaks in the data. However, we did not get this type of non-symmetry of exchange peaks as it will be shown later. It is possible that this could be explained by the appropriate selection of the phase cycle as it will be discussed later in this thesis.

7.3 NMR theory

Mathematics for the two-site exchange problem is based on the numerical solution of a pair of coupled differential equations for the two magnetisation populations associated with pore types A and B of different size, as shown by McDonald et al. (2005).

Two reservoirs with the magnetisations M^a and M^b are connected. Thus there is exchange between them. The system of coupled differential equations governing the relaxation of the magnetization M^a and M^b in the reservoirs is:

$$\frac{dM_a}{dt} = -k_a M_a + k_b M_b + R_a (M_a^{eq} - M_a) \quad (7.1)$$

$$\frac{dM_b}{dt} = -k_b M_b + k_a M_a + R_b (M_b^{eq} - M_b)$$

where $k_{a,b}$ is exchange rate between the pores and $R_{a,b}$ is a relaxation rate equal to $1/T_{2a,b}$. $M_{a,b}^{eq}$ is equilibrium magnetisation for each site and t is a time. These equations can be written in the form

$$\begin{bmatrix} d(M_a - M_a^{eq})/dt \\ d(M_b - M_b^{eq})/dt \end{bmatrix} = \begin{bmatrix} -R_a - k_a & k_b \\ k_a & -R_b - k_b \end{bmatrix} \begin{bmatrix} M_a - M_a^{eq} \\ M_b - M_b^{eq} \end{bmatrix} \quad (7.2)$$

since $\frac{dM_{a,b}^{eq}}{dt} = 0$.

$T_2 - T_2$ experiments consists of three encoding periods t_1 , t_2 and t_3 . The observed magnetization M is the sum of M_a and M_b .

During the first encoding period, which is a CPMG experiment, $M_a^{eq} = M_b^{eq} = 0$. $R_a = 1/T_{2a}$ and $R_b = 1/T_{2b}$. The initial magnetisation at $t = 0$ is $M_a(0) = M_a^0$ and $M_b(0) = M_b^0$.

During the second encoding period, the magnetisation is recovering towards equilibrium so that $M_a^{eq} = M_a^0$ and $M_b^{eq} = M_b^0$ by T_1 recovery so $R_a = 1/T_{1a}$ and $R_b = 1/T_{1b}$. The initial values are the final values of the first encoding period.

During the third encoding period, it is CPMG again. So the parameters are the same for the first period except that the initial values are the final values of the second period. The final values of the third period are the measured values. For the fixed t_2 , data is recorded as a function of t_1 and t_3 making a 2 dimensional relaxation data set.

The final solution is given by Monteilhet et al. (2006) and is:

$$M(t_1, t_2, t_3) = C_1(t_3)[C_2(t_1, t_2) + C_3(t_1, t_2)] + C_4(t_3)[C_5(t_1, t_2) + C_6(t_1, t_2)] \quad (7.3)$$

where

$$C_1(t_3) = (A_2^- - F_2) \exp(s_2^+ t_3) + (A_2^+ + F_2) \exp(s_2^- t_3) \quad (7.4)$$

$$C_2(t_1, t_2) = M_a^0 + [A_1^- \exp(s_1^+ t_2) + A_1^+ \exp(s_1^- t_2)] \times [-M_a^0 + (A_2^- M_a^0 - G_2 M_b^0) \exp(s_2^+ t_1) + (A_2^+ M_a^0 + G_2 M_b^0) \exp(s_2^- t_1)] \quad (7.5)$$

$$C_3(t_1, t_2) = -G_1 [\exp(s_1^+ t_2) - \exp(s_1^- t_2)] \times [-M_b^0 + (B_2^- M_b^0 - F_2 M_a^0) \exp(s_2^+ t_1) + (B_2^+ M_b^0 + F_2 M_a^0) \exp(s_2^- t_1)] \quad (7.6)$$

and where the two eigenvalues s_i^+ and s_i^- are used, with $i = 1, 2$, such that

$$s_i^+ = \frac{-1}{2} (R_{ai} + k_a + R_{bi} + k_b) + \frac{1}{2} * ((R_{ai} + k_a + R_{bi} + k_b)^2 - 4((R_{ai} + k_a)(R_{bi} + k_b) - k_a * k_b))^{1/2} \quad (7.7)$$

$$s_i^- = \frac{-1}{2} (R_{ai} + k_a + R_{bi} + k_b) - \frac{1}{2} * ((R_{ai} + k_a + R_{bi} + k_b)^2 - 4((R_{ai} + k_a)(R_{bi} + k_b) - k_a * k_b))^{1/2} \quad (7.8)$$

$$A_{1,2}^{+/-} = \frac{s_{1,2}^{+/-} + R_a^{1,2} + k_a}{s_{1,2}^{+/-} - s_{1,2}^{-/+}} \quad (7.9)$$

$$B_{1,2}^{+/-} = \frac{s_{1,2}^{+/-} + R_b^{1,2} + k_b}{s_{1,2}^{+/-} - s_{1,2}^{-/+}} \quad (7.10)$$

$$F_{1,2} = \frac{k_a}{s_{1,2}^- - s_{1,2}^+} \quad (7.11)$$

$$G_{1,2} = \frac{k_b}{s_{1,2}^- - s_{1,2}^+} \quad (7.12)$$

The condition of mass balance requires $k_a M_a^0 = k_b M_b^0$, where M_a^0 and M_b^0 are magnetizations of each site at the time $t = 0$.

This evolution of the magnetization in the presence of exchange with time is given by eq. 12 McDonald et al. (2005).

7.3.1 Three-Site exchange model

The three site problem parallels the two site problem except that it uses three magnetisation reservoirs M_a , M_b and M_c with exchange rate such as k_{ba} for exchange from b to a , for instance.

The equation to be solved is:

$$\begin{bmatrix} d(M_a - M_a^{eq})/dt \\ d(M_b - M_b^{eq})/dt \\ d(M_c - M_c^{eq})/dt \end{bmatrix} = \begin{bmatrix} -R_a - k_{aa} & k_{ba} & k_{ca} \\ k_{ab} & -R_b - k_{bb} & -k_{cb} \\ k_{ac} & k_{bc} & -R_c - k_{cc} \end{bmatrix} \begin{bmatrix} M_a - M_a^{eq} \\ M_b - M_b^{eq} \\ M_c - M_c^{eq} \end{bmatrix} \quad (7.13)$$

To date there is no analytical solution to the 3-site exchange problem. However, we can solve eq. 7.13.

At first we define three starting magnetisation which represent the volume of each pore site M_a^0 , M_b^0 and M_c^0 . Each reservoir has a corresponding relaxation rate $R_i = 1/T_{2i}$ in the first and third interval and $R_i = 1/T_{1i}$ in the second where $i=a,b$ or c . The spin relaxation matrix consists of R_i elements, and is defined as 7.14.

$$R_{mat}^{T2} = \begin{bmatrix} R_{2a} & 0 & 0 \\ 0 & R_{2b} & 0 \\ 0 & 0 & R_{2c} \end{bmatrix} \quad (7.14)$$

Again $M_i^{eq} = 0$ in the first and third intervals and $M_i^{eq} = M_i^0$ in the second one.

Exchange times τ_{bc} , τ_{ca} and τ_{cb} are the variables that we vary in order to check experimental results. Other exchange times are defined through the conservation of mass requirements:

$$\tau_{ba} = \tau_{ab} \times \frac{M_b^0}{M_a^0}, \tau_{ac} = \tau_{ca} \times \frac{M_a^0}{M_c^0} \text{ and } \tau_{cb} = \tau_{bc} \times \frac{M_c^0}{M_b^0}. \text{ The rates } k \text{ are given as } k_{ij} = 1/\tau_{ij}.$$

Now the $k = 1/\tau$ matrix has 9 elements. It is defined as 7.15.

$$k_{mat} = \begin{bmatrix} k_{aa} & -k_{ba} & -k_{ca} \\ -k_{ab} & k_{bb} & -k_{bc} \\ -k_{ac} & -k_{bc} & k_{cc} \end{bmatrix} \quad (7.15)$$

Mass balance requires that $k_{aa} = k_{ab} + k_{ac}$, $k_{bb} = k_{bc} + k_{ba}$, $k_{cc} = k_{ca} + k_{cb}$.

The differential equations are solved using a finite element algorithm for pairs of values of $[\tau_1, \tau_3]$ for fixed exchange time τ_2 so as to build a complete $2D(\tau_1, \tau_3)$ data set. In real

experiments, the experiment is performed twice using a phase cycle so that only stored magnetisation and not relaxed magnetisation from t_2 is measured in t_3 .

Due to experimental phase cycle, it is necessary to actually perform the simulation twice: once when the start of the 2-nd interval is $+M_i(t_i)$, and once when it is $-M_i(t_i)$, and to add the results together. This ensures that the effective magnetisation relaxes toward zero in the second period so that the measured signal for long t_2 during t_3 is zero. The same result is achieved in simulation by relaxing M to zero and not M^0 in t_2 .

Since it is known that in cements $T_1 \sim 4 \times T_2$ this ratio is fixed in all subsequent analyses so as to reduce the number of free parameters.

The Matlab code to do the modelling is presented in Appendix A.

7.3.2 Code validation: 1D exchange rate

In order to validate elements of the code using the model above, we can simulate the behaviour of the two site exchange with the three site model. An effort has been made to reproduce results from Van Landeghem et al. (2010).

At this stage we calculate only a final magnetization $m_a(t) + m_b(t)$ which is inverted with the ILT software. Corresponding magnetisations are:

$$m_a(t) = \frac{((s_2^- + R_{a2} + k_a) \times M_a^0 + k_b \times M_b^0)}{(s_2^- - s_2^+)} \exp(s_2^+ \times t) + \frac{((s_2^+ + R_{a2} + k_a) \times M_a^0 + k_b \times M_b^0)}{(s_2^+ - s_2^-)} \exp(s_2^- \times t) \quad (7.16)$$

with the same for the b site

$$m_b(t) = \frac{((s_2^- + R_{b2} + k_b) \times M_b^0 + k_a \times M_a^0)}{(s_2^- - s_2^+)} \exp(s_2^+ \times t) + \frac{((s_2^+ + R_{b2} + k_b) \times M_b^0 + k_a \times M_a^0)}{(s_2^+ - s_2^-)} \exp(s_2^- \times t) \quad (7.17)$$

Two populations with equal intensity $M_A^0 = M_B^0$ starting magnetisations and T_2 's of 2.5 and 25 ms were used as an input data for a simple CPMG experiment. The model CPMG data is inverted to a T_2 distribution. At the slow exchange limit as seen on the Fig. 7.1, two peaks have T_2 values similar to the ones in the input. The ratio of the area of the two peaks is 1. With the increase of exchange rate both peaks start to shift toward smaller T_2 values

with the shorter peak decreasing in amplitude and longer one gaining in amplitude. At the fast exchange limit of 10 ms^{-1} there is one peak at circa 4.5 ms. It is determined from the average rate of the input relaxation times, eq. 7.18 so that $T_2^{theory} = 4.54 \text{ ms}$. The integrated area of the single peak also corresponds to the sum of the two peaks in the slow exchange limit.

$$\frac{1}{T_2^{theory}} = \frac{1/2}{2.5} + \frac{1/2}{25} = \frac{1}{5} + \frac{1}{50} = 0.22 \quad (7.18)$$

This type of modelling shows the effect of different exchange rates. It explains the merging of the signals from two different pores as a function of the coupling.

7.3.3 Code validation: 2D exchange rate

The next step was a validation of the 3-site model, but with effectively switching off one of the sites by giving it an intensity 100 times smaller than other two intensities. Hence, we run simulations for two-site only: A \rightarrow B exchange and again for B \rightarrow C exchange .

For the A \rightarrow B exchange we used parameters that are close to our 3-site model with $k_{AB} = 700 \mu\text{s}$, 3 ms and 6 ms and $\tau_{ex} = 700 \mu\text{s}$, 3 ms and 6 ms. The final plot is a 3×3 matrix plot of the combination of both of these parameters Fig. 7.2.

For the B \rightarrow C exchange we used totally fictitious parameters as $k_{BC} = 50 \mu\text{s}$, 3 ms and 10 ms and $\tau_{ex} = 50 \mu\text{s}$, 3 ms and 10 ms. The final plot is a 3×3 matrix plot of the combination of these parameters Fig. 7.3.

The two figures contain very similar results and show that the code is working. However, the fictitious parameters of Figure 7.3 are easier to explain. If the exchange time is very short compared to the relaxation times ($\tau_{bc} \ll T_{2b}, T_{2c}$) as in the top row then there is efficient exchange averaging and only a single on-diagonal peak is seen at the relaxation time calculated similarly to Equation 7.18. As the exchange period of the experiment increases, so the magnetisation increasingly decays in τ_{ex} and the peak loses intensity.

In the bottom left row, the exchange period (τ_{ex}) is short and the exchange time (τ_{bc}) is long. There is no (very little) exchange and only two diagonal peaks are seen at the expected T_2 values of $800 \mu\text{s}$ and 8 ms. Moving right, as the exchange period t_2 gets longer so off-diagonal exchange peaks appear.

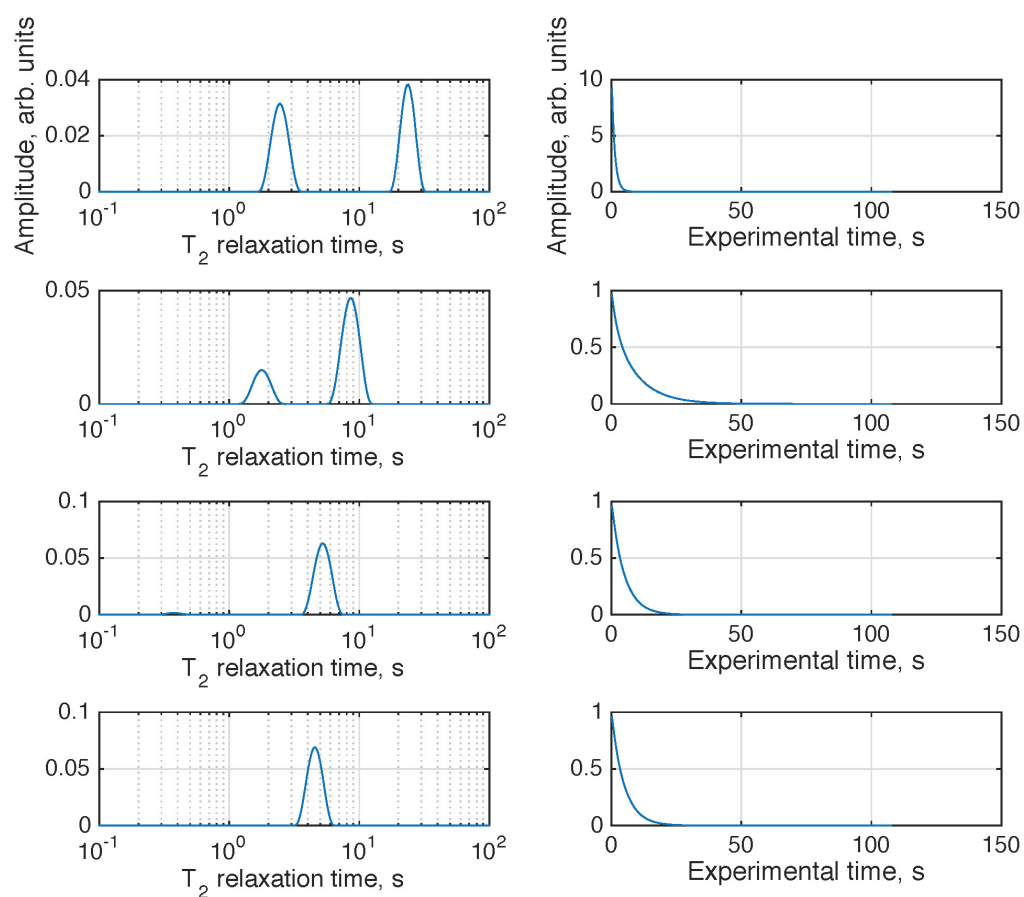


Fig. 7.1 Left is a 1D simulation of the T_2 distributions of 2 sites with input parameters: $T_{2a} = 2.5 \text{ ms}$, $T_{2b} = 25 \text{ ms}$, $M_a^0 = M_a b^0 = 0.5$. Four exchange values $k = k_a = k_b$ were used: from the top to the bottom: slow exchange (0.002 ms^{-1}), two intermediate exchange (0.1 ms^{-1} , 0.5 ms^{-1}) and fast exchange (10 ms^{-1}), with corresponding simulated CPMG data on the right.

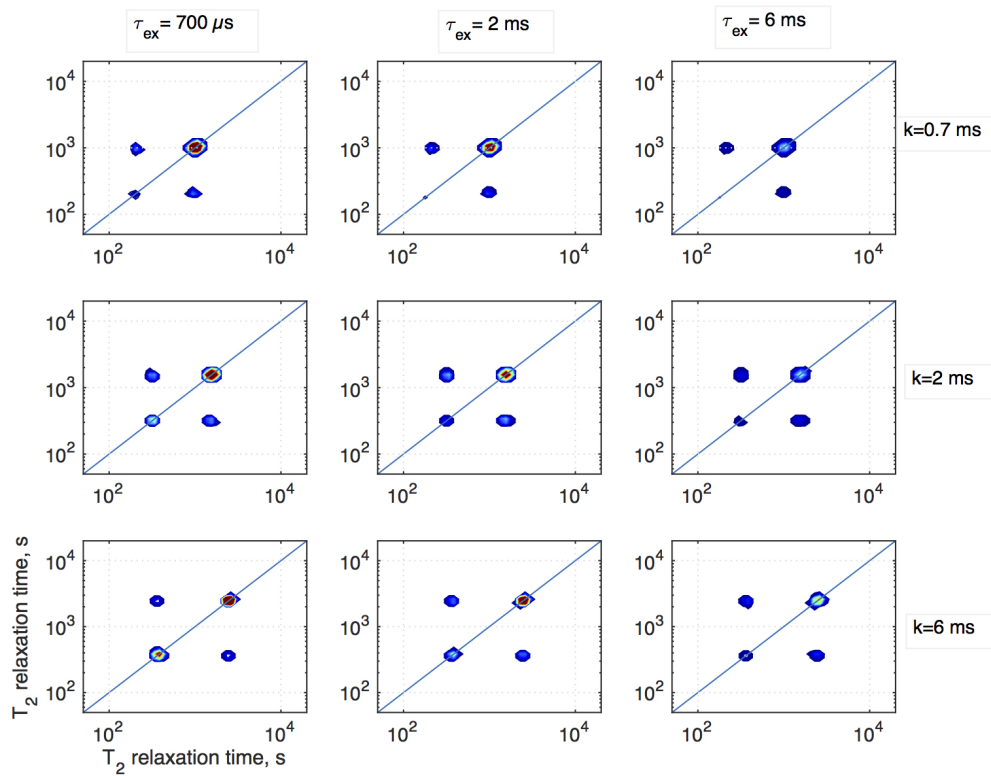


Fig. 7.2 2D simulation of the $T_2 - T_2$ spectra for left to right short, intermediate and long storage time and bottom to top slow, medium, and fast exchange rates for the A \rightarrow B exchange.

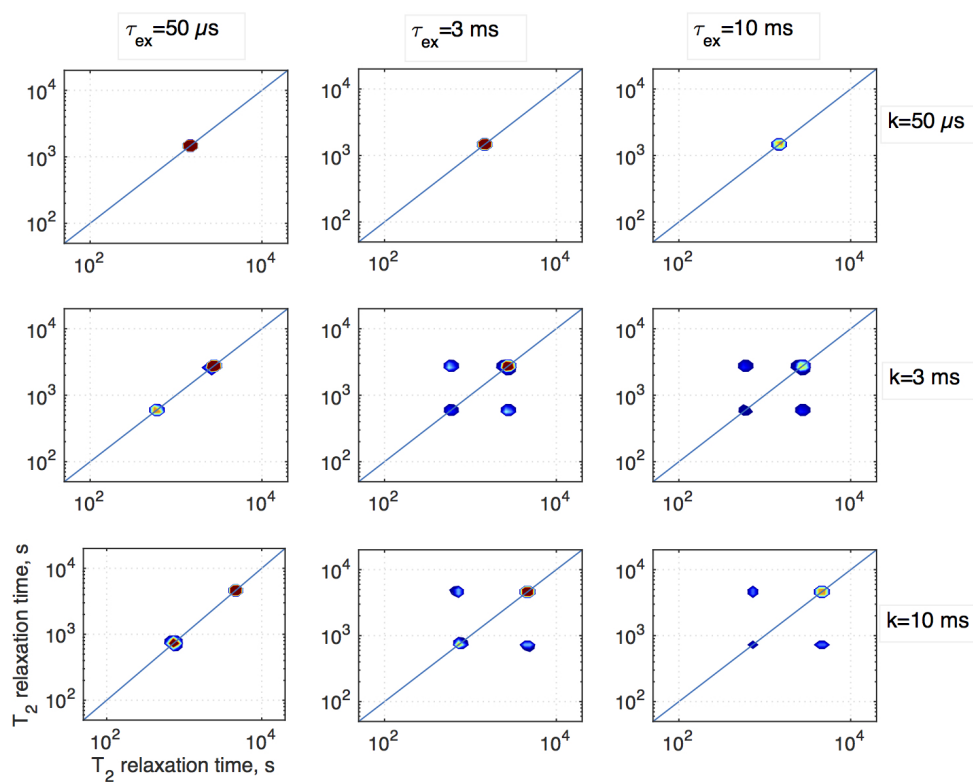


Fig. 7.3 2D simulation of the $T_2 - T_2$ spectra for left to right short, intermediate and long storage time and bottom to top slow, medium, and fast exchange rates for the for the B -> C exchange.

7.4 Materials and methods

7.4.1 Materials

C₃S powder used in this work was synthesised at LCR (Lafarge Research Center). The composition of the powder is 73.06% CaO, 26.02% SiO₂, 0.19% Al₂O₃, 0.07% Fe₂O₃, and 0.20% MgO. The free lime content was measured at 0.41%. Typically 10 g of powder was mixed with water in the water/C₃S mass ratio 0.51 (from here on we will call it the water to solid ratio $w/s = 0.51$) for three minutes by hand. For these experiments ELGA purified water was used. Around 1 cc of paste was placed in an 18 mm NMR tube and sealed immediately afterwards. Samples were kept in a temperature-controlled room at 21°C during hydration.

7.4.2 NMR experiments

¹H NMR measurements were made on a Maran Ultra spectrometer operating at 23.5 MHz. Before and after every $T_2 - T_2$ experiment two normal Carr-Purcell-Meiboom-Gill (CPMG) measurements were made with 512 scans. The 90° pulse length was 6.6 μs. CPMG echo measurements were made. Typically, 128 echoes with four points per echo were recorded. The echoes were logarithmically spaced starting from 57.75 μs and ending at 0.032 s. It was assured that the signal had completely decayed before the last echo. The repetition time was kept at 0.5 s after the pulse. T_2 distributions were obtained with inverse Laplace transform algorithm (ILT) software written at the Victoria University of Wellington (Wellington, New Zealand), which is based on the Venkataramanan et al. (2002) algorithm. CPMG data was analysed using the parameters: time range of 0.00001 s to 0.1 s with 500 points and the smoothing parameter of $\alpha = 1e^{12}$. Processing took approximately 5 minutes for each CPMG data set.

2D exchange experiments were performed with a $T_2 - T_2$ sequence. Full details of the pulse sequence are in previous chapter. The pulse sequence is programmed to increment through only odd echoes of the first CPMG, resulting in the 64x128 point data set, which was later adjusted to the 64x64 matrix by removing even echoes from the second CPMG encoding. The same number of echoes, logarithmic spacing and repetition delay were used as during the CPMG measurements. Storage intervals were varied in different experiments between 0.6 and 6.0 ms. Both positive and negative phases of storage were recorded and added together removing storage artefacts associated with recovery of magnetisation by T_1 so in the limit of long τ_s the final signal is zero. A single $T_2 - T_2$ experiment with 256 scans took about three hours.

Inverse Laplace transformation was performed with the 2D version of the ILT, used for CPMG. For the $T_2 - T_2$ analysis the used parameters were: a time range of 0.00001 s — 0.1 s with a 64x64 matrix and a smoothing parameter of $\alpha = 1e^6$. A standard laptop (2.7 GHz Intel Core i5) took approximately 2.5 hours on average to process data of this size. 2D ILT software also used more than 4Gb of RAM in order to build the matrix needed for the calculations. Low temperatures were achieved with dry air cooled down with liquid nitrogen.

A full cycle on a sample that took circa 12 hours to complete was performed in the following manner: three measurements were done at each temperature, CPMG first, $T_2 - T_2$ and CPMG again. The temperature cycle was +23°C then cooling down to -5°C, continue cooling down to -30°C and back to 23°C. The cycle was repeated for the 2.5, 3.5, 5.5, 9.5 days old samples with three storage times: 700 μ s and 2ms and 6ms. At each temperature samples were equilibrated to the given temperature for 15 minutes. Our previous tests show that 15 minutes are enough to stabilise temperature within the sample.

7.5 Experiment development

The $T_2 - T_2$ pulse sequence used for this experiment was written from scratch for the MARAN NMR instrument available at LafargeHolcim laboratories. It was written in Pascal. The full pulse sequence program can be found in Appendix B.

Since $T_2 - T_2$ is a multi pulse experiment, a phase cycling list for the different pulses should be implemented. Phase cycling removes systematic errors and unwanted coherence pathways. In particular, it ensures that for long τ_{ex} in $T_2 - T_2$ the signal is zero. Phase cycling used in the $T_2 - T_2$ pulse sequence is shown in Tab. 7.1.

P ₉₀	02022020131331310202202013133131
P ₁₈₀	11113333000022223333111122220000
90 store	02202002133131130220200213313113
90 anti-store	20200202313113132020020231311313
120	11113333000022223333111122220000
Acquisition	02202002133131130220200213313113

Table 7.1 Phase cycle used in the $T_2 - T_2$ pulse sequence, where 0, 1, 2 and 3 represent the x' , y' , $-x'$ and $-y'$ axes of the NMR rotating frame.

The pulse program was tested on standard samples such as rubber and water.

7.6 Results: $T_2 - T_2$

Fig. 7.4 shows the results for the T_2 - T_2 experiment on 2 days old C_3S paste with the storage time of 6 ms performed at 4 different temperatures as explained before.

At room temperature two diagonal peaks could be seen, one at around 0.6 ms and a much more intense peak at 3 ms. Off-diagonal peaks represent exchange peak between them. Peaks outside dotted lines represent an attempt of the ILT software to find peaks outside the measured range. They are due to slight errors in the first echo measurement or small offset baseline in the data.

At -5°C a very similar picture is seen with the difference that a low intensity peak at 0.2 ms is seen now. An -5°C data is stretched a bit along the diagonal line and is somewhat clearer. It is believed that the data at -5°C is generally better than at room temperature as any free water condensing in the NMR tube or in large capillary pores that otherwise interferes with the measurement is frozen. This allows the NMR to better resolve the nano-pore water. However, it is evident that the water in the nano-pores does not freeze at -5°C .

At -30°C there is one big peak at around 300-400 μs and a much smaller one at 4-5 ms. It is evident here that the water in interhydrate pores and larger gel pores has frozen since the intensity of the longer T_2 peak is smaller and the T_2 value is decreased compared to -5°C .

After being thawed and tested again at room temperature exchange still can be detected. The intensity of this exchange is comparable to the exchange in the non-frozen sample. It seems that freezing has not caused damage to the microstructure and the exchange is still there.

It seems that the most interesting data relevant to a study of connectivity are the data recorded at -5°C at different storage times. We choose -5°C because it seems to be much clearer compared to the room temperature. As it was mentioned above, this is because the bulk surface water and large capillary water is immobile (frozen) at this temperature. Thus only the signal from the water in the nano-pores is recorded.

Fig 7.5, 7.6 and 7.7 show the results of the $T_2 - T_2$ experiment applied to the 2.5 days old C_3S paste recorded at -5°C with three storage times: 700 μs , 2 ms, 6 ms respectively.

The data resolution is low which makes it difficult to extract exact peak positions and intensity values. It would take much longer times on the NMR spectrometer to record data with better signal-to-noise. Also a more powerful computer for the data processing would be needed for greater resolution (matrix size). From this point we continue to describe results based on the visual interpretation.

Fig. 7.5 shows 2.5 days old C_3S paste with the storage time of 700 μs . Three diagonal peaks can be seen with T_2 values of 200 μs , 900 μs and 4 ms. The result is inline with the CPMG data recorded before the $T_2 - T_2$ experiment. We associate these peaks with the

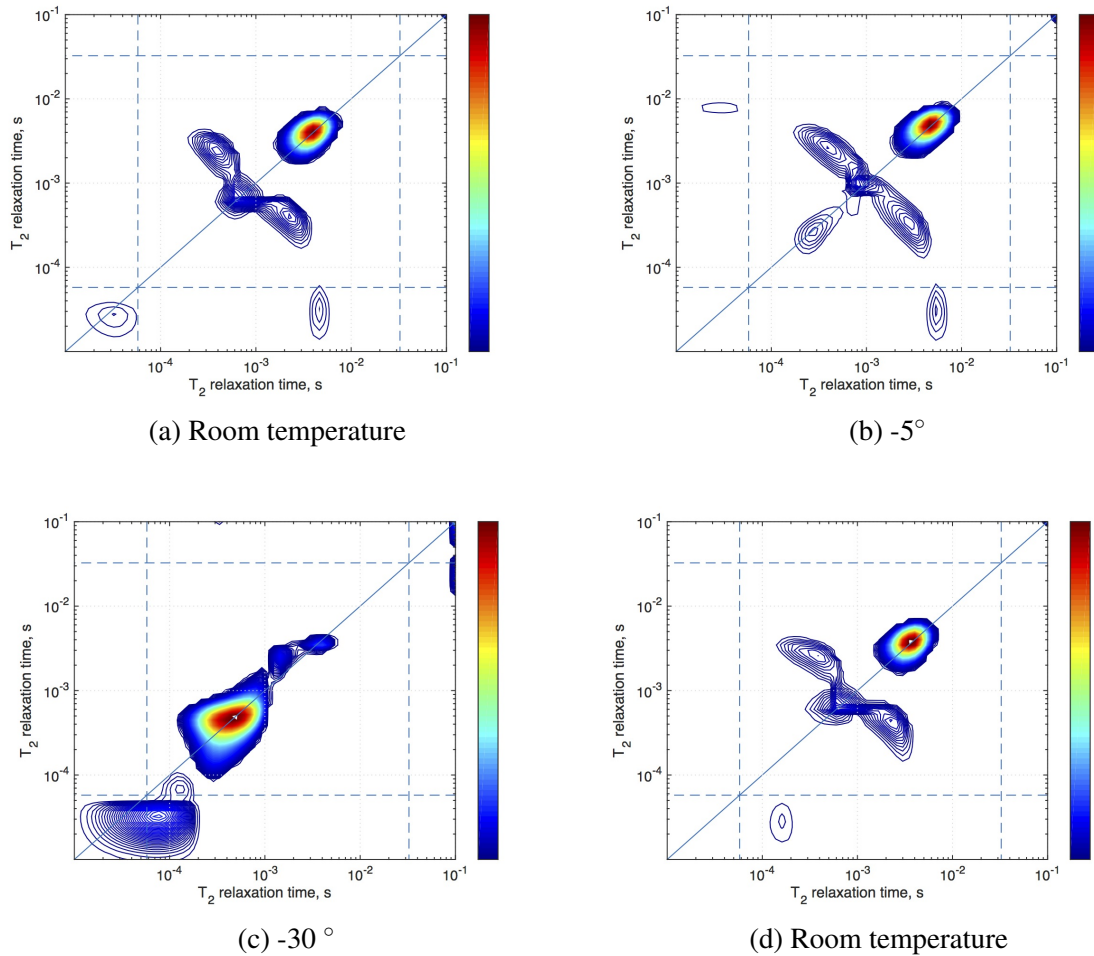


Fig. 7.4 Results of a $T_2 - T_2$ experiment on a 2 days old C_3S paste at 4 different temperatures (a) room temperature, (b) $-35^\circ C$, (c) $-30^\circ C$ and (d) room temperature again, with the storage time of 6 ms. The dotted lines bracket the region of inspected T_2 space. Peaks outside area are artefacts of inversion.

interlayer, gel and interhydrate water. Off-diagonal peaks are seen only between the two shortest peaks i.e. interlayer and gel pores. It means that at this short time frame of the experiment, hydrogen nuclei (or water) exchange between interlayer and gel pores only.

With the increase of the storage time to 2 ms, (Fig. 7.6) three diagonal peaks are at the same place with T_2 values of 200 μs , 900 μs and 4 ms. However, the shorter T_2 peaks lose some intensity. This happens due to the T_1 relaxation in exchanging pores and is in line with theoretical prediction. Off-diagonal peaks appear at a bit longer times. This possibly represents the exchange between the interlayer water and the interhydrate pores water. However, the peak position is unambiguous.

The 6 ms storage time data is shown in Fig. 7.7. It still has three diagonal peaks with T_2 values of 200 μs , 900 μs and 4 ms. Exchange off-diagonal peaks are now clear. They seem to show the existence of the interlayer - interhydrate exchange only.

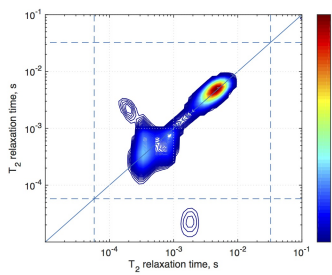


Fig. 7.5 T_2 - T_2 of the 2.5 days old C_3S at -5° with the storage time of 700 μs .

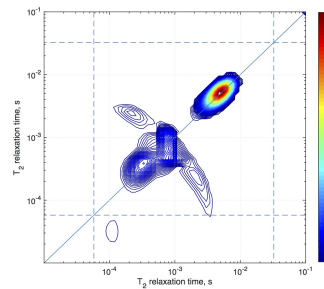


Fig. 7.6 T_2 - T_2 of the 2.5 days old C_3S at -5° with the storage time of 2 ms.

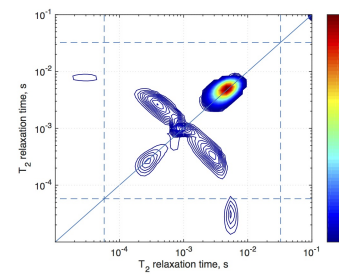


Fig. 7.7 T_2 - T_2 of the 2.5 days old C_3S at -5° with the storage time of 6 ms.

These results show that within C-S-H interlayer and gel pores are situated close to each other. The exchange existence at short storage times means that water can exchange between two types of pores at a very short times. But now the gel-interhydrate or the interlayer-interhydrate exchange is not detected.

At longer times such as 6 ms storage time water can get from interlayer to interhydrate pores. This process is longer, than interlayer-pores exchange. This means that interlayer and interhydrate pores are not so closely connected. Also there is no gel - interhydrate pores exchange.

The data therefore suggest that interhydrate pores and gel pores are connected to interlayer pores but not to each other. This seems logical. A gel pore connected to an interhydrate pore simply makes a bigger interhydrate pore.

7.7 Results: model

The idea of the $T_2 - T_2$ experiment is to calculate amplitudes change and T_2 time change of the off-diagonal peaks with the storage time variation. However, three pore types in C_3S made it impossible to calculate off-diagonal peaks intensities and hence calculate exchange rates. Rather the model is used to simulate data for different ratio and seen "by eye" agreement with experiment results.

The model was written for the purpose of finding exchange times. Input parameters, such as T_2 relaxation times and pore populations were taken from the experimental CPMG data. Further exchange rates were varied for three different storage times. It was shown from the experiments that there is no or very little exchange between the gel and interhydrate pores and that there is only the exchange between interlayer-gel and interlayer-interhydrate pores. τ_{ab} is the exchange between interlayer and gel pores. τ_{ac} is the exchange between interlayer and interhydrate pores. Both are expected to be possible exchange paths and are therefore finite in time > 0 . τ_{bc} is gel to interhydrate exchange. This is at best a minor direct exchange path. Therefore to simplify we set $\tau_{bc} = 0$ or $k_{bc} = \frac{1}{\tau_{bc}} = \infty$.

Fig.7.8, shows modelling for the storage time $t_2 = 0.7$ ms. Different exchange times for the interlayer-gel pore exchange τ_{ab} were used: $100 \mu s$, $330 \mu s$, 1 ms, 3.3 ms, 10 ms and 20 ms. This parameter varies from top to bottom in Fig.7.8. The same values were used for the interlayer-interhydrate exchange τ_{bc} , this parameter varies from left to right at Fig.7.8.

The results of the model for the storage time $t_2 = 0.7$ ms are compared to the same storage times of the $T_2 - T_2$ C_3S experiment shown at Fig 7.5. It appears that the most similar result with the model is achieved with the parameters $\tau_{ab} = 3.3$ ms and $\tau_{ac} 3.3$ ms.

For the ease of comparison we show the best model results and the C_3S data side by side in Fig. 7.9.

At Fig. 7.10 the results for the C_3S and the model for the storage time of 2 ms are compared to each other again. Just like in the $t_2 = 700 \mu s$ example, the most similar result with the model is achieved with the parameters $\tau_{ab} = 3.3$, maybe 10 ms and $\tau_{ac} 3.3$ ms.

Again for comparison the complete data set next to the best fit is presented in Fig.7.11.

The results in Fig.7.12 are obtained with the storage time $t_2 = 6$ ms. This should be compared to the $T_2 - T_2$ experiments with the same storage time of 6 ms Fig. 7.6. This model appears to be the most similar to the experimental results used with the parameters $\tau_{ab} = 3.3$ or maybe 10 ms and $\tau_{ac} 3.3$ ms.

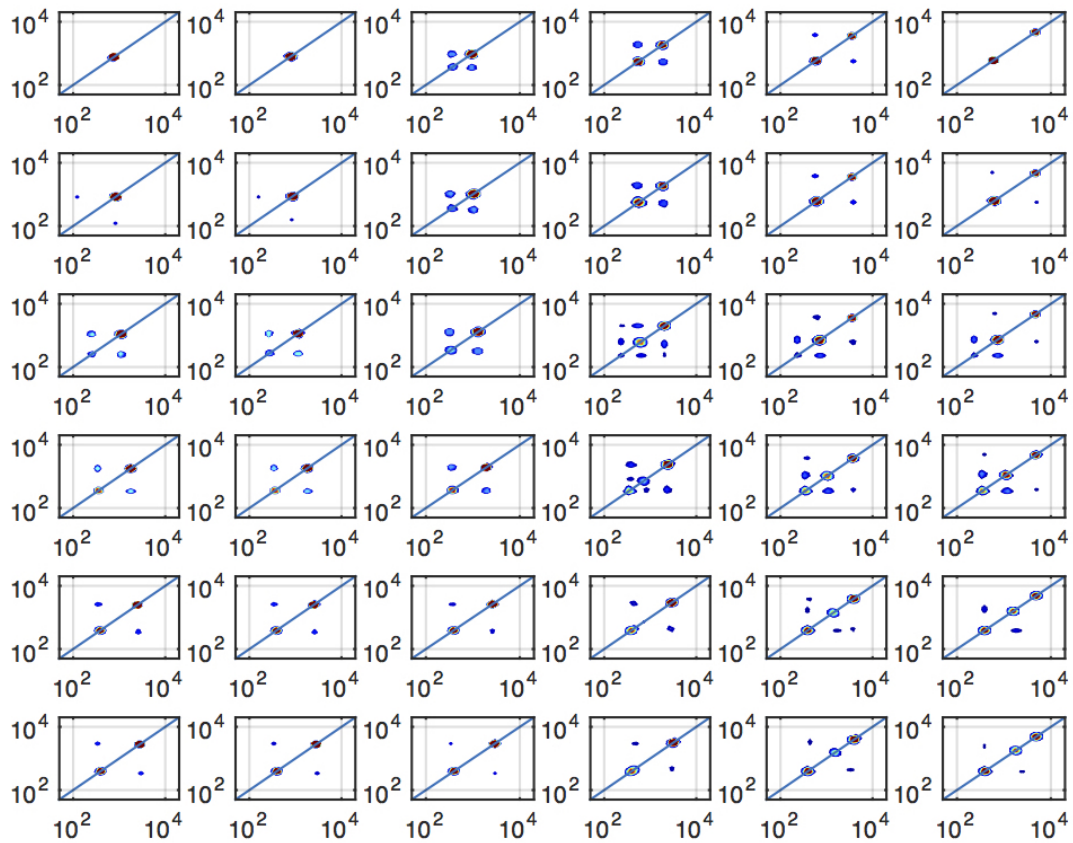
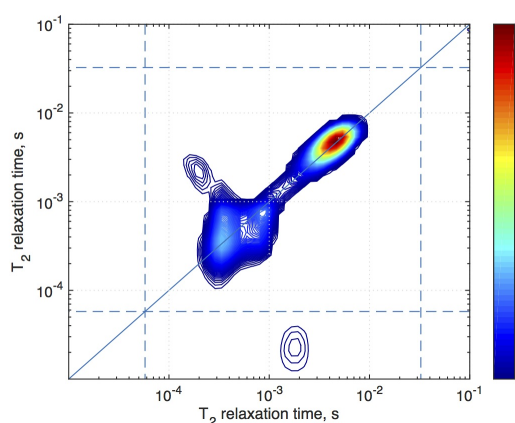
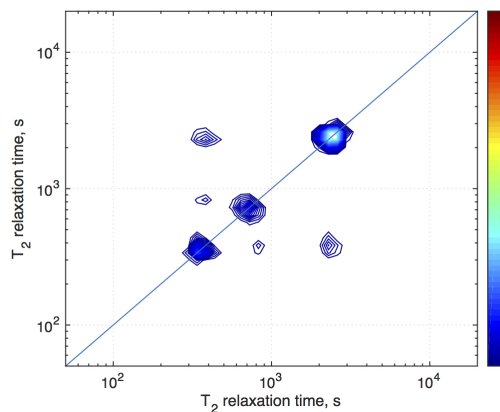


Fig. 7.8 Modelling results for the storage time $t_2 = 0.7$ ms. Different exchange times for the interlayer-gel pore exchange τ_{ab} were used: from top to bottom $100 \mu\text{s}$, $330 \mu\text{s}$, 1 ms, 3.3 ms, 10 ms and 20 ms. The same values were used for the interlayer-interhydrate exchange τ_{bc} , this parameter varies from left to right.

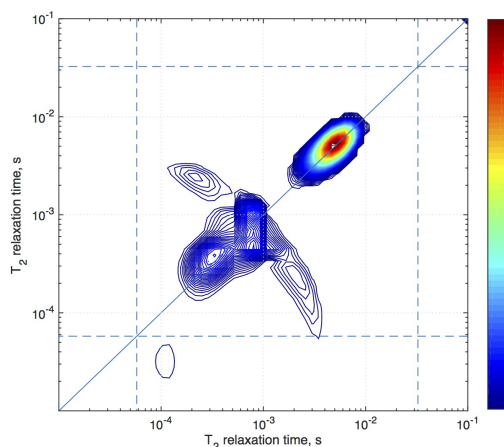


(a) A $T_2 - T_2$ data of the 2.5 days old C_3S at -5° with the storage time of $700 \mu s$.

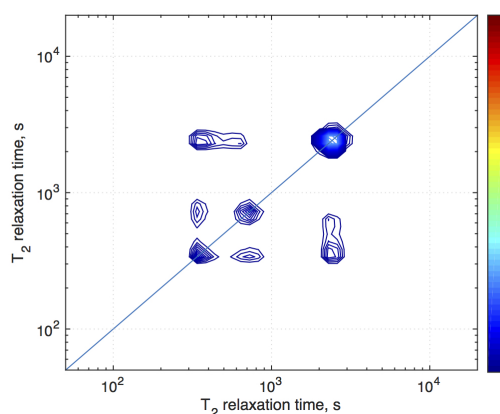


(b) A modeled $T_2 - T_2$ of the three-site system with the T_2 's similar to the C_3S with the storage time of $700 \mu s$; $\tau_{ab} = 3.3 \text{ ms}$ and $\tau_{ac} = 3.3 \text{ ms}$.

Fig. 7.9 Comparison of the model to the real data.



(a) A $T_2 - T_2$ data of the 2.5 days old C_3S at -5° with the storage time of 2 ms .



(b) A modelled $T_2 - T_2$ of the three-site system with the T_2 's similar to the C_3S with the storage time of 2 ms ; $\tau_{ab} = 3.3$ and $\tau_{ac} = 3.3 \text{ ms}$.

Fig. 7.10 Comparison of the model to the real data.

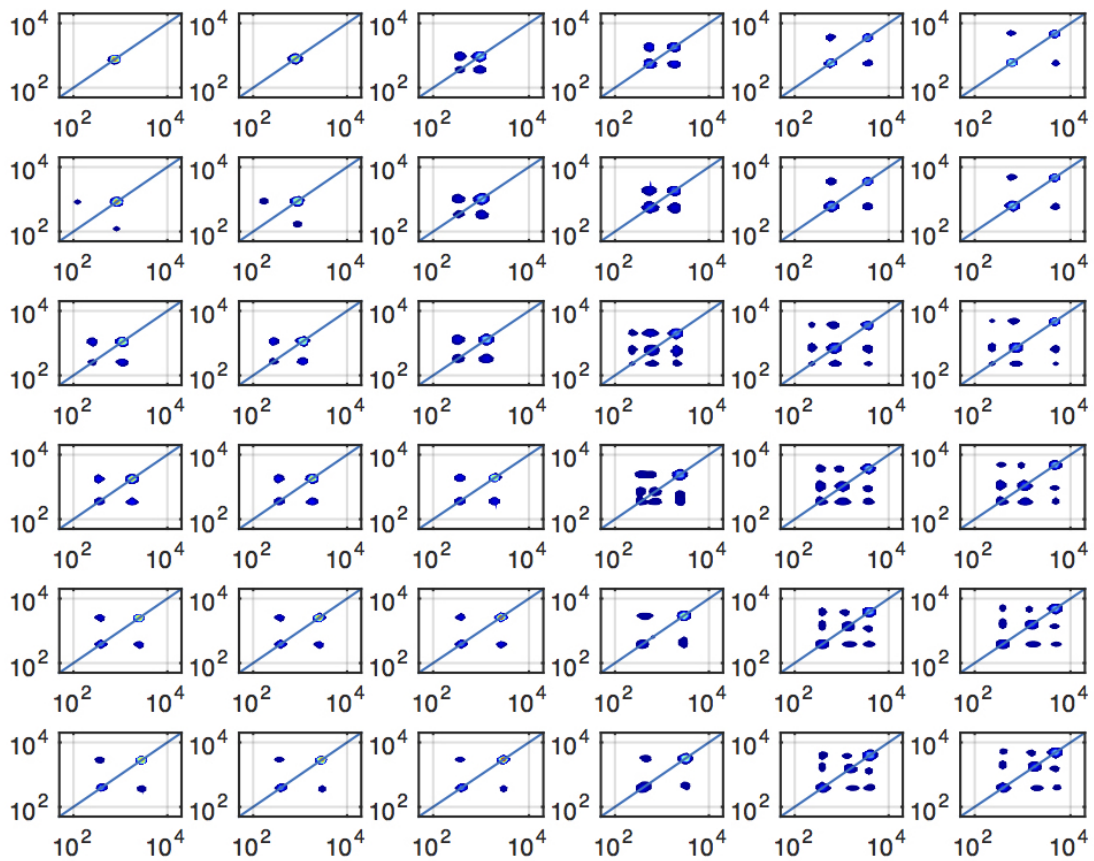


Fig. 7.11 Modelling results for the storage time $t_2 = 2$ ms. Different exchange times for the interlayer-gel pore exchange τ_{ab} were used: from top to bottom $100 \mu\text{s}$, $330 \mu\text{s}$, 1 ms, 3.3 ms, 10 ms and 20 ms. The same values were used for the interlayer-interhydrate exchange τ_{bc} , this parameter varies from left to right.

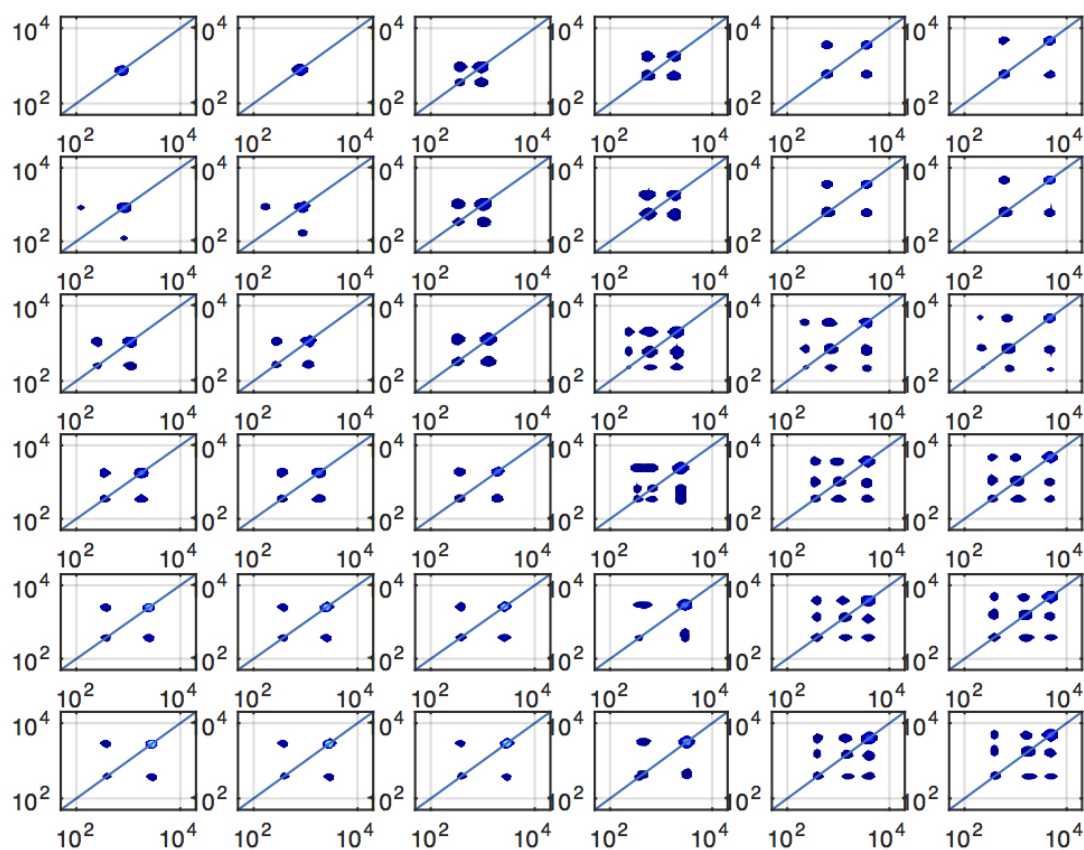


Fig. 7.12 Modelling results for the storage time $t_2 = 6$ ms. Different exchange times for the interlayer-gel pore exchange τ_{ab} were used: from top to bottom $100 \mu s$, $330 \mu s$, 1 ms, 3.3 ms, 10 ms and 20 ms. The same values were used for the interlayer-interhydrate exchange τ_{bc} , this parameter varies from left to right.

7.8 Conclusions

In this chapter a two dimensional ^1H NMR $T_2 - T_2$ exchange experiment was used to investigate the exchange of water between interlayer spaces, gel pores and capillary pores at temperatures of room temperature, -5°C and -30°C on cooling and again on warming in C_3S . A 3-site exchange numerical model was written to solve the associated coupled differential magnetisation exchange equations. By comparing the model output and experimental data it was shown that water exchanges between interlayer spaces and gel pores and between interlayer spaces and capillary pores. However, there is no exchange from gel pores to capillary pores. This makes sense so much as gel pores are not connected to capillary pore except through the solid hydrate interlayer spaces. This is first time 3-site $T_2 - T_2$ was performed and modelled on cement. The use of low temperature helped to confirm the results by freezing large pores.

Chapter 8

Conclusions

The most exciting results in this thesis are contained in the chapter 6: Study of C-S-H drying shrinkage and relaxation on rewetting in white cement. It has long been known that cement shrinks on drying but this work has shown that there are rearrangements of the nano porosity as water is removed and then replaced. Moreover it has been shown that there is a relaxation of the porosity from the new conformation back toward the original conformation over a timescale of about 10 days. Some of the changes are reversible, but some are not. Measurements were made with a function of drying severity. This is the first time results of this kind have been seen and they have been published in Cement and Concrete Research 86:12-19, August 2016: "A ^1H NMR relaxometry investigation of gel-pore drying shrinkage in cement pastes".

The results in the $T_2 - T_2$ chapter have cleared earlier uncertainties about what exactly was measured in this type of experiment. Applied to cementitious materials it has been shown that there is no exchange between gel and capillary pores. Only exchange of water between interlayer spaces and gel pores and between interlayer spaces and capillary pores in C_3S has been detected. Since gel pores are not connected to capillary pore except through the solid hydrate interlayer spaces these results are inline with current understanding of the C-S-H. This is the first time 3-site $T_2 - T_2$ was performed and modelled on cement. The use of low temperature helped to confirm the results by freezing large pores.

When this thesis work started, NMR cryoporometry had been attempted at LCR but had been unsuccessful. Thus the cryoporometry and relaxometry techniques were transferred from the University of Surrey and installed at the industrial laboratory. Cryoporometry has been validated on model porous glasses and been applied to the cementitious materials. The most interesting result is that T_2 depends on temperature in cementitious C_2S and C_3S , but not in the porous glasses: SiO_2 and MCM-41. A possible explanation is that this depends on the presence or not of surface hydroxyls, however, this requires detailed understanding of

the surface chemistry of cementitious materials and porous glasses and potentially requires molecular dynamics simulations, neither of which was available.

8.1 Future work

It could be interesting to model the water -OH group interaction. Results from such a model could explain different behaviour of T_2 relaxation time in SiO_2 and cementitious materials. Such a model could also explain the origin of the short T_2 arising from the non-freezing layers of water in nano-porous silica glasses recorded with CPMG at low temperatures.

Also by going at lower than -80°C it seems that it would be possible to detect low-density liquid (LDL) and a high-density liquid (HDL) transition with the relaxometry. This was never done before.

T_2 - T_2 is a time consuming experiment. However, recently ultrafast T_1 - T_2 NMR methods were developed (King et al., 2016). It has been shown, that such an approach shortens the experiment time by one to two orders of magnitude relative to traditional experiments, and increases the sensitivity per unit time by a factor of three. Such a quick T_2 - T_2 experiment is in demand both in industry and academia. In this work a typical T_2 - T_2 experiment took around 12 hours, during this time paste continues to hydrate which makes it difficult to investigate early hydration times. If we could shorten experimental time to around 1 hour we could get more insights on the C-S-H connectivity.

References

- Allen, A. J., Thomas, J. J., and Jennings, H. M. (2007). Composition and density of nanoscale calcium–silicate–hydrate in cement. *Nature materials*, 6(4):311–316.
- Balcom, B. J., Barrita, J., Choi, C., Beyea, S., Goodyear, D., and Bremner, T. (2003). Single-point magnetic resonance imaging (mri) of cement based materials. *Materials and structures*, 36(3):166–182.
- Bentz, D. P. (1997). Three-dimensional computer simulation of portland cement hydration and microstructure development. *Journal of the American Ceramic Society*, 80(1):3–21.
- Bishnoi, S. and Scrivener, K. L. (2009). μ ic: A new platform for modelling the hydration of cements. *Cement and Concrete Research*, 39(4):266–274.
- Blinč, R., Burgar, M., Lahajnar, G., Rožmarin, M., Rutar, V., Kocuvan, I., and Uršič, J. (1978). Nmr relaxation study of adsorbed water in cement and c3s pastes. *Journal of the American Ceramic Society*, 61(1-2):35–37.
- Bohris, A., Goerke, U., McDonald, P. J., Mulheron, M., Newling, B., and Le Page, B. (1998). A broad line nmr and mri study of water and water transport in portland cement pastes. *Magnetic resonance imaging*, 16(5):455–461.
- Breit, G. and Rabi, I. (1931). Measurement of nuclear spin. *Physical Review*, 38(11):2082.
- Brunauer, S., Emmett, P. H., and Teller, E. (1938). Adsorption of gases in multimolecular layers. *Journal of the American chemical society*, 60(2):309–319.
- Callaghan, P., Godefroy, S., and Ryland, B. (2003). Use of the second dimension in pgse nmr studies of porous media. *Magnetic Resonance Imaging*, 21(3-4):243 – 248. Proceedings of the Sixth International Meeting on Recent Advances in MR Applications to Porous Media.
- Callaghan, P. T. (2011). *Translational dynamics and magnetic resonance: principles of pulsed gradient spin echo NMR*. Oxford University Press.
- Cook, R. A. and Hover, K. C. (1999). Mercury porosimetry of hardened cement pastes. *Cement and Concrete research*, 29(6):933–943.
- Etzold, M. A., McDonald, P. J., and Routh, A. F. (2014). Growth of sheets in 3D confinements—a model for the C–S–H meso structure. *Cement and Concrete Research*, 63:137–142.
- Feldman, R. and Sereda, P. (1970). A new model for hydrated portland cement and its practical implications. *Engineering Journal*, 53(8-9):53–59.

- Filippov, A. and Vartapetyan, R. S. (1997). The nmr study of pore connectivity. *Colloid journal of the Russian Academy of Sciences*, 59(2):226–229.
- Fischer, N. (2015). *Validation of conventional concrete water transport test methods by spatially resolved 1H magnetic resonance*. PhD thesis, University of Surrey.
- Fischer, N., Haerdtl, R., and McDonald, P. J. (2015). Observation of the redistribution of nanoscale water filled porosity in cement based materials during wetting. *Cement and Concrete Research*, 68:148–155.
- Gajewicz, A., Gartner, E., Kang, K., McDonald, P. J., and Yermakou, V. (2016). A 1H NMR relaxometry investigation of gel-pore drying shrinkage in cement pastes. *Cement and Concrete Research*, 86:12–19.
- Gallé, C. (2001). Effect of drying on cement-based materials pore structure as identified by mercury intrusion porosimetry: a comparative study between oven-, vacuum-, and freeze-drying. *Cement and Concrete Research*, 31(10):1467–1477.
- Gartner, E. (2004). Industrially interesting approaches to low-cost cements. *Cement and Concrete research*, 34(9):1489–1498.
- Gartner, E. M. (1997). A proposed mechanism for the growth of C–S–H during the hydration of tricalcium silicate. *Cement and concrete research*, 27:665–672.
- Greener, J., Peemoeller, H., Choi, C., Holly, R., Reardon, E. J., Hansson, C. M., and Pintar, M. M. (2000). Monitoring of hydration of white cement paste with proton nmr spin–spin relaxation. *Journal of the American Ceramic Society*, 83(3):623–627.
- Hahn, E. L. (1950). Spin echoes. *Physical review*, 80(4):580.
- Hall, C. and Hoff, W. D. (2011). *Water transport in brick, stone and concrete*. CRC Press.
- Halperin, W. P., Jehng, J.-Y., and Song, Y.-Q. (1994). Application of spin-spin relaxation to measurement of surface area and pore size distributions in a hydrating cement paste. *Magnetic resonance imaging*, 12(2):169–173.
- Holly, R., Reardon, E., Hansson, C., and Peemoeller, H. (2007). Proton spin–spin relaxation study of the effect of temperature on white cement hydration. *Journal of the American Ceramic Society*, 90(2):570–577.
- Jackson, C. L. and McKenna, G. B. (1990). The melting behavior of organic materials confined in porous solids. *The Journal of Chemical Physics*, 93(12):9002–9011.
- Jennings, H. M. (2008). Refinements to colloid model of csh in cement: Cm-ii. *Cement and Concrete Research*, 38(3):275–289.
- Jennings, H. M., Kumar, A., and Sant, G. (2015). Quantitative discrimination of the nanopore-structure of cement paste during drying: New insights from water sorption isotherms. *Cement and Concrete Research*, 76:27–36.
- Jensen, O. M. (2005). Coe lecture, hokkaido university.

- Johannesson, B. and Utgenannt, P. (2001). Microstructural changes caused by carbonation of cement mortar. *Cement and Concrete Research*, 31(6):925 – 931.
- Kimmich, R. (2012). *NMR: tomography, diffusometry, relaxometry*. Springer Science & Business Media.
- King, J. N., Lee, V. J., Ahola, S., Telkki, V.-V., and Meldrum, T. (2016). Ultrafast multidimensional laplace NMR using a single-sided magnet. *Angewandte Chemie*, 128(16):5124–5127.
- Kowalczyk, R. M., Gajewicz, A. M., and McDonald, P. J. (2014). The mechanism of water–isopropanol exchange in cement pastes evidenced by nmr relaxometry. *RSC Advances*, 4(40):20709–20715.
- Lauterbur, P. C. (1973). Image formation by induced local interactions: examples employing nuclear magnetic resonance.
- Leventis, A., Verganelakis, D., Halse, M., Webber, J., and Strange, J. (2000). Capillary imbibition and pore characterisation in cement pastes. *Transport in Porous Media*, 39(2):143–157.
- Maruyama, I., Nishioka, Y., Igarashi, G., and Matsui, K. (2014). Microstructural and bulk property changes in hardened cement paste during the first drying process. *Cement and Concrete Research*, 58:20–34.
- McDonald, P. J., Korb, J.-P., Mitchell, J., and Monteilhet, L. (2005). Surface relaxation and chemical exchange in hydrating cement pastes: a two-dimensional nmr relaxation study. *Physical Review E*, 72(1):011409.
- McDonald, P. J., Mitchell, J., Mulheron, M., Aptaker, P. S., Korb, J.-P., and Monteilhet, L. (2007). Two-dimensional correlation relaxometry studies of cement pastes performed using a new one-sided NMR magnet. *Cement and concrete research*, 37(3):303–309.
- McDonald, P. J., Rodin, V., and Valori, A. (2010). Characterisation of intra-and inter-c–s–h gel pore water in white cement based on an analysis of nmr signal amplitudes as a function of water content. *Cement and Concrete Research*, 40(12):1656–1663.
- Meiboom, S. and Gill, D. (1958). Modified spin-echo method for measuring nuclear relaxation times. *Review of scientific instruments*, 29(8):688–691.
- Mitchell, J., Gladden, L., Chandrasekera, T., and Fordham, E. (2014). Low-field permanent magnets for industrial process and quality control. *Progress in nuclear magnetic resonance spectroscopy*, 76:1–60.
- Mitchell, J., Stark, S., and Strange, J. (2005). Probing surface interactions by combining nmr cryoporometry and nmr relaxometry. *Journal of Physics D: Applied Physics*, 38(12):1950.
- Mitchell, J., Webber, J. B. W., and Strange, J. H. (2008). Nuclear magnetic resonance cryoporometry. *Physics Reports*, 461(1):1–36.
- Monteilhet, L., Korb, J.-P., Mitchell, J., and McDonald, P. J. (2006). Observation of exchange of micropore water in cement pastes by two-dimensional T_2 - T_2 nuclear magnetic resonance relaxometry. *Phys. Rev. E*, 74:061404.

- Muller, A. C., Mitchell, J., and McDonald, P. J. (2015). *Proton nuclear magnetic resonance relaxometry*, pages 287–350. CRC Press.
- Muller, A. C., Scrivener, K., Gajewicz, A., and McDonald, P. J. (2013). Use of bench-top NMR to measure the density, composition and desorption isotherm of C–S–H in cement paste. *Microporous and Mesoporous Materials*.
- Muller, A. C., Scrivener, K. L., Gajewicz, A. M., and McDonald, P. J. (2012). Densification of C–S–H measured by ^1H NMR relaxometry. *The Journal of Physical Chemistry C*, 117(1):403–412.
- Muller, A. C. A. (2014). *Characterization of porosity and CSH in cement pastes by ^1H NMR*. PhD thesis, Ecole Polytechnique Federale De Lausanne.
- Navi, P. and Pignat, C. (1996). Simulation of cement hydration and the connectivity of the capillary pore space. *Advanced Cement Based Materials*, 4(2):58–67.
- Nestle, N., Galvosas, P., and Kärger, J. (2007). Liquid-phase self-diffusion in hydrating cement pastes—results from nmr studies and perspectives for further research. *Cement and concrete research*, 37(3):398–413.
- Peemoeller, H., Shenoy, R., and Pintar, M. (1981). Two-dimensional nmr time evolution correlation spectroscopy in wet lysozyme. *Journal of Magnetic Resonance (1969)*, 45(2):193–204.
- Petrov, O. and Furó, I. (2011). A study of freezing–melting hysteresis of water in different porous materials. part ii: surfactant-templated silicas. *Physical Chemistry Chemical Physics*, 13(36):16358–16365.
- Petrov, O. V. and Furó, I. (2009). Nmr cryoporometry: principles, applications and potential. *Progress in Nuclear Magnetic Resonance Spectroscopy*, 54(2):97–122.
- Powers, T. C. (1958). Structure and physical properties of hardened portland cement paste. *Journal of the American Ceramic Society*, 41(1):1–6.
- Powles, J. and Strange, J. (1963). Zero time resolution nuclear magnetic resonance transient in solids. *Proceedings of the Physical Society*, 82(1):6.
- Richardson, I. (2004). Tobermorite/jennite-and tobermorite/calcium hydroxide-based models for the structure of csh: applicability to hardened pastes of tricalcium silicate, β -dicalcium silicate, portland cement, and blends of portland cement with blast-furnace slag, metakaolin, or silica fume. *Cement and Concrete Research*, 34(9):1733–1777.
- Rodin, V., Valori, A., and McDonald, P. J. (2011). A ^1H double-quantum-filtered nmr study of water in cement pastes. *New Journal of Physics*, 13(3):035017.
- Strange, B. (1998). Organic nanocrystals: an nmr study of cyclohexane in porous silica. *Molecular Physics*, 93(2):263–269.
- Strange, J. (1994). Cryoporometry: a new *nmr* method for characterising porous media. *Nondestructive Testing and Evaluation*, 11(5):261–271.

- Taylor, H. F. (1997). *Cement chemistry*. Thomas Telford.
- Valckenborg, R., Pel, L., and Kopinga, K. (2002). Combined nmr cryoporometry and relaxometry. *Journal of Physics D: Applied Physics*, 35(3):249.
- Valori, A., McDonald, P., and Scrivener, K. (2013). The morphology of c–s–h: Lessons from 1h nuclear magnetic resonance relaxometry. *Cement and Concrete Research*, 49(0):65 – 81.
- Valori, A., Rodin, V., and McDonald, P. J. (2010). On the interpretation of 1H 2-dimensional NMR relaxation exchange spectra in cements: Is there exchange between pores with two characteristic sizes or Fe 3+ concentrations. *Cement and Concrete Research*, 40(9):1375–1377.
- Van Breugel, K. (1995). Numerical simulation of hydration and microstructural development in hardening cement-based materials:(ii) applications. *Cement and Concrete Research*, 25(3):522–530.
- Van Landeghem, M., Haber, A., D’espinoze De Lacaillerie, J.-B., and Blümich, B. (2010). Analysis of multisite 2D relaxation exchange NMR. *Concepts in Magnetic Resonance Part A*, 36(3):153–169.
- Venkataramanan, L., Song, Y.-Q., and Hurlimann, M. D. (2002). Solving fredholm integrals of the first kind with tensor product structure in 2 and 2.5 dimensions. *Signal Processing, IEEE Transactions on*, 50(5):1017–1026.
- Washburn, K. and Callaghan, P. (2006). Tracking pore to pore exchange using relaxation exchange spectroscopy. *Physical review letters*, 97(17):175502.
- Wu, M. (2014). *Using low temperature calorimetry and moisture fixation method to study the pore structure of cement based materials*. PhD thesis, Technical University of Denmark, Department of Civil Engineering.
- Wu, M., Fridh, K., Johannesson, B., and Geiker, M. (2015). Influence of frost damage and sample preconditioning on the porosity characterization of cement based materials using low temperature calorimetry. *Thermochimica Acta*, 607:30–38.
- Zamani, S., Kowalczyk, R., and McDonald, P. J. (2014). The relative humidity dependence of the permeability of cement paste measured using GARField NMR profiling. *Cement and Concrete Research*, 57:88–94.

Appendix A

Matlab 3 site exchange $T_2 - T_2$ model

Code

```
%  
%  
% Programme to Simulate 3 Site T2-T2 exchange data  
% Log tau spacings  
%  
clear all  
  
% Input parameters  
  
M0a=50;  
M0b=30;  
M0c=20;  
  
T2a=400;  
T2b=800;  
T2c=8000;  
  
tau_ab=inf; % exchange time = 1/rate  
tau_ba=tau_ab*M0b/M0a; % conservation of mass requirement
```

```

tau_ca=10; % exchange time = 1/rate
    tau_ac=tau_ca*M0a/M0c; % conservation of mass requirement
tau_bc=inf; % exchange time = 1/rate
    tau_cb=tau_bc*M0c/M0b; % conservation of mass requirement

    %T1=inf
    T1=4*T2

tau_echo_0=32; % first echo time
N_echo=64;
echo_time_mult=1.06;

t_mix=100; % mixing time

dt=1; % simulation step time << smallest relaxation or exchange time

%!!!!!!!!!!!!!!!!!!!!!!!!!!!!!!!!!!!!!!!!!!!!!!!!!!!!!!!!!!!!!!!!!!!!!!!!!!!!!!!!!!!!!!!!!!!!!!!!!!!!!!!!!!!!!!!!!!!!!!!!

% Calculated simulation Parameters

T2=[T2a, inf, inf; inf, T2b, inf; inf, inf, T2c];
T1=4*T2 %from McD and Korb 2005 PRE

R2=1./T2; % rates = 1/times
R1=1./T1;

kab=1/tau_ab; kac=1/tau_ac;
kbc=1/tau_bc; kba=1/tau_ba;
kca=1/tau_ca; kcb=1/tau_cb;
kaa=kab+kac;
kbb=kbc+kba;
kcc=kca+kcb;

k=[kaa, -kba, -kca; -kab, kbb, -kcb; -kac, -kbc, kcc];

```

```

D2=-R2-k; % relaxation exchange matrices
D1=-R1-k;

M0=[M0a;M0b;M0c]; % Initial M vector
Mstart=M0; % used to track 1st CPMG
t=0;

%*****%

for i=1:N_echo

    % Do first / next echo of first CPMG
    M=Mstart;
    N1=floor(tau_echo_0*(echo_time_mult^i)/dt);

    for p=1:N1
        M=M+D2*M*dt;
    end

    % Keep hold of M at end of ith echo of 1st CPMG
    % to speed up next cycle
    Mstart=M;

    % Continue with mixing time
    N2=floor(t_mix/dt);

    for p=1:N2
        M=M+D1*M*dt;
    end

    % Continue with 2nd CPMG
    for j=1:N_echo
        N3=floor(tau_echo_0*(echo_time_mult^j)/dt);

        for p=1:N3

```

```
        M=M+D2*M*dt ;
    end

    % Add total magnetisation to data array
    data(i,j)=sum(M);
end
end

t_vector=(tau_echo_0*echo_time_mult.^[1:1:N_echo])';
for i=2:N_echo
    t_vector(i)=t_vector(i-1)+t_vector(i);
end
figure (1);
imagesc(data);
figure (2);
plot(t_vector);
csvwrite('datafile.csv',data);
csvwrite('timefile.csv',t_vector);
```

Appendix B

$T_2 - T_2$ pulse sequence

```
PROGRAM T2T2;
{ VERSION 2.0          }
{ MARAN ULTRA          }

{ SUGGESTED PHASE LISTS }
{ PH1 0213021313201320 }
{ PH2 0213203113203102 }
{ PH3 1122112222332233 }
{ PH4 0213021313201320 }
{ PH5 2031021331021320 }

{$I COMPILE.INC }

USES
{$I UNITS.INC }

CONST
    PreEnable      = 20*US;
    { Warning: the Duty cycle should not exceed 30%.
      Do NOT use TAU values below 30 mus }

VAR
    n              : LONGINT;
    Count          : LONGINT;
```

```

AcqTime      : REAL;      { Define Total Acquisition Time }
Tauvar       : REAL;      { Define Variable Tau           }
TauOrig      : LONGINT;   { Original Tau from input
}
PreAcqTime   : LONGINT;   { Define Time Pre-Acquire       }
PostAcqTime  : LONGINT;   { Define Time Post-Acquire      }

```

PROCEDURE Sequence;

BEGIN

```

TauOrig:=Tau;      { Remember original input Tau   }
Tauvar:=Tau;      { Initialize Tauvar           }
AcqTime:=(SI-1)*DW; { Total Acquire Time }

Duration(20*us ,TXEnable1);      { Pre-enable CH1 RF}
ZeroTime;                        { Define Start Label For RINMR}
Duration(P90 ,RF(PH1)+TXEnable1); { 90 Pulse , CH1=PH1}
Duration(Round(Tau-(P90+P180)/2) ,TXEnable1);{ Wait For Tau}
Duration(P180 ,RF(PH3)+TXEnable1); { 180 Pulse , CH1=PH3 }

```

FOR Count:=1 TO NumEchoes-1 DO { Start Echo Train}

BEGIN

```

    PreAcqTime:=Round(Tau-(P180/2)); { Time Pre-Acquire }
    Duration(PreAcqTime ,0);          { Wait For Pre-Acquire Delay , }
                                     { enable Receiver }

```

```

Tauvar:=FP1*Tauvar;
IF Tauvar>30000 THEN
    Tauvar:=30000;

```

```

Tau:=Round(Tauvar);

```

```

PostAcqTime:=Round(Tau-P180/2); { Time Post-Acquire }
  Duration(PostAcqTime,0);
Duration(P180,RF(PH3)+TXEnable1); { 180 Pulse , CH1=PH3 }

END;

Duration(Round(Tau-P180/2),0);
Duration(P90,RF(PH4)+TXEnable1);
Duration(D2,0);

{second CPMG }

Tauvar:=TauOrig;
Tau:=TauOrig;

Duration(P90,RF(PH5)+TXEnable1); { 90 Pulse , CH1=PH1}
Duration(Round(Tau-(P90+P180)/2),TXEnable1);{ Wait For Tau }

FOR Count:=1 TO NumEchoes DO { Start Echo Train }
  BEGIN

    Duration(P180,RF(PH3)+TXEnable1); { 180 Pulse , CH1=PH3}
    Duration(Dead1,0); { Wait For Probe Ring Down }
    PreAcqTime:=Round(Tau-Dead1-(P180/2)-(AcqTime/2));
  { Time Pre-Acquire }
    Duration(PreAcqTime,REC); { Wait For Pre-Acquire De }
    { enable Receiver }

    FOR n:=1 TO SI-1 DO
      Duration(DW,REC+ADC(PH2)); { Acquire Echo , Phase PH2 }

    Tauvar:=FP1*Tauvar;
    IF Tauvar>30000 THEN
      Tauvar:=30000;

```

```

Tau:=Round(Tauvar);

PostAcqTime:=Round(Tau-(AcqTime/2)-P180/2); { Time Post-Acquire
}

Duration(PostAcqTime-PreEnable,REC+ADC(PH2));{ Post-Acquire Delay,}
                                                { enable CH1 for next 18
Duration(PreEnable, TXEnable1);

END;

Next(PH1);
Next(PH2);                                { Increment Phase Lists }
Next(PH3);
Next(PH4);
Next(PH5);
Duration(RD,0);                            { Wait For Relaxation Delay}

END;

BEGIN
Run(Sequence);
END.

```